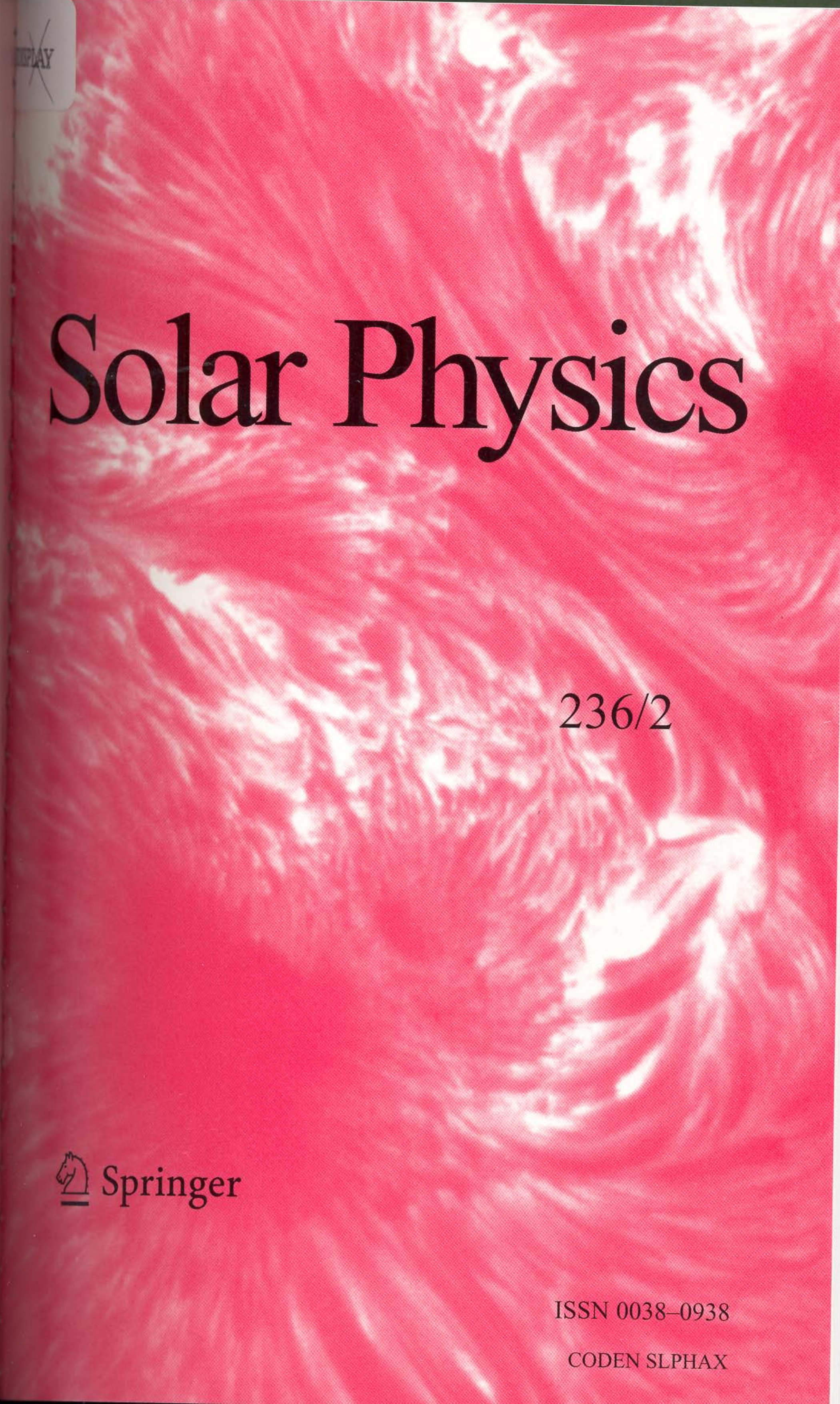

Solar Physics

236/2

Springer

ISSN 0038–0938

CODEN SLPHAX

SOLAR PHYSICS / *Vol. 236 No. 2 July 2006*

Solar Physics (2006) 236: 325–349
DOI: 10.1007/s11207-006-0039-z

ANALYSIS OF MAGNETIC SHEAR IN AN X17 SOLAR FLARE ON OCTOBER 28, 2003

Y.N. SU
Harvard-Smithsonian Center for Astrophysics, Cambridge, MA 02138, U.S.A.; Purple Mountain Observatory, Chinese Academy of Sciences, Nanjing 210008, P. R. China; Graduate University of Chinese Academy of Sciences, Beijing, P. R. China
(e-mail: ynsu@head.cfa.harvard.edu)

L. GOLUB and A.A. VAN BALLEGOOIJEN
Harvard-Smithsonian Center for Astrophysics, Cambridge, MA 02138, U.S.A.

and

M. GROS
DSM/DAPNIA/Service d'Astrophysique, CEA Saclay, 91191 Gif-sur-Yvette, France

(Received 1 August 2005; accepted 9 May 2006)

Abstract. An X17 class (GOES soft X-ray) two-ribbon solar flare on October 28, 2003 is analyzed in order to determine the relationship between the timing of the impulsive phase of the flare and the magnetic shear change in the flaring region. EUV observations made by the *Transition Region and Coronal Explorer* (TRACE) show a clear decrease in the shear of the flare footpoints during the flare. The shear change stopped in the middle of the impulsive phase. The observations are interpreted in terms of the splitting of the sheared envelope field of the greatly sheared core rope during the early phase of the flare. We have also investigated the temporal correlation between the EUV emission from the brightenings observed by TRACE and the hard X-ray (HXR) emission ($E > 150$ keV) observed by the anticoincidence system (ACS) of the spectrometer SPI on board the ESA INTEGRAL satellite. The correlation between these two emissions is very good, and the HXR sources (RHESSI) late in the flare are located within the two EUV ribbons. These observations are favorable to the explanation that the EUV brightenings mainly result from direct bombardment of the atmosphere by the energetic particles accelerated at the reconnection site, as does the HXR emission. However, if there is a high temperature ($T > 20$ MK) HXR source close to the loop top, a contribution of thermal conduction to the EUV brightenings cannot be ruled out.

1. Introduction

A two-ribbon structure in the chromosphere and transition region (e.g., in Hα, UV, and EUV) is often seen during a solar flare, especially for those long-duration events associated with coronal mass ejections (CMEs). The magnetic reconnection model proposed by Carmichael (1964), Sturrock (1966), Hirayama (1974), and Kopp and Pneuman (1976) (the CSHKP model) suggests that for an eruptive flare or CME, field lines open and then merge and reconnect at progressively higher altitudes in the corona. The EUV ribbons are the footprints in the transition region of the closed, reconnected field lines which are typically filled with hot coronal plasma in the form of postflare loops.

There are two proposed mechanisms for producing the EUV ribbon emission: thermal conduction from the reconnected loops, and direct bombardment of the lower atmosphere by accelerated particles from the reconnection site (Fletcher and Hudson, 2001). A close temporal relationship between the hard X-ray (HXR) and UV emission during the impulsive phase in solar flares was reported by Kane and Donnelly (1971) and Kane, Frost, and Donnelly (1979) using data from OGO and OSO satellites and was also found by SMM, when HXR and UV light curves were seen to be simultaneous to within 1 s (Woodgate *et al.*, 1983; for a review, see Fletcher, 2002).

Cheng *et al.* (1981) and Cheng, Tandberg-Hanssen, and Orwig (1984) made the first attempt to study the spatial structure of UV bursts using the UV observations with spatial resolution of a few seconds of arc obtained by UVSP. Their study showed that: (a) there was considerable preflare activity with UV transient brightenings occurring in many small point-like kernels; and (b) individual peaks in the HXR bursts can be identified with individual peaks in the UV bursts of individual flaring kernels. The recent observations from *Transition Region and Coronal Explorer* (TRACE), *Yohkoh*, and BATSE reported by Warren and Warshall (2001) showed that the initial HXR burst was positively correlated only with footpoints that showed no pre-HXR activity, which indicated that energy release during the preflare and impulsive phase of the flare was occurring on different loops. A comparison of HXR emission and EUV emission measured at the locations of the HXR sources was reported by Fletcher and Hudson (2001), who found that the light curves map to one another quite well. However, due to the TRACE time resolution of the event they reported, they could only establish that the two peaks are within 20 s of each other.

It is well known that during a two-ribbon flare the two footpoint ribbons, residing in opposite magnetic polarities, expand outward and away from each other (Svestka and Cliver, 1992). Some recent papers even reported an anticorrelation between the time profile of the separation distance of the conjugate footpoints and that of the HXR emission in a flare on September 9, 2002 (Ji *et al.*, 2004a,b; Huang and Ji, 2005). In addition to the ribbon separation in the direction perpendicular to the magnetic inversion line (MIL), which is predicted generically by the two-dimensional magnetic reconnection model, motions of the footpoints parallel to the direction of the MIL during flares have also been found by several authors. Masuda, Kosugi, and Hudson (2001) reported observations of the evolution of the HXR (*Yohkoh*/HXT) footpoints from a strong to a weak sheared structure, which was also found in Hα (Sartorius Refractor at Kwasan Observatory; Asai *et al.*, 2003) observations. A shear change of the footpoints observed at HXR (RHESSI) and microwave (Nobeyama Radioheliograph) was also reported by Kundu, Schmahl, and Garaimov (2004). This strong-to-weak shear change of the footpoints reflects a decrease in the shear of the newly reconnected loops during the course of the flare.

It should be noted that this decrease of the magnetic shear means that the outer magnetic field has weaker magnetic shear, and it does not mean that the magnetic shear is reducing during a flare.

In this paper, we focus on the question of what changes occur when a flare goes from the impulsive phase to the main phase. What causes this change, and how? The magnetic shear may show abrupt changes during a flare as reported in the above papers. The question we address here is: could the change from the impulsive to gradual phase be related to the magnetic shear change? For example, does the transition from the impulsive phase to the gradual phase occur as the initial flare brightenings evolve out of the filament channel into the larger surrounding volume?

To answer this question, we have selected a particularly well-observed X17 solar flare on October 28, 2003, which shows obvious shear change via the evolution of the EUV footpoints observed by TRACE, and examined the temporal evolution as well as the rate of change of the shear. The main observational data are summarized in Section 2. In Section 3.1 we present the comparison of EUV and HXR emission, and in Section 3.2 we study the pre-HXR EUV brightenings. The identification of the conjugate footpoints is described in Section 4.1. In Section 4.2 we focus on describing the decrease of the shear of the EUV footpoints, which is an apparent motion of the footpoints during the flare. The EUV emission mechanism of the brightenings is discussed in Section 5.1. Our interpretation of the evolution of the shear of the EUV footpoints is discussed in detail in Section 5.2. Conclusions are given in Section 6.

2. Observations

An X17 (GOES soft X-ray class) two-ribbon solar flare occurred in NOAA active region 10486 on October 28, 2003 at ≈11:00 UT. The main observational data used in this investigation were obtained simultaneously by the TRACE (Handy *et al.*, 1999) and the anticoincidence system (ACS) of the SPI spectrometer on board the ESA INTEGRAL satellite (Attié *et al.*, 2003; Vedrenne *et al.*, 2003). In addition to this large event, a filament eruption was seen in EUV (TRACE) and in Hα images (Figure 4 in Schmieder *et al.*, 2006 and Figure 2 in Wang *et al.*, 2005) about 40 min before the X17 solar flare and following a soft X-ray/EUV event which occurred about 10 min earlier (≈9:50 – 10:10 UT). Even though this filament eruption and the large flare that we studied involved the same magnetic inversion line, it is not clear whether they were related to each other, because of the large time difference. In this paper, we focus only on the X17 event.

During this event, SPI was observing the IC443 supernova remnant. Technical constraints fixed the satellite altitude in such a way that solar photons arrived at 122° from the telescope axis. At this incidence angle, the photons have to cross the satellite platform and the ACS of SPI. While the satellite platform practically is

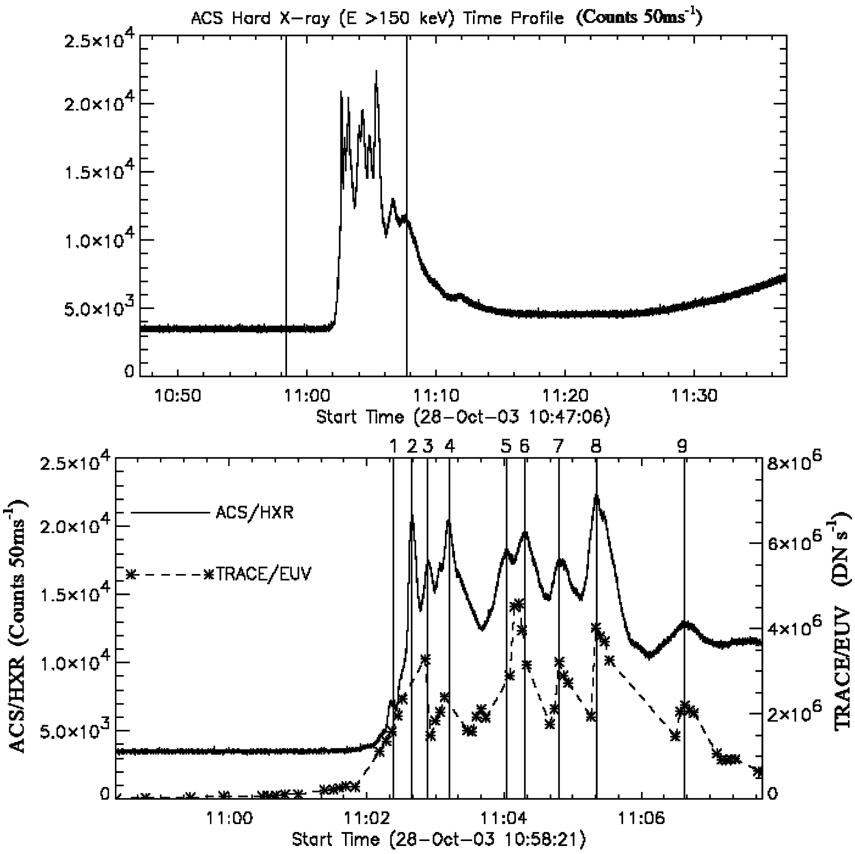

Figure 1. Light curves of the EUV and HXR emission. The SPI/ACS HXR light curve of the solar flare on October 28, 2003 is displayed in the *top panel*; the two lines mark the time range of the enlarged HXR light curve in the *bottom panel*, and nine spikes are marked by nine *vertical lines*. The summed TRACE/EUV light curve from all the brightenings is displayed via the *dashed line* with *asterisk signs* in the *bottom panel*.

transparent to the photons at such energies, the SPI/ACS system, composed of 5 cm thick BGO blocks, provides efficient shielding to photons arriving at the Germanium camera. On the other hand, the cross-section of this SPI/ACS, viewed under this 122° incidence angle, is $\approx$5200 cm^2. With a $\approx$100% efficiency from 150 keV up to some hundreds of keV, SPI/ACS is a very efficient detector for solar HXR in this energy range. As a result, count rates with 50 ms integration have been recorded with significant statistics, allowing a comparison of EUV and HXR intensity time profiles with very high precision. The SPI/ACS time profile of photons with energy $E > 150$ keV, in steps of 50 ms, is displayed in Figure 1. During the time period that we are interested in (bottom panel in Figure 1), nine peaks are seen and shown by the vertical lines. Peak 1, and Peaks 2 – 9 occurred during the rise phase and impulsive phase of the flare, respectively.

Given the high intensity of the flare, the number of photons detected in the SPI Ge detector matrix was sufficient to perform spectral analysis with 1 min integration time. The time profiles obtained for different energy bands suggest that during Peaks 1 – 4, photons with energies up to 10 MeV were emitted. The spectra integrated over these peaks show a clear power law bremsstrahlung spectrum (Gros *et al.*, 2004). Data from *Koronas*/SONG (Kuznetsov *et al.*, 2006) show that this spectrum extends up to 40 MeV. For the later peaks, it seems that this bremsstrahlung emission is mixed with nuclear (4 – 7 MeV) and pion (60 – 100 MeV) emissions.

TRACE observed AR 10486 from several hours before the flare until 12:56:46 UT on October 28, 2003, yielding data at 195 Å (Fe XII/XXIV), 284 Å (Fe XV), and 1600 Å (C IV plus UV continuum). Details of the TRACE instrumentation and performance can be found in Handy *et al.* (1999) and Golub *et al.* (1999). Observations at 195 Å and 1600 Å were recorded using an array size of 768 × 768 pixels, with a pixel size of 0.5 arcsecond, while the 284 Å observations used a 2 × 2 summed array of 512 × 512 pixels. Apart from the few 284 Å images taken, the observing mode was designed to alternate data acquisition between 195 Å and 1600 Å, with the time cadence at 195 Å higher than that at 1600 Å. To compare with HXR spikes, the TRACE data with high time cadence (typically ≈4 s) from 10:58:21 UT to 11:07:46 UT at 195 Å was selected. Due to the motion of the field of view (FOV), a small part of the north ribbon was sometimes not observed at 195 Å , but the ribbons in their entirety could be seen at 1600 Å and 284 Å at all times. TRACE observations show us that in the UV and EUV, the two flare ribbons are composed of discrete bright kernels (e.g., Figures 2 – 8). Our analysis focuses primarily on the observed evolution of these kernels during the course of the flare.

We note that some pixels in some of the EUV bright kernels saturated the Analog-to-Digital Converter (ADC) during the impulsive phase. We investigated the degree of saturation in the EUV images of this flare and found that (1) very few pixels (3%) saturated the ADC even for the brightest flare kernel, (2) the CCD itself did not reach saturation level (full well is five times greater than the ADC conversion limit), and (3) the saturated pixels were only slightly stronger than the other pixels in the kernels, as determined from analysis of the first-order images. This saturation will have some effect on the accuracy of the actual intensity of the flare kernel, but produces a negligible change in the shape of the summed light curves. Details of the method for investigating these effects are presented by Lin, Nightingale, and Tarbell (2001).

3. Comparison of EUV and HXR Emission

3.1. CORRELATION BETWEEN EUV AND HXR EMISSION

The SPI/ACS HXR data have excellent temporal resolution, but essentially no spatial resolution, while the TRACE data have both temporal and spatial resolution.

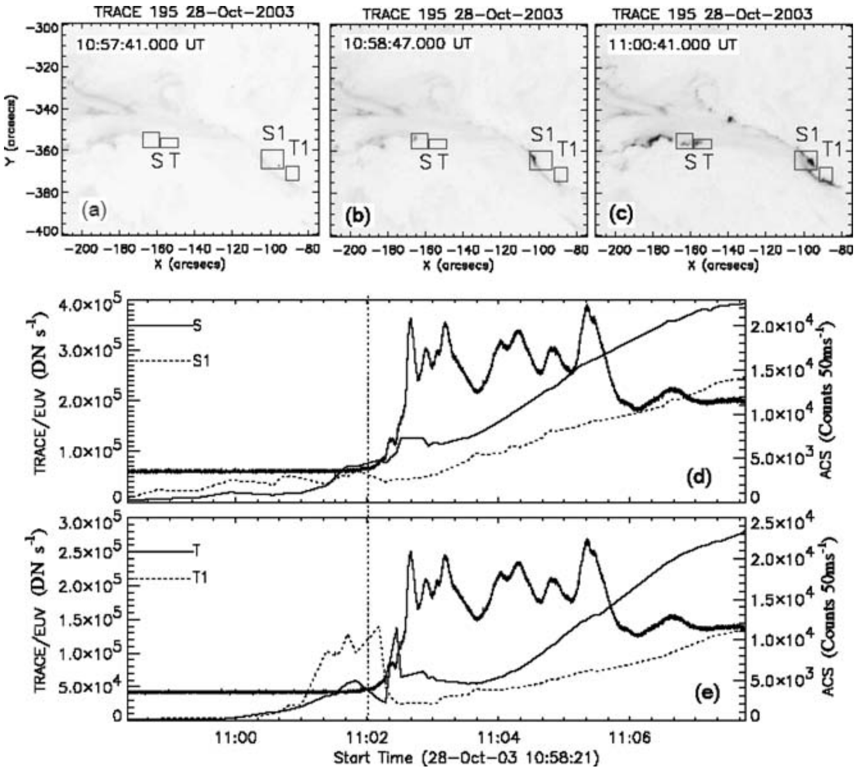

Figure 2. SPI/ACS/HXR light curves, TRACE/EUV images, and light curves of different brightenings during Phase 1. Phase 1 is the time period before HXR onset, which is represented by the vertical *dashed line*. (a) *Gray boxes* representing EUV brightenings "S"/"S1" and "T"/"T1" during Phase 1 are overlaid on an EUV image before Phase 1. (b), (c) EUV images are overlaid with gray boxes representing the EUV brightenings during Phase 1. (d), (e) EUV light curves of the two pairs of brightenings "S"/"S1" and "T"/"T1" during Phase 1. The ACS/HXR light curve is represented by the *thick solid line*.

RHESSI was behind the Earth at the start of this flare and began observations at 11:06:26 UT, which only caught the last HXR peak (Peak 9) in the impulsive phase. Our basic method of comparison to determine whether the EUV and HXR emissions are correlated is therefore based mainly on the timing of the EUV brightenings *versus* the timing of the HXR peaks.

In order to compare the EUV emission from the bright kernels and the HXR emission, boxes are defined in the EUV images that enclose the bright kernels. Because the bright kernels are continuously evolving (*viz.*, Fletcher, Pollock, and Potts, 2004), in order to track them we divide the rising and impulsive phases of this flare into eight time bins. Different boxes are chosen at the different time bins (see Figures 2 – 8) and the relevant kernels located in the boxes are labelled A, B, etc.

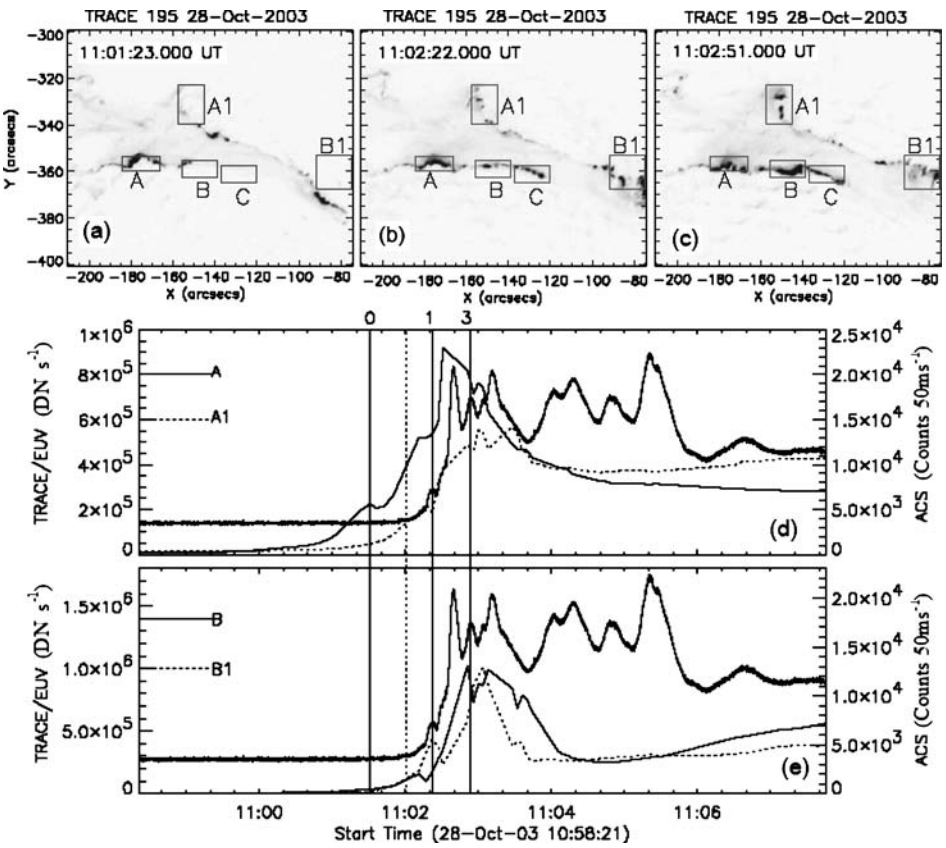

Figure 3. Similar to Figure 2 but for Phase 2. Phase 2 is the time period between the vertical *dashed line* representing HXR onset and the *solid line* representing Peak 3. (a) EUV image at EUV peak 0 before HXR onset is overlaid with *gray boxes* representing the EUV brightenings "A"/"A1," "B"/"B1," and "C" during Phase 2. (b), (c) *Gray boxes* representing EUV brightenings during Phase 2 are overlaid on EUV images closest in time to HXR Peaks 1 and 3. (d), (e) Similar to Figures 2d and 2e, but for EUV brightenings "A"/"A1," "B"/"B1," and "C" during Phase 2. The peaks are marked as *vertical line*.

The bottom panel in Figure 1 shows us the comparison of the hard X-ray light curve and the summed light curve of all the EUV bright kernels (for example, during Phase 1 it is the summed light curve of brightenings "S"/"S1" and "T"/"T1"). We can obtain a timing comparison, which is better than the cadence of the individual TRACE images by cross-correlating this summed EUV light curve as a whole against the HXR light curve. From Figure 1 we can see that the correlation between the HXR and EUV emission is very good, especially for HXR Peaks 3, 4, 7, 8, and 9. In order to quantify the temporal relationship between the HXR and EUV emission, we have done a cross-correlation between these two emissions for the individual HXR Peaks 4, 7, 8, and 9, and also a correlation of the full light curves

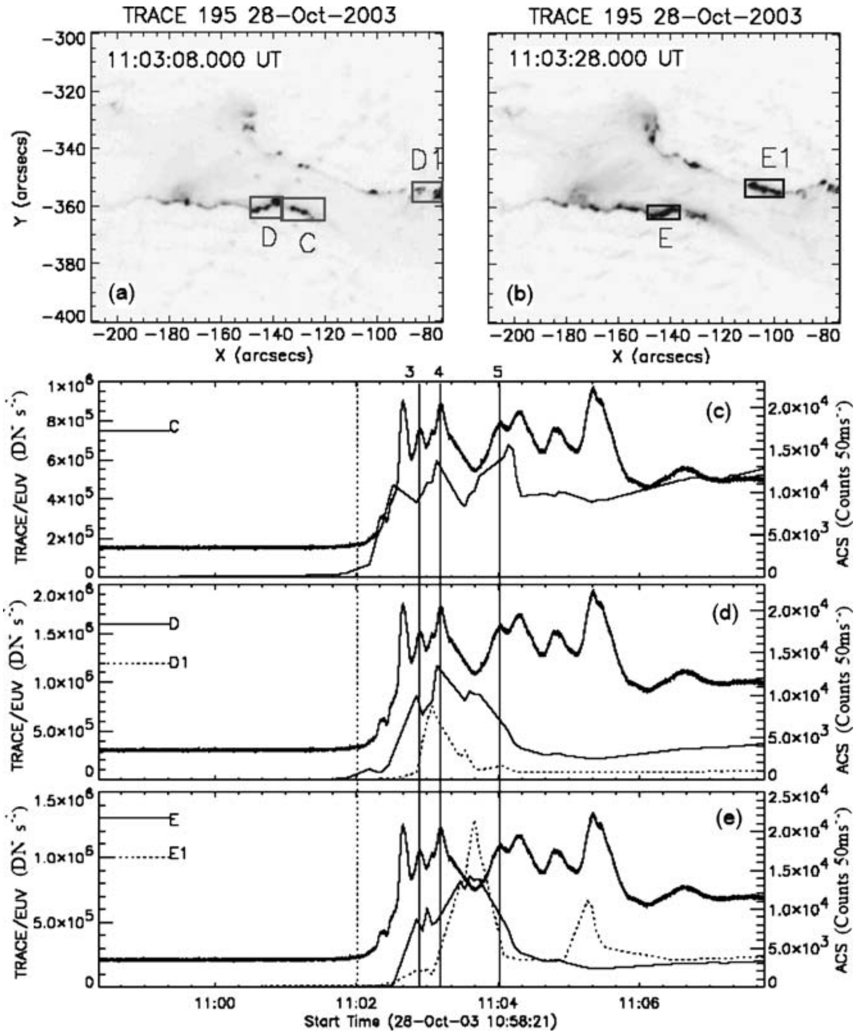

Figure 4. Similar to Figure 2, but for Phases 3 and 4. The time period between Peaks 3 and 4 is Phase 3, and Phase 4 is the time period between Peaks 4 and 5. (a) EUV image closest in time to HXR Peak 4 is overlaid with *gray boxes* representing the EUV bright kernels "C" and "D"/"D1" during Phase 3. (b) EUV image is overlaid with gray boxes representing the bright kernels E/E1 during Phase 4. (c), (d), and (e) Similar to Figures 2d and 2e, but for EUV brightenings during Phases 3 and 4, respectively.

from 10:58:21 UT to 11:07:46 UT. The time lags ($t_{\mathrm{EUV}} - t_{\mathrm{HXR}}$) obtained for the individual peaks are displayed in Table I, and the average time lag for these four peaks taken as an aggregate is 0.75 ± 1.4 s. The cross-correlation between the two complete light curves shown in the bottom panel in Figure 1 gives a time lag ($t_{\mathrm{EUV}} - t_{\mathrm{HXR}}$) of -1.25 ± 2.15 s (last line in Table I). From these results, we see that these

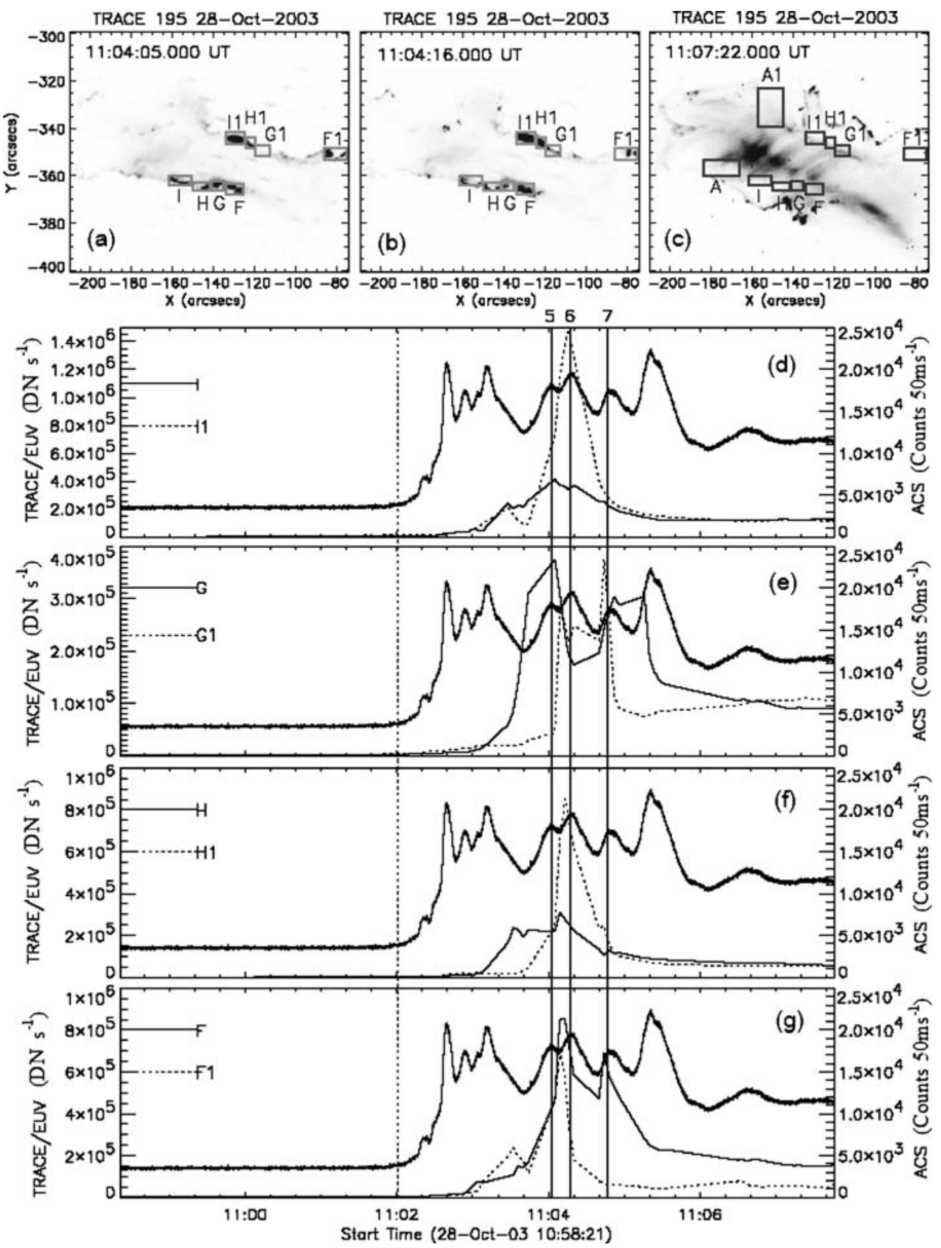

Figure 5. Similar to Figure 2, but for Phase 5 (the time period between Peaks 5 and 7). (a), (b) *Gray boxes* representing EUV brightenings during Phase 5 are overlaid on the EUV images closest in time to HXR Peaks 5 and 6, respectively. (c) *Gray boxes* representing EUV brightenings are overlaid on an EUV image of the postflare loops. (d), (e), (f), and (g) Similar to Figures 2d and 2e, but for EUV brightenings during Phase 5.

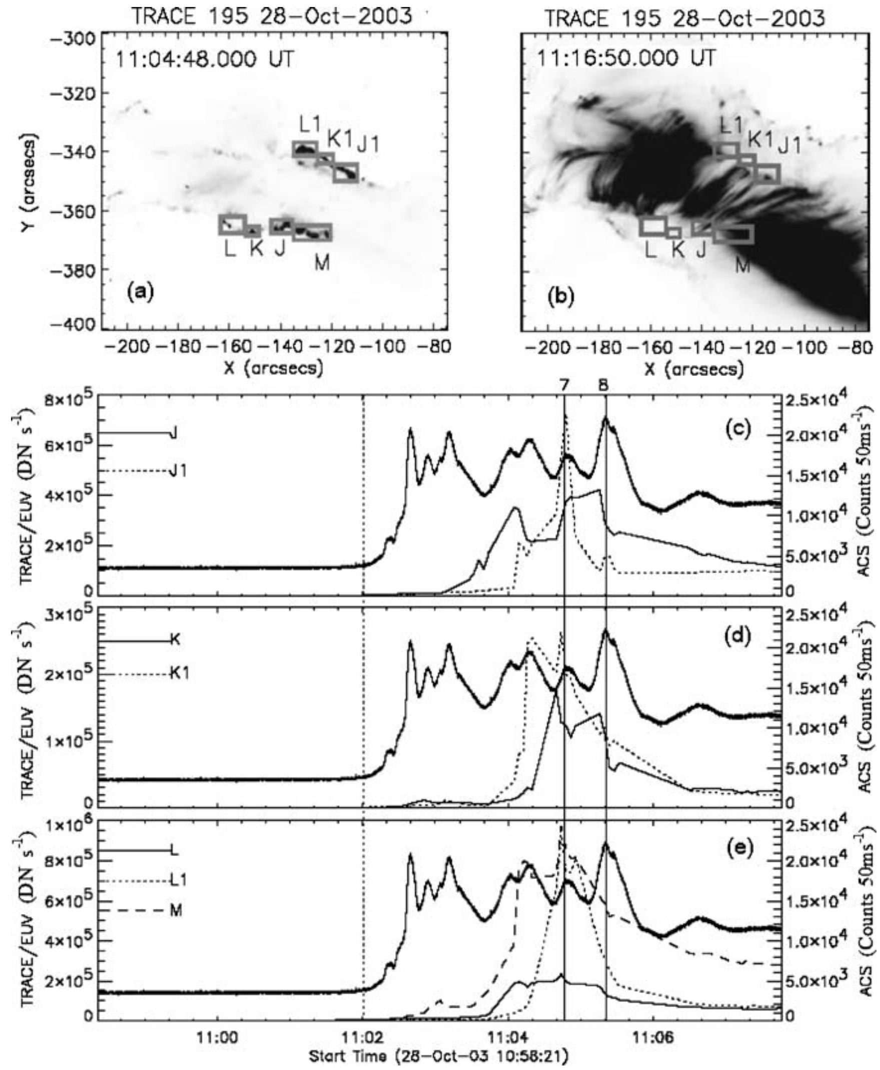

Figure 6. Similar to Figure 2, but for Phase 6 (the time period between Peaks 7 and 8). (a) *Gray boxes* representing EUV brightenings during Phase 6 are overlaid on the EUV image closest in time to HXR Peak 7. (b) *Gray boxes* representing EUV brightenings during Phase 6 are overlaid on an EUV image of the postflare loops. (c), (d), and (e) Similar to Figures 2d and 2e, but for EUV brightenings during Phase 6.

two types of emission are effectively simultaneous to our measurement accuracy, which is in the range $\approx 1-3$ s.

With the high spatial resolution of TRACE, we also examined the light curves of individual bright kernels (Figures 2 – 8) in order to find the EUV bright kernels corresponding to each HXR peak, and the resulting identifications are listed in

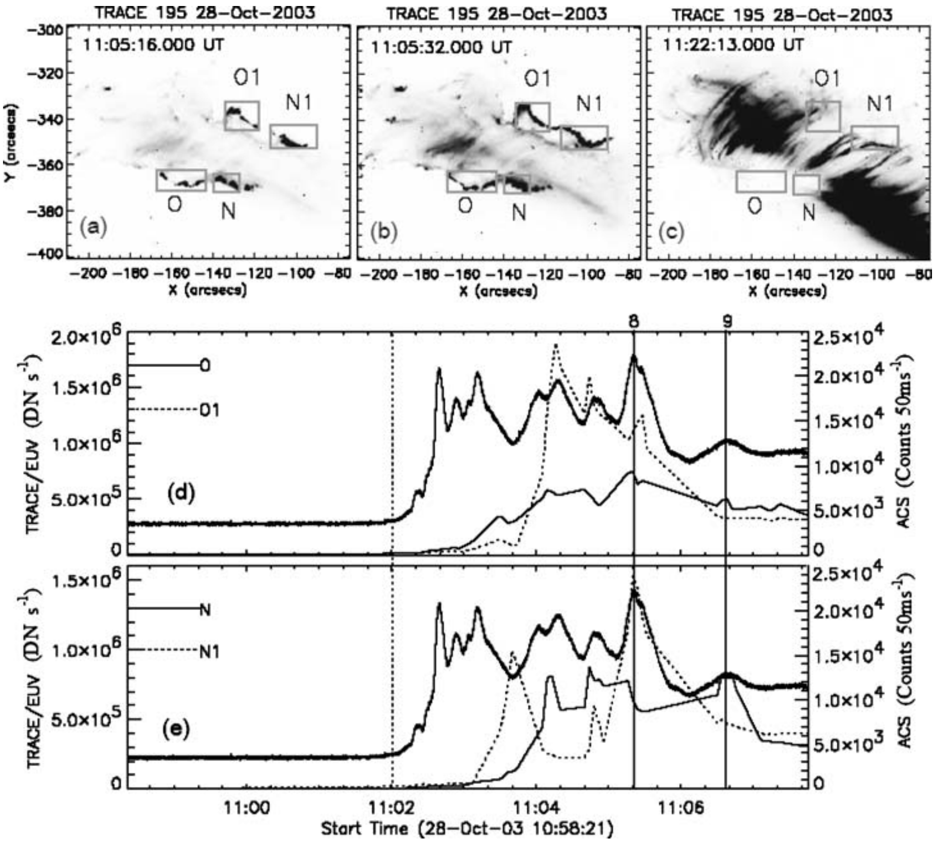

Figure 7. Similar to Figure 2, but for Phase 7 (the time period between Peaks 8 and 9). (a), (b) *Gray boxes* representing EUV brightenings during Phase 7 are overlaid on the EUV image closest in time to HXR Peak 8 and another EUV image during Phase 7, respectively. (c) *Gray boxes* representing EUV brightenings during Phase 7 are overlaid on an EUV image of the postflare loops.(d), (e) Similar to Figures 2d and 2e, but for EUV brightenings during Phase 7.

Table I. Table I presents the times of the HXR peaks, time lags between the EUV and HXR emission, and the EUV bright kernels corresponding to each HXR peak. The second column in Table I refers to the time of the HXR peak, and the third column shows the time of the EUV observations closest in time to each HXR peak. The fourth column shows the time lags between the HXR and EUV emission determined from a cross-correlation analysis of the respective peaks, and the error bar $(1 - \sigma)$ is given in the same column. The last column identifies the EUV bright kernels, which we believe are corresponding to the HXR peak. From Table I we can see that in the EUV observations closest in time to nearly each HXR peak, we find a peak in the EUV light curves from one or more bright kernels. These bright kernels are therefore possibly related to the HXR peak. We do not find the corresponding

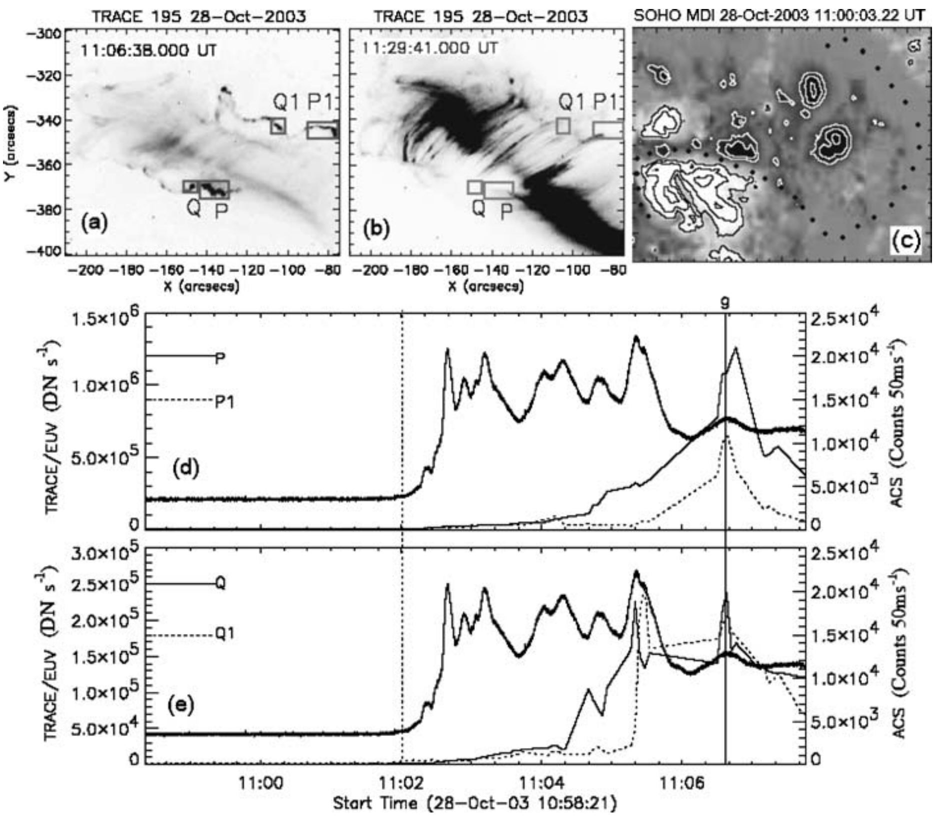

Figure 8. Similar to Figure 2, but for Phase 8 (the time period after Peak 9). (a) *Gray boxes* representing EUV brightenings during Phase 8 are overlaid on the EUV image closest in time to HXR Peak 9. (b) *Gray boxes* representing EUV brightenings during Phase 8 are overlaid on a later EUV image of the postflare loops. (c) SOHO/MDI photospheric magnetogram overlaid with MDI contours, where *white* and *black contours* refer to negative and positive magnetic field, respectively. The *black dotted line* represents the locus of the filament. The field of view is $240'' \times 160''$. (d), (e) Similar to Figures 2d and 2e, but for EUV brightenings during Phase 8.

EUV bright kernels for HXR Peak 2, but we note the lack of EUV observations near the time of that peak.

3.2. Pre-HXR EUV brightenings

From the light curves in Figures 1 and 2 we can see that the EUV emission from the bright kernels starts to rise at 10:58:21 UT, which is more than 3 min before the onset of the first HXR burst (11:02:00 UT). We also see some small peaks in the EUV light curves (e.g., Peak 0 in Figure 3d) before HXR onset.

EUV brightenings before the HXR onset appear within two slender ribbons, as can be seen in Figures 2b and 2c. The comparison of the morphology of the

TABLE I

Timing of HXR peaks and corresponding EUV brightenings.

Peak	SPI/ACS HXR ($E > 150$ keV) t_{HXR} (UT)	TRACE/EUV (195 Å) t_{EUV} (UT)	Time lag $\Delta t = t_{EUV} - t_{HXR}$ (s)		Corresponding TRACE/EUV Bright kernels
Peak 1	11:02:23.373	11:02:22			B1
Peak 2	11:02:39.573	11:02:31			
Peak 3	11:02:53.773	11:02:51			A1, B
Peak 4	11:03:11.923	11:03:08	−2.8	±1.2	C, D
Peak 5	11:04:02.323	11:04:05			I, G
Peak 6	11:04:18.423	11:04:13			I1
Peak 7	11:04:47.923	11:04:48	1.8	± 1.0	J1
Peak 8	11:05:20.823	11:05:20	2.9	± 1.0	O, N1
Peak 9	11:06:37.323	11:06:38	1.1	± 2.4	P1, Q/Q1
Total			−1.25	± 2.15	

pre-HXR brightenings and the later flare ones (*viz*., Figure 3a) shows us that the flare brightenings result from an outward expansion of the pre-HXR EUV brightenings in a direction perpendicular to the ribbons and an extension of the pre-HXR brightenings along the direction of the ribbons (Figures 9a – e). Some of the flare brightenings are also seen before the HXR onset, such as brightening "A." These observations show that the preflare EUV brightenings are very similar to the flare ones, differing mainly in intensity but similar to the later flare brightenings in most other respects.

4. Evolution of the EUV Bright Kernels

4.1. Identification of the EUV conjugate footpoints

The most prominent conjugate footpoints have been identified manually by studying the evolution of the EUV bright kernels. There are three factors that we considered in identifying brightenings as conjugate footpoints: (1) the two brightenings appear simultaneously, (2) the light curves of the two brightenings are very similar, and (3) the two brightenings are connected by postflare loops. In this section we focus on describing in detail several examples of the method to show how we track and identify the conjugate footpoints in this flare.

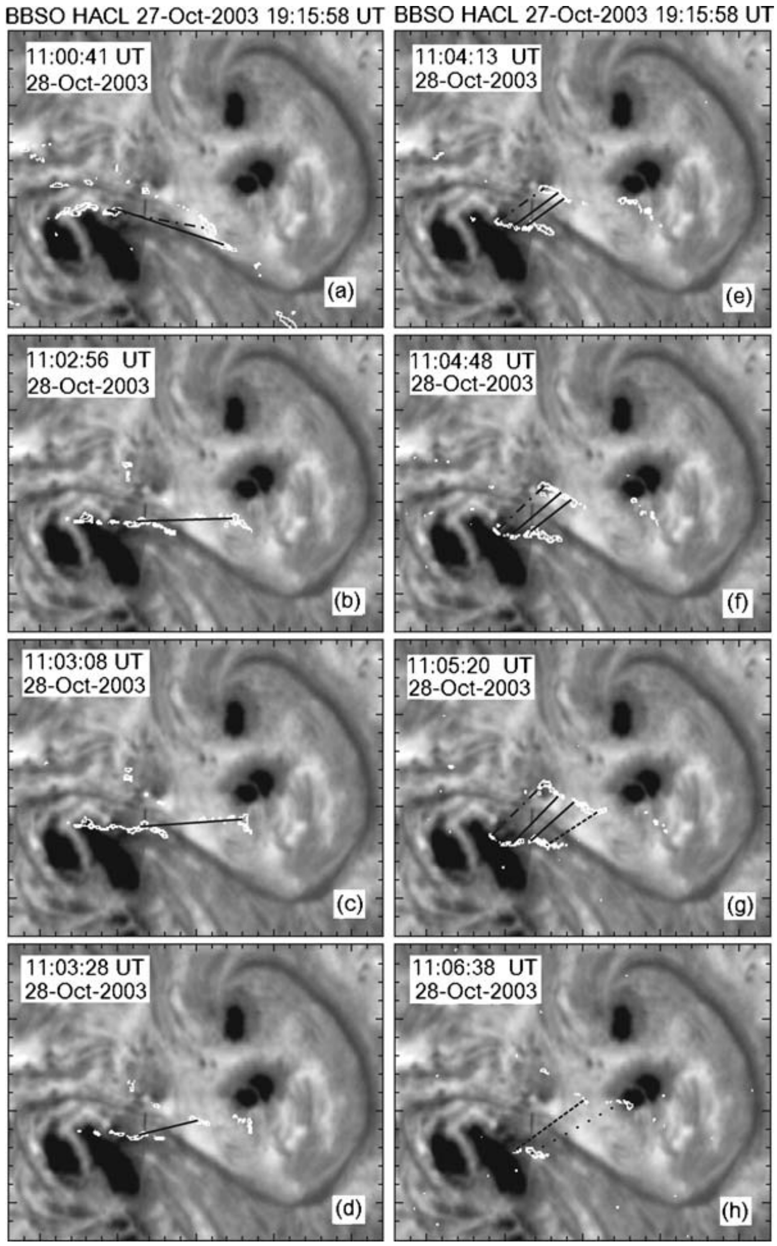

Figure 9. EUV brightenings and Hα image. TRACE/EUV contours at different times are overlaid on an earlier Hα image from BBSO. The times of the EUV contours are marked on each image, and the *black lines* connecting to the EUV bright kernels represent the possible conjugate EUV footpoints. Different kind of line refers to different group of brightening pairs. The field of view is $240'' \times 160''$ for each image.

Most of the EUV conjugate footpoints before Phase 5 have similar light curves, and some of the pairs can also be identified as appearing at the same time. These early brightenings are close to the neutral line and any possible postflare loops connecting them would be hidden under the larger postflare loops connecting the outer brightenings (see below for a discussion of the relative timing). Since no corresponding postflare loops can be seen, we identify the conjugate footpoints mainly by the first two factors.

For example, at 10:58:21 UT, the first EUV brightening “S1” appears in the western part of the north ribbon and spreads from east to west. The next brightening, “S,” located in the eastern part of the south ribbon appears at 10:58:47 UT and spreads from east to west (Figure 2b). Because (i) only these two brightenings can be seen at this time, (ii) the time of their appearance is quite close, and (iii) the two light curves are also similar, we speculate that brightening “S” may be associated with brightening “S1.”

With the extension of the two ribbons from east to west, brightenings “T” and “T1” appear at 11:00:41 UT (Figure 2c). Brightenings “T” and “T1” may be conjugate footpoints, because they appear at the same time and have similar time profiles during Phase 1 (Figure 2e).

After Phase 4, we identify the EUV conjugate footpoints mainly by factors (2) and (3), since many brightenings appear simultaneously, and postflare loops are seen for these kernels. Although the correlation between the light curves of some of these conjugate footpoints is not clear, they can be confirmed by the corresponding postflare loops. For example, many EUV brightening pairs appear at HXR Peak 5, but the conjugate nature of footpoints “I”/“I1,” “H”/“H1,” “G”/“G1,” and “F”/“F1” may be confirmed from the appearance of postflare loops (Figure 5c) connecting them.

For some conjugate brightening pairs before 11:04:05 UT, we do not see the expected postflare loops, but this does not mean that they are not conjugate footpoints. Cargill, Mariska, and Antiochos (1995) derived a simple formula for the cooling time of high-temperature flare plasma, which is $\tau_{\mathrm{cool}} \approx 2.35 \times 10^{-2} L^{5/6} / T_0^{1/6} n_0^{1/6}$ s. The parameters L, T_0, and n_0 in the formula are the loop half-length, electron temperature, and electron density, respectively. From the formula we can see that the most sensitive parameter is the loop length. The distance between the earlier brightening pairs before Phase 5 is much longer than that between the later brightening pairs (Figures 2 – 8). Because of their large separation along the neutral line, these early loops are two to three times longer than the later loops, so it should take substantially longer for the earlier loops to cool down to the TRACE/EUV observational temperature range than the later ones. By the time they cool down to the TRACE temperature range, the shielding by the overlying loops makes them unobservable.

Table II gives a summary of the brightenings occurring in the different phases of the flare. Note that the different phases in this table just refer to the different time bins and they do not have physical implication. The start and end times of the phases

TABLE II

Summary of the bright kernels occurring in different phases of the October 28, 2003 flare.

Phase		TRACE (195 Å) Brightening kernels					Ribbon	Angle θ (°)
Phase 1 (Figure 2)				T	S		S	
10:58:21 – 11:02:10				T1	S1		N	73, 71
Phase 2 (Figure 3)	C			B		A	S	
11:02:11 – 11:02:55				B1		A1	N	54
Phase 3 (Figure 4)	C			D			S	
11:02:56 – 11:03:27				D1			N	50
Phase 4 (Figure 4)				E			S	
11:03:28 – 11:04:04				E1			N	41
Phase 5 (Figure 5)	F		H	G	I			
11:04:05 – 11:04:47	F1		H1	G1	I1		N	18
Phase 6 (Figure 6)	M		K	J	L		S	
11:04:48 – 11:05:19			K1	J1	L1		N	19
Phase 7 (Figure 7)		N		O			S	
11:05:20 – 11:06:29		N1		O1			N	9, 23
Phase 8 (Figure 8)	P	Q					S	
11:06:30 – 11:07:46	P1	Q1					N	20

are displayed in the first column. The middle columns give the identifying labels of the different bright kernels in each ribbon. The grouping of the identifying letters into different vertical columns (e.g., "T"/"T1," "B"/"B1," "D"/"D1," "E"/"E1") indicates the evolution of a pair of conjugate footpoints through the stages of its evolution. The middle column marked between the two vertical lines represents the strongest brightening pairs, and the positions of these brightening pairs appear to evolve continuously during the evolution of the flare (especially for the brightenings in the south ribbon). The next column indicates which ribbon (North (N) or South (S)) the bright kernels occurred in. These identifications are then used to define an angle θ, listed in the last column and discussed in the next section.

4.2. Evolution of the Shear of the EUV Conjugate Footpoints

It is well known that filaments typically lie on inversion lines in the longitudinal magnetic field when viewed near the center of the disk (McIntosh, 1972), which also can be seen in Figure 8c. In order to get information about the ribbon's underlying magnetic inversion line, we use the solar filament which can be seen in Hα

image obtained at Big Bear Solar Observatory (BBSO). Because there are no Hα observations at BBSO close in time to the preflare phase, we choose an image late in the day on October 27, 2003, which is about 15 h before this flare.

To get good coalignment of the TRACE/EUV and BBSO/Hα images, we proceeded in three steps: (i) we derotated the Hα image to the same time as the EUV image, and found the SOHO/MDI magnetogram closest in time to the EUV image; (ii) we overlaid the Hα image with the SOHO/MDI magnetogram, using the dark sunspots; (iii) we selected the two images in 195 Å closest in time from SOHO/EIT and TRACE/EUV, and obtained the offset of the TRACE/EUV image by cross-correlation.

In order to examine the evolution of the shear of the EUV conjugate footpoints, we select one image from each time bin; the EUV contours in the different time bins overlaid on the Hα image can be seen in Figures 9a – g, and the conjugate footpoints obtained from our analysis are marked as black lines connecting the bright kernels. The different group of brightening pairs shown in Table II are indicated by different line types in the figure. The evolution of the shear is clearly seen in this sequence of images.

In order to calculate a shear angle, the conjugate brightening pairs during each of the phases connected by the solid, dot-dashed, and dashed lines as shown in the middle column marked between the two vertical lines in Table II are regarded as a group and the angles are averaged. The angles (shear angle) between the lines connecting these conjugate footpoints and the line perpendicular to the filament have been measured and displayed in the last column in Table II. The angles between the lines connected different brightenings pairs in this group are very similar at each phase (time bin) during the early phases (time bins), but become more dispersed after Phase 6. For example, the angle between the line connecting brightening pair "N"/"N1" and the line perpendicular to the filament is very different (23° vs. 9°) from the angles measured for the other brightening pairs seen in Phase 7. All values, however, are retained when taking the average.

Because most of the strongest brightening pairs predominating at the earlier phases (time bins) disappeared by Phase 8, the angle θ is measured using brightening pair "Q"/"Q1," which appears to be related to the brightening pair "N"/"N1" in position. Because the brightening pairs which are associated with the strongest brightening pair "P"/"P1" at Phase 8 are outside of the FOV most of the time, the evolution of this group of brightening pairs is not discussed here.

Furthermore, we have also examined the rate of change of these angles ($-\mathrm{d}\theta/\mathrm{dt}$; we use the average value of θ, if we have more than one value in a given time bin), which is shown in the first column in Table III, and the corresponding time (we use the midpoint between the two times at which we measured the two angles) is displayed in the second column.

The ACS/HXR time profile is displayed in Figure 10a. The temporal evolution of the average shear angle θ and the change rate of this angle $\mathrm{d}\theta/\mathrm{dt}$ are displayed as a solid line with asterisk signs and a dashed line with plus signs, respectively in

TABLE III

Shear angle change rate and the corresponding time.

Time (UT)	11:01:48	11:03:02	11:03:18	11:03:48	11:04:30	11:05:04	11:05:59
$d\theta/dT(°s^{-1})$	0.14	0.33	0.45	0.51	0.03	0.03	−0.07

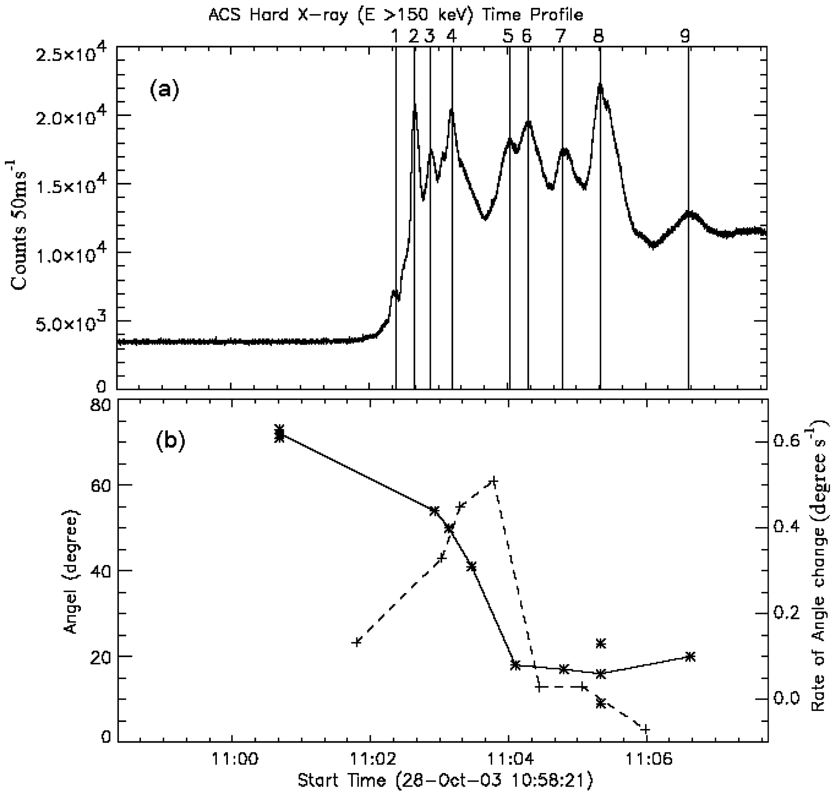

Figure 10. HXR light curve and the temporal evolution of the shear angle and the change rate of this angle. (a) The ACS/HXR light curve of the solar flare on October 28, 2003. (b) The evolution of the shear angle θ (*solid line* with *asterisk sign*), and the evolution of the change rate of this angle (*dashed line* with *plus sign*).

Figure 10b. The real measured angles are shown as individual asterisk signs around the average angle.

From Figure 10b we see that the shear angle θ of the strongest brightening pairs is decreasing all the time during the early impulsive phase, which indicates that the shear of the conjugate footpoints is decreasing during the early impulsive phase (before Peak 6). The change rate of the shear angle peaks during the early impulsive phase, as can be seen in Figure 10b, and the shear change becomes very slow after

Peak 5. It seems, therefore, that the change in shear angle of the EUV brightenings does not correlate in a straightforward way with the impulsive-phase HXR bursts.

5. Discussion

5.1. EUV BRIGHTENINGS GENERATION MECHANISM

As mentioned previously, there are mainly two generation mechanisms for the EUV brightenings: thermal conduction from the reconnected loops, and direct bombardment of the lower atmosphere by accelerated particles from the reconnection site. By the comparison of the EUV and HXR emission, we are able to discuss the EUV brightenings generation mechanism in this event.

Thermal conduction models have been proposed where the initial instability occurs at the loop top where the gas is heated and produces hard X-rays. A thermal conduction front proceeds down the loop to heat the chromosphere to at least transition region temperatures (Smith and Lilliequist, 1979; Smith and Auer, 1980; Nagai, 1980).

TRACE/EUV image overlaid with RHESSI HXR ($E = 100-200\,\mathrm{keV}$) image at the time period of the HXR Spike 9 has been shown in Figure 9 in Krucker and Hudson (2004). From that figure, we can see the HXR sources are located within the two EUV ribbons rather than at the loop top, and we also can see the strongest HXR sources are corresponding to the strongest EUV brightening pair "P"/"P1." These observations suggest that the EUV brightenings during HXR Spike 9 may not be due to thermal conduction.

Unfortunately, we do not have HXR image before HXR spike 9 to check the viability of the thermal conduction model for the other EUV brightenings. However, the travelling time of the thermal conduction front can be estimated as $t = L^2 n_e k_B/\kappa_0 T^{5/2}$ (Yokoyama and Shibata, 1997), where k_B is Boltzmann constant, κ_0 is a physical constant (about 10^{-6} in cgs). Here, L, n_e, and T are the half length of the loop, electron number density, and the temperature of the hot plasma, respectively. Our event is located close to disk center, so we cannot measure the length of the loops directly because of the viewing angle. However, we can measure the distance between the EUV conjugate footpoints. The shortest distance between the EUV conjugate footpoints for Peaks 4, 7, 8, and 9 is approximately 28 800 km, thus the half-length of the shortest loop should be approximately 23 000 km, if we assume a semicircular loop. If we assume that the electron number density and the temperature of the hot plasma are $2 \times 10^{9}\,\mathrm{cm}^{-3}$ and 20 MK, respectively, the travelling time will be 0.94 s, which is comparable to the observed time delay (less than 3 s) between the EUV and HXR emission. This means that we cannot rule out thermal conduction as the cause of the EUV brightenings. However, we should note that the temperature is the most sensitive parameter in this equation: the higher the temperature is, the shorter the travelling time is. The temperature that we used above is within the range of Fe XXIV emission, which starts to appear after Peak 9, as can be seen in Figure 5c, so this travelling time may be only appropriate for the later brightenings after Peak 9. However, due to the lack of HXR observations with spatial resolution, we cannot rule out the possibility that the HXR emission is from a hot ($T > 20$ MK) loop-top source; therefore, we cannot rule out the possibility of the thermal conduction.

As mentioned in Section 3.2, the observations show that the preflare EUV brightenings are similar to the later flare ones in most respects, differing mainly in intensity. Therefore, we speculate that the pre-HXR EUV brightenings have the same generation mechanism as the flare ones. Why can we see EUV brightenings before the HXR onset in this event? The EUV observations show that the pre-HXR EUV bursts are much weaker than the later ones, as can be seen from the summed EUV light curves in the bottom panel of Figure 1. Given the high count rates and good statistics seen in the HXR for all of the flare peaks, the HXR sensitivity does not seem to be an issue. We therefore suggest that the energy released from the reconnection site may be relatively low during the rising phase, so that there is less contribution to the HXR emission in the SPI/ACS energy band ($E > 150$ keV).

5.2. Evolution of the Magnetic Shear

The EUV bright kernels are argued to represent the chromospheric footpoints of the newly reconnected flare loops. Therefore, we can to some extent infer the magnetic field connectivity by observation of the evolution of the EUV footpoints.

In order to study the shear change, the strongest brightening pairs of EUV footpoints, which represent the major energy release site are selected. A strong to weak shear change is observed during the impulsive phase, which confirms the earlier results found at other wavelengths (Masuda, Kosugi, and Hudson, 2001; Asai *et al.*, 2003; Kundu, Schmahl, and Garaimov, 2004). The decrease of the shear of the EUV footpoints implies that the newly reconnected loops have a lesser magnetic shear.

However, we also would like to know what these observations can tell us about the flare magnetic topology. The observed shear change can be understood in terms of the standard model for solar flares (e.g., Moore, LaRosa, and Orwig, 1995; Moore *et al.*, 2001). According to this model the preflare magnetic field contains a highly sheared core field overlying the magnetic inversion line (MIL) on the photosphere. It is assumed that the preflare configuration evolves appropriately for the sheared core field to become eruptively unstable, and that the flare begins with the onset of the core eruption. Magnetic field begins to reconnect just below the rising core field, producing newly reconnected loops that, though less sheared than the preflare core field, retain some obvious shear (see Figure 1 in Moore, LaRosa, and Orwig, 1995). This indicates that, soon after the start of the eruption, the reconnection site is located at some height above the photosphere, inside the sheared envelope field.

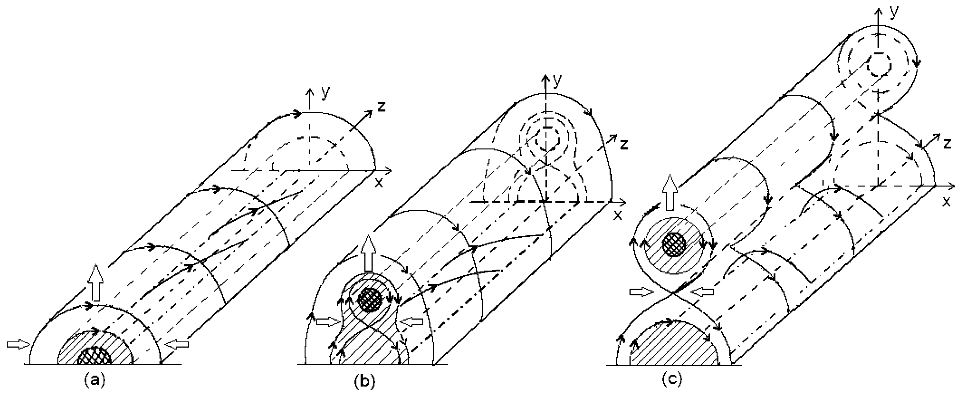

Figure 11. Cartoon of the evolution of the magnetic field in the standard model of solar flares. (a) Preflare magnetic field configuration with greatly sheared core field region (double hatched) surrounded by relatively less but still highly sheared envelope field (single hatched), which is underlying the unsheared envelope field. (b) Magnetic reconnection occurs in the highly sheared envelope field region. (c) The sheared envelope field splits completely, and magnetic reconnection occurs in the region where the field is unsheared. The direction of the magnetic field is represented by the *arrows* on the field lines. Note that the double-hatched shadings indicate magnetic shear, not the presence of cool plasma (Hα filament).

This reconnection causes the sheared envelope to split into two parts during the early phase of the flare. The upper part is ejected into the heliosphere, while the lower part stays behind on the sun.

Figure 11 illustrates the evolution of the magnetic field in the early phase of the flare according to the standard model, but focusing on the evolution of the shear of the magnetic field. We use a Cartesian coordinate system (x, y, z) with the origin lying on the MIL in the photosphere; x is the horizontal coordinate perpendicular to the MIL, y is the height above the photosphere ($y \geq 0$), and z is the distance along the MIL. Figure 11a shows the magnetic configuration well before the flare at a time when flare-related reconnection has not yet occurred. Figure 11b shows the configuration in the early phase of the flare when the main reconnection has already started. The transition from Figure 11a to Figure 11b may take 1 h or even longer. It is unclear exactly how this transition occurs. A detailed model of the magnetic field evolution during this period is beyond the scope of this paper.

It is useful to divide the initial magnetic field configuration into three parts: (1) the inner part is a bundle of greatly sheared core field (double hatched) located just above the MIL; (2) the envelope field immediately coating the sheared core bundle is relatively less but still highly sheared (single hatched); (3) the outmost part is unsheared magnetic field overlying the immediate sheared envelope (Figure 11a). Note that the shear of the magnetic field transitions gradually between these regions.

The observed high shear during the early impulsive phase indicates that magnetic reconnection occurred in the region where the magnetic field (highly sheared, within the immediate sheared envelope region of Figure 11b) has a strong component along the direction of the magnetic inversion line. With the expansion of the sheared core flux bundle, the reconnection line moves upward, and the reconnection region moves out progressively. Therefore, the shear of the newly reconnected loops decreases progressively, which can explain the progressive decrease of the shear of the footpoints with the ribbon separation (Figures 9a – d).

The sheared envelope soon splits into two separate parts: an upper part that moves away from the sun and a lower part that stays behind in the low corona (Figure 11c). Magnetic reconnection occurs at an X-line located between the upper and lower parts of the sheared envelope field. As the eruption proceeds, the upper and lower parts of the sheared envelope field become more and more clearly separated, and the B_z component of magnetic field at the X-line decreases. Therefore, during the later phase, the newly reconnected loops are weakly sheared, as shown in Figure 11c. This model provides a natural explanation for the observed shear change.

At 11:04 UT, the shear angle is about 20°, and little change in shear angle occurs after that time (Figure 10). This suggests that the splitting of the sheared envelope field is nearly complete at 11:04 UT, in the middle of the impulsive phase. Hence, there is no obvious relationship between the splitting of the sheared envelope field and the end of the impulsive phase.

6. Conclusions

An X17 class (GOES soft X-ray) two-ribbon solar flare which occurred on October 28, 2003 is studied in this paper. Comparison of the light curves of the EUV emission from the brightenings within the two ribbons observed by TRACE and the HXR ($E > 150$ keV, SPI/ACS) emission show very good correlation, and we have also found that most of the individual peaks in the HXR bursts can be identified with EUV peaks from one or more bright kernels. The cross-correlation between the light curves of the two types of emission shows that the typical time delay between the EUV and HXR emission is less than 3 s in this event. The comparison of the HXR ($E = 100 – 200$ keV, RHESSI) and EUV image at Phase 8 shows that the HXR sources are located at the EUV bright points. Although all of these observations seem to be favorable to the explanation that the EUV brightenings are mainly caused by direct bombardment at the lower atmosphere of the energetic particles accelerated at the reconnection site, we cannot rule out the possibility of thermal conduction, since the travelling time of the thermal conduction front can be comparable to the observed time delay between the EUV and HXR emission, if the HXR emission is from a very high temperature ($T > 20$ MK) loop-top source. Good data sets observed simultaneously by TRACE, RHESSI, and the Solar-B/XRT, which will be launched in 2006 will be helpful in obtaining a more conclusive result in this topic.

The onset of the EUV brightenings is about 3 min earlier than the HXR emission. These pre-HXR EUV brightenings appear to be associated with the flare ones in position, and these two kinds of brightenings do not have any obvious major difference. Some of the flare brightenings are also seen before the HXR onset, such as brightening "A." All of these observations may suggest that the pre-HXR EUV brightenings have the same generation mechanism as the flare ones.

The EUV conjugate footpoints start at a position close to the magnetic inversion line but widely separated along the inversion line (highly sheared), and change into far from and straight across the inversion line (less sheared) gradually during the impulsive phase. This evolution of the EUV footpoints from strong to weak shear confirms the earlier results reported at other wavelengthes. This suggests that the observed evolution in shear during the initial stages of a flare may be a frequent occurrence. We propose an interpretation in terms of the splitting of the sheared envelope field of the greatly sheared core rope overlying the magnetic inversion line during the early phase of the event. It is clear now, there must be some sheared field left behind on the sun, but what is the fraction of this kind of sheared field, or how much sheared filed has been erupted? A lot of work needs to be done in order to answer this question.

Our most significant new result is that the shear (between the strongest EUV footpoints) change was very fast during the early impulsive phase, but stopped in the middle of the impulsive phase. This result may indicate that the sheared envelope field is split completely in the middle of the impulsive phase. This observation also gives a negative answer to our initial question: the magnetic shear change *per se* does not seem to be the reason for the transition from the impulsive phase to the main phase. More detailed studies of magnetic reconnection and particle acceleration in flares are needed in order to answer this question.

Acknowledgements

The authors thank the anonymous referee for the constructive suggestions to improve the level of this paper. The authors sincerely thank Dr. Spiro Antiochos, Dr. Jun Lin, and Dr. Guangli Huang for helpful discussions. Y.N. Su is grateful to Dr. Ed DeLuca, Dr. Mark Weber, and Dr. Jonathan Cirtain for their help with data reduction, and she also would like to thank Dr. Brigitte Schmieder, Dr. Arek Berlicki, and Dr. Pascal Démoulin for useful discussions and their hospitality during her stay in Meudon. Y. N. Su is also grateful to Dr. Jiong Qiu and Dr. Haisheng Ji for their help with BBSO data process. The authors wish to thank the team of TRACE, SPI/ACS, SOHO/MDI, SOHO/EIT, and NJIT/BBSO for providing the valuable data, and especially thank Dr. Andrei Bykov for letting them use his private SPI/ACS data. The TRACE analysis was supported at Smithsonian Astrophysics Observatory (SAO) by a contract from Lockheed Martin. Y.N. Su was also supported by SAO Predoctoral Fellowship and the NSFC projects No. 10333030 and 10273025.

References

Asai, A., Ishii, T.T., Kurokawa, H., Yokoyama, T., and Shimojo, M.: 2003, *Astrophys. J.* **586**, 624.

Attié, D., Cordier, B., Gros, M., Laurent, Ph., Schanne, S., Tauzin, G. *et al.*: 2003, *Astron. Astrophys.* **411**, L71.

Cargill, P.J., Mariska, J.T., and Antiochos, S.P.: 1995, *Astrophys. J.* **439**, 1034.

Carmichael, H.: 1964, in W.N. Hess (ed.), *NASA Symposium on The Physics of Solar Flares, NASA SP-50*, NASA, Washington, p. 451.

Cheng, C.-C., Tandberg-Hanssen, E., Bruner, E.C., Orwig, L., Frost, K.J., Kenny, P.J., Woodgate, B.E., Shine, R.A.: 1981, *Astrophys. J.* **248**, L39.

Cheng, C.-C., Tandberg-Hanssen, E., and Orwig, L.E.: 1984, *Astrophys. J.* **278**, 853.

Fletcher, L.: 2002, in A. Wilson (ed.), Solar Variability: *From Core to Outer Frontiers, ESA SP-506*, ESA Publications Division, Noordwijk, The Netherland, p. 223.

Fletcher, L. and Hudson, H.: 2001, *Solar Phys.* **204**, 69.

Fletcher, L., Pollock, J.A., and Potts, H.E.: 2004, *Solar Phys.* **222**, 279.

Golub, L., Bookbinder, J., DeLuca, E., Karovska, M., Warren, H., Schrijver, C.J., Shine, R., Tarbell, T., Title, A., Wolfson, J., Handy, B., and Kankelborg, C.: 1999, *Phys. Plasmas* **6**, 2205.

Gros, M., Tatischeff, V., Kiener, J., Cordier, B., Chapuis, C., Weidenspointner, G., Vedrenne, G., von Kienlin, A., Diehl, R., Bykov, A., Méndez, M.: 2004, in V. Schönfelder, G. Lichti, and C. Winkler (eds.), *Proceedings of the 5th INTEGRAL Workshop on the INTEGRAL Universe, ESA SP-552*, ESA Publications Division, Noordwijk, The Netherland, p. 669.

Handy, B.N., Acton, L.W., Kankelborg, C.C., Wolfson, C.J., Akin, D.J., Bruner, M.E. *et al.*: 1999, *Solar Phys.* **187**, 229.

Hirayama, T.: 1974, *Solar Phys.* **34**, 323.

Huang, G.L. and Ji, H.: 2005, *Solar Phys.* **229**, 227.

Ji, H., Wang, H., Goode, P.R., Jiang, Y., and Yurchyshyn, V.: 2004a, *Astrophys. J.* **607**, L55.

Ji, H., Wang, H., Schmahl, E.J., Qiu, J., and Zhang, Y.: 2004b, *Astrophys. J.* **605**, 938.

Kane, S.R., Frost, K.J., and Donnelly, R.F.: 1979, *Astrophys. J.* **234**, 669.

Kopp, R.A. and Pneuman, G.W.: 1976, *Solar Phys.* **50**, 85.

Krucker, S. and Hudson, H.S.: 2004, in R.W. Walsh, J. Ireland, D. Danesy, and B. Fleck (eds.), *Proceedings of the SOHO 15 Workshop, ESA SP-575*, ESA Publications Division, Noordwijk, The Netherland, p. 247.

Kundu, M.R., Schmahl, E.J., and Garaimmov, V.I.: 2004, in A.V. Stepanov, E.E. Benevolenskaya, and A.G. Kosovichev (eds.), *Multi-Wavelength Investigations of Solar Activity, IAU Symp.* **223**, Cambridge University Press, Cambridge; New York p. 425.

Kuznetsov, S.N., Kurt, V.G., Yushkov, B.Y., Myagkova, I.N., and Kudela, K.: 2006, *Solar System Research* **40**, 104.

Lin, A.C., Nightingale, R.W., and Tarbell, T.: 2001, *Solar Phys.* **198**, 385.

Masuda, S., Kosugi, T., and Hudson, H.S.: 2001, *Solar Phys.* **204**, 57.

McIntosh, P.S.: 1972, in P.S. McIntosh and M. Dryer (eds.), *Solar Activity Observations and Predictions*, MIT press, Cambridge, Massachusetts, p. 65.

Moore, R.L., LaRosa, T.N., and Orwig, L.E.: 1995, *Astrophys. J.* **438**, 935.

Moore, R.L., Sterling, A.C., Hudson, H.S., and Lemen, J.R.: 2001, *Astrophys. J.* **552**, 833.

Nagai, F.: 1980, *Solar Phys.* **68**, 351.

Schmieder, B., Mandrini, C.H., Démoulin, P., Pariat, E., Berlicki, A., and Deluca, E.: 2006, *Adv. Space Res.* **37**, 1313.

Smith, D.F. and Auer, L.H.: 1980, *Astrophys. J.* **238**, 1126.

Smith, D.F. and Lilliequist, C.G.: 1979, *Astrophys. J.* **232**, 582.

Sturrock, P.A.: 1966, *Nature* **211**, 695.

Svestka, Z.: 1992, in Z. Svestka, B.V. Jackson, and M.E. Machado (eds.), *Eruptive Solar Flares*, Springer-Verlag, New York, p. 1.

Vedrenne, G., Roques, J.-P., Schönfelder, V., Mandrou, P., Lichti, G.G., von Kienlin, A. *et al*.: 2003, *Astron. Astrophys.* **411**, L63.

Wang, Y.M., Ye, P.Z., Zhou, G.P., Wang, S.J., Wang, S., Yan, Y.H., and Wang, J.X.: 2005, *Solar Phys.* **226**, 337.

Warren, H.P. and Warshall, A.D.: 2001, *Astrophys. J.* **560**, L87.

Woodgate, B.E., Shine, R.A., Poland, A.I., and Orwig, L.E.: 1983, *Astrophys. J.* **265**, 530.

Yokoyama, T. and Shibata, K.: 1997, *Astrophys. J.* **474**, L61.

VOLUME 655 NUMBER 1, PART 1

THE ASTROPHYSICAL JOURNAL

2007 JANUARY 20

(*Continued on inside page*)

PUBLISHED BY THE UNIVERSITY OF CHICAGO PRESS FOR
THE AMERICAN ASTRONOMICAL SOCIETY

ASJOAB 655(1, Pt. 1) 1–684 (2007)

(*Continued from front cover*)

(*Continued on following page*)

The Astrophysical Journal, 655:606–614, 2007 January 20

A STATISTICAL STUDY OF SHEAR MOTION OF THE FOOTPOINTS IN TWO-RIBBON FLARES

Yingna Su,[1,2] Leon Golub,[2] and Adriaan A. Van Ballegooijen[2]

Received 2006 September 13; accepted 2006 October 9

ABSTRACT

We present a statistical investigation of shear motion of the ultraviolet (UV) or extreme-ultraviolet (EUV) footpoints in two-ribbon flares, using the high spatial resolution data obtained in 1998–2005 by *TRACE*. To do this study, we have selected 50 well-observed X and M class two-ribbon flares as our sample. All 50 of these flares are classified into three types based on the motions of the footpoints with respect to the magnetic field (*SOHO* MDI). The relation between our classification scheme and the traditional classification scheme (i.e., "ejective" and "confined" flares) is discussed. We have found that 86% (43 out of 50) of these flares show both strong-to-weak shear change of footpoints and ribbon separation (type I flares), and 14% of the flares show no measurable shear change of conjugate footpoints, including two flares with very small ribbon separation (type II flares) and five flares having no ribbon separation at all through the entire flare process (type III flares). Shear motion of footpoints is thus a common feature in two-ribbon flares. A detailed analysis of the type I flares shows (1) for a subset of 20 flares, the initial and final shear angles of the footpoints are mainly in the range 50°–80° and 15°–55°, respectively; and (2) in 10 of the 14 flares having both measured shear angle and corresponding hard X-ray observations, the cessation of shear change is 0–2 minutes earlier than the end of the impulsive phase, which may suggest that the change from impulsive to gradual phase is related to magnetic shear change.

Subject headings: Sun: corona — Sun: flares — Sun: magnetic fields — Sun: UV radiation

1. INTRODUCTION

Solar flares can be grouped according to the number of ribbons, from unresolved compact pointlike flares to four-ribbon flares. The most commonly seen chromospheric flare morphology is the two-ribbon flare, according to Tang (1985). It is well known that ribbons of large two-ribbon flares separate as a function of time. This ribbon separation is interpreted as the chromospheric signature of the progressive magnetic reconnection in the corona, in which new magnetic field lines reconnect at higher and higher altitudes, according to the two-dimensional classical "CSHKP" model for two-ribbon flares (Svestka & Cliver 1992).

After analyzing 31 flares observed by the Hard X-Ray telescope (HXT) on board *Yohkoh*, Bogachev et al. (2005) classified the footpoint motions into three types: (1) motion away from and nearly perpendicular to the magnetic inversion line (MIL) (ribbon separation), (2) motion mainly along the MIL and in antiparallel directions (shear motion), and (3) parallel motion in the same direction along the MIL. Furthermore, they found that 14 out of their 31 flares show the second type of motion, which often appears as strong-to-weak shear change of the footpoints during a flare. This shear motion was also found in several individual two-ribbon flares (Ji et al. 2006; Su et al. 2006, hereafter Paper I, and references therein). This motion cannot be explained by a simplified two-dimensional flaring model, but it is instead consistent with a three-dimensional magnetic field configuration having highly sheared inner and less sheared outer magnetic field lines in the preflare phase (Moore et al. 1995 and references therein). The cessation of shear change during the impulsive phase can be interpreted as a splitting of the envelope of the highly sheared core field, according to Paper I.

So far, this change from strong to weak shear of the footpoints during the flare has been reported in almost 20 solar flares, which suggests that this motion may be a common feature in solar flares. In this paper we have made a detailed statistical study of the shear motion of the footpoints in 50 two-ribbon flares using high spatial resolution extreme-ultraviolet (EUV)/ultraviolet (UV) images obtained with the *Transition Region and Corona Explorer* (*TRACE*; Handy et al. 1999), in order to make a conclusive statement about the prevalence of shear motion of footpoints in such flares. Our flares are classified into three groups: type I flares, which show both ribbon separation and shear motion; type II flares, which show only ribbon separation; and type III flares, which show no footpoint motion.

It is often considered that, to a first approximation, the life history of a flare consists of an impulsive phase, characterized by mainly nonthermal emissions (hard X-rays, gamma rays, radio waves, and neutrons) and a gradual (main) phase characterized by predominantly thermal emissions (soft X-rays, UV, and optical radiation; Tandberg-Hanssen & Emslie 1988). The impulsive and gradual phases can also be recognized on the basis of hard X-ray (HXR) and microwave time profiles. The impulsive emissions have a short timescale, of order several tens of seconds to a few minutes, and gradual emissions evolve over a longer timescale of tens of minutes. The distinction between the two turns out to be more than superficial and is not limited to temporal properties. Statistical and case studies in the last two decades revealed other respects in which the impulsive and gradual emissions show contrasting properties (for a detailed review see Qiu et al. 2004 and references therein).

The physical differences between the flare impulsive phase and gradual phase are pronounced, and the transition from impulsive phase to main phase is typically abrupt. What is the nature of the change that occurs when a flare goes from the impulsive phase to the gradual phase? The magnetic field strength per se is unlikely to change abruptly, but the magnetic shear may show abrupt temporal gradients. Therefore, Lynch et al. (2004) suggested that the observed cessation of HXR bursts with the start of the main phase can be understood in terms of the difference between reconnection in a strongly sheared versus an unsheared

[1] Purple Mountain Observatory, Nanjing, China; and Graduate University of Chinese Academy of Sciences, China.

[2] Current address: Harvard-Smithsonian Center for Astrophysics, Cambridge, MA; ynsu@head.cfa.harvard.edu.

field. This hypothesis has been examined in detail for one flare in our previous paper (Paper I). The observations showed that the cessation of shear change of footpoints occurs in the middle of the impulsive phase. However, it is difficult to draw a conclusive statement on this question from this one case study. In this paper we examine the time difference between the cessation of the shear motion and the end of the impulsive phase in a sample of 14 events having both measurable shear angle and corresponding HXR observations.

The observational data are summarized in § 2. In § 3.1 we present the study of type I flares. The observational results of type II and III flares are described in § 3.2. In §§ 4.1 and 4.2 we compare our classification scheme (type I, II, and III flares) with that of Svestka (1986) ("ejective" and "confined" flares), and an energy scale for two-ribbon flares is described in § 4.3. The time difference between the cessation of shear motion and the end of impulsive phase in type I flares is presented in § 5. Summary is given in § 6.

2. OBSERVATIONAL DATA

We construct our data sets based on the *TRACE* Flare Catalog,[3] provided by the Solar and Stellar X-Ray Group at Smithsonian Astrophysical Observatory, which lists all of those X and M class flares (*GOES* soft X-ray) from 1998 May to the present time (and those C class flares from 1998 to 2002, and they are not cataloged after this) observed by *TRACE*. The *TRACE* Flare Catalog is formed by selecting those flare events having *TRACE* observations around the flare peak time reported by *GOES*. The information of the class and peak time of the flares listed in the *TRACE* Flare Catalog is taken from the *GOES* Flare Catalog.[4] We have selected 50 well-observed two-ribbon solar flares from 1998 to 2005, according to the following criteria:

1. We only consider flares in which two long and roughly parallel ribbons are seen during the flare.
2. Most parts of the two ribbons are visible within the field of view (FOV) of *TRACE*.
3. *TRACE* obtained several good images during the rise and impulsive phase, from which we can see the two ribbons and their evolution clearly.
4. Flares near the limb for which the two ribbons and their evolution cannot be seen are not considered.

All of the flares we included in this study are listed in Tables 1 and 2.

The *TRACE* mission explores the dynamics and evolution of the solar atmosphere from the photosphere to the corona with high spatial and temporal resolution (Handy et al. 1999). It observes the white-light photosphere, the transition region at the wavelengths of 1216, 1550, and 1600 Å, and the 1–2 MK corona at 171, 195, and 284 Å. However, because of its limited FOV, *TRACE* may miss observing some flares, if these flares happen outside the FOV (Zhang et al. 2002). We have used the *TRACE* catalog, understanding that it will not be a complete sample of all flares occurring during the studied period because the *TRACE* observations of flares provide high spatial and temporal resolution images, which make possible the study of shear motion of the footpoints.

The HXR time profiles used in this study from 1998 to 2001 are taken from the *Yohkoh* Flare Catalog.[5] *Yohkoh* HXT (Kosugi et al. 1991) used a Fourier synthesis technique to take images in four energy bands (L: 13–23 keV; M1: 23–33 keV; M2: 33–53 keV; H: 53–93 keV) with a collimator response (FWHM) of about 8″. For those flares that occurred after 2001, the HXR data are obtained from *RHESSI*. *RHESSI* provides unprecedented high-resolution imaging and spectroscopy capability for solar flares (Lin et al. 2002). For the analysis, we use the energy band 33–53 keV for both *Yohkoh* HXT and *RHESSI*, since lower energy bands may have a considerable contribution from the superhot plasma emission. We could also use a higher energy band, but the HXR emission is usually too weak in those bands to define the end of the impulsive phase with proper accuracy.

The magnetic inversion line information in most events used in this study is from the line-of-sight photospheric magnetograms observed by the Michelson Doppler Imager (MDI) on board the *Solar and Heliospheric Observatory* (*SOHO*). For those events that do not have corresponding MDI observations, or if the MIL on the MDI magnetograms is too complicated, the MIL is identified by the corresponding filament on the Hα images observed by Big Bear Solar Observatory (BBSO). Information about related coronal mass ejections (CMEs) is obtained from the *SOHO* Large Angle and Spectrometric Coronagraph Experiment (LASCO) CME Catalog.[6]

3. THREE TYPES OF TWO-RIBBON FLARES

Of the available *TRACE* passbands, more than half of the events we studied were mainly observed only in the EUV (171/195 Å) or UV (1600/1700 Å), and less than half of them were observed with a sequence that took a combination of EUV (171/195/284 Å) and UV (1600/1216/1550 Å) images. In order to study shear motion of the footpoints, our first step is to look through all of the movies at the wavelength in the main observing sequence for each event, i.e., the wavelength that has the best coverage of the event. The motion of the brightenings can be seen clearly from the movies and is visible in either UV or EUV channels. To make a detailed study, we first synthesized a set of *TRACE* images at the wavelength in main observing sequence for each event. In order to distinguish the motions of footpoints with respect to the magnetic field, the next step is to co-align the *TRACE* images with the corresponding magnetic field or Hα images. To get good co-alignment of the EUV/UV (*TRACE*) and *SOHO* MDI magnetograms or BBSO Hα image, we proceeded in three steps: (1) aligned the EUV/UV images with the white-light (WL) images observed by *TRACE* using the "trace_prep.pro" program provided as part of the *TRACE* analysis software; (2) aligned the WL images with the *SOHO* MDI magnetograms or BBSO Hα images, using the dark sunspots; (3) aligned the EUV/UV images with the *SOHO* MDI images or BBSO Hα images using the offsets obtained from the first two steps.

After studying the motions of the brightenings observed by *TRACE* with respect to the magnetic field, we found that our events could be categorized into three groups:

Type I flares.—The common characteristic among all flares in this group is that the EUV conjugate footpoints start at a position close to the magnetic inversion line but widely separated along the MIL (highly sheared) and change into a configuration far from and straight across the inversion line (less sheared) during the impulsive phase. In other words, this type of flare shows strong-to-weak shear motion of the footpoints and also ribbon separation.

An example of a type I flare on 2001 April 26 is shown in Figure 1. Figure 1*a* represents the HXR time profiles obtained from *Yohkoh* HXT. The *TRACE* EUV initial brightenings (*white contours*) at the flare onset overlaid on the EUV image having the final brightenings at the time when the shear change stops are

[3] See http://hea-www.harvard.edu/trace/flare_catalog/.
[4] See http://www.lmsal.com/SXT/plot_goes.html.
[5] See http://gedas22.stelab.nagoya-u.ac.jp/HXT/catalogue/index.html.
[6] See http://cdaw.gsfc.nasa.gov/CME_list/index.html.

TABLE 1
Type I Flares with Shear Motion and Ribbon Separation

Date	GOES Class	TRACE Observed Band(s) (Å)	TRACE Shear Angle θ_1[a] (deg)	θ_2[a] (deg)	$\theta_1 - \theta_2$ (deg)	Time t_{EUV1}[b] (UT)	t_{EUV2}[b] (UT)	t_{HXR}[c] (UT)	$t_{HXR} - t_{EUV2}$ (s)	GOES Peak (UT)	CME Onset (UT)
1998 Sep 23	M7.1	1550, 195	...	...	...	...	...	...	...	07:13	No data
1999 Jun 22	M1.7	1216, 195, 171	52±2	31±2	21	18:20:26	18:24:51	18:23	−111	18:29	18:54
1999 Jun 23	M1.7	1216, 195, 171	56±2	32±2	24	06:50:42	06:57:02	...	...	07:09	07:31
2000 Feb 08	M1.3	171, 1600	65±2	19±2	46	08:44:05	08:49:32	08:51:55	143	09:00	09:30
2000 Apr 12	M1.3	171	...	...	...	...	...	...	...	03:35	No
2000 Jun 04	M3.2	171, 1600	67±2	49±2	16	22:06	22:09:27	...	...	22:10	23:54
2000 Jun 06	X2.3	171, 1600	...	...	...	...	...	...	...	15:25	15:30
2000 Jun 10	M5.2	195, 1600	51±2	19±2	32	16:47:12	16:53:30	...	...	17:02	17:08
2000 Jul 14	X5.7	195	65±2	23±2	42	10:24:23	10:26:51	10:27	9	10:24	10:54
2000 Nov 08	M7.4	171	...	...	...	...	...	...	...	23:28	23:06
2000 Nov 24	X2.3	1600	...	...	...	...	...	...	...	15:13	15:30
2000 Nov 24	X1.8	1600	57±2	15±2	42	21:49:14	21:52:51	21:54:07	76	21:59	22:06
2001 Jan 20	M1.2	1600	...	...	...	...	...	...	...	18:47	19:31
2001 Jan 20	M7.7	1600	...	...	...	...	...	...	...	21:20	21:30
2001 Mar 24	M1.7	171, 1600	80±2	50±2	30	19:37:53	19:55:05	...	...	19:55	20:50
2001 Apr 09	M7.9	171, 1600	63±2	35±2	28	15:25:02	15:31:27	...	...	15:34	15:54
2001 Apr 10	X2.3	171	53±2	2±2	51	05:08:39	05:17:25	05:19	95	05:26	05:30
2001 Apr 11	M2.3	171	76±2	46±2	30	12:58:27	13:07:46			13:26	13:31
2001 Apr 26	M7.8	171, 1600	51±2	5±2	46	13:07:48	13:09:54	13:10:10	16	13:12	13:31
2001 Jun 15	M6.3	195	...	...	...	...	...	...	...	10:13	10:31
2001 Aug 25	X5.3	284	...	...	...	...	...	...	...	16:45	16:50
2001 Oct 19	X1.6	171	...	...	...	...	...	...	...	16:30	16:50
2001 Dec 26	M7.14	1600	...	...	...	...	...	...	...	05:40	05:30
2002 Mar 14	M5.7	171	61±2	26±2	35	01:42:02	01:47:22	01:46	−82	01:50	23:54
2002 Apr 10	M1.6	195	52±2	27±2	25	19:01:55	19:04:03	19:04:15	12	19:07	20:26
2002 Jul 29	M4.7	171, 1600	...	...	...	...	...	...	...	10:44	No
2002 Jul 31	M1.2	171	50±2	1±2	49	19:37:53	01:51:10	01:51:40	30	01:53	No
2002 Oct 22	M1.0	195	85±2	50±2	35	15:32:18	15:33:25	...	...	15:35	No
2002 Oct 25	M1.5	195	...	...	...	...	...	...	...	17:47	18:06
2003 May 29	X1.2	195, 1600	...	...	...	...	...	...	...	01:05	01:27
2003 May 31	M9.3	195	52±2	29±2	23	02:19:03	02:21:54	...	...	02:24	02:30
2003 Jun 11	X1.6	1700	...	...	...	...	...	...	...	20:14	No data
2003 Aug 19	M2.7	171, 195, 1600	70±2	48±2	22	09:49:45	10:00:24	10:02:22	118	10:06	10:30
2003 Oct 24	M7.6	195, 1600	72±2	41±2	31	02:27:56	02:44:58	02:52:20	440	02:54	02:54
2003 Oct 28	X17.2	195, 1600, 284	78±2	22±2	56	11:00:41	11:04:05	11:05	55	11:10	11:30
2004 Nov 10	X2.5	1600	...	...	...	...	...	...	...	02:13	02:26
2004 Dec 30	M2.2	1600	...	...	...	...	...	...	...	10:47	10:57
2005 Jan 15	X2.6	1600	...	...	...	...	...	...	...	23:02	23:06
2005 May 17	M1.8	171	75±2	36±2	39	02:33:37	02:42:46	02:42:50	4	02:39	03:06
2005 Jul 07	M4.9	171, 1600	61±2	18±2	43	16:07:21	16:20:50	...	...	16:29	17:06
2005 Jul 09	M2.8	171, 1600	48±2	19±2	29	21:55:55	22:05:27	...	...	22:06	22:30
2005 Jul 30	X1.3	171	...	...	...	...	...	...	...	06:35	06:50
2005 Sep 17	M9.8	171, 1600	67±2	46±2	21	06:02:15	06:04:53	06:05:40	47	06:05	No

[a] θ_1 and θ_2 refer to the initial and final shear angles, respectively.
[b] t_{EUV1} and t_{EUV2} refer to the time when the initial and final shear angles are measured, respectively.
[c] The time when the impulsive phase stops.

shown in Figure 1*b*. Figures 1*c* and 1*d* show the initial and final brightenings (*white contours*) overlaid on the later postflare loop images showing the postflare loops connecting these brightenings, respectively. The *TRACE* image at the time when the shear change stops overlaid with photospheric magnetic field contours observed by *SOHO* MDI is shown in Figure 1*e*. Figures 1*f* and 1*g* show how we measure the initial and final shear angle.

Type II flares.—We do not see measurable shear motion of the conjugate brightenings, but we see very small ribbon separation in this type of flare (e.g., Figs. 2*a* and 2*b*).

Type III flares.—We do not see shear motion of the conjugate brightenings, nor ribbon separation in these flares. Two examples of type III flares are shown in Figures 2*c*–2*f*.

3.1. *Type I Flares*

3.1.1. *Footpoint Motion in Type I Flares*

In all, 86% (43 out of 50) of the two-ribbon flares we studied show shear motion of the EUV/UV footpoints during the flare, which indicates that this motion is a common feature in two-ribbon flares. This 86% fraction is much larger than the 45% (14 out of 31) fraction reported by Bogachev et al. (2005). They found that 8 of these 14 flares with shear motion show mainly this shear motion, while the other 6 flares show a combination of ribbon separation and shear motion. However, all of our 86% of flares show a combination of ribbon separation and shear motion. Two reasons that may explain this difference are as follows: (1) Data

TABLE 2

TYPE II AND TYPE III FLARES WITHOUT SHEAR MOTION

Date	*GOES* Class	Observed Band(s) (Å)	*GOES* Peak Time (UT)	Ribbon Separation	CME Onset Time (UT)
2001 May 05[a]	M1.0	171, 1600	08:56	Small	No
2001 Aug 05[b]	M1.7	171, 1600	15:31	No	No
2001 Aug 05[b]	M4.9	171, 1600	22:24	No	No
2001 Oct 31[c]	M3.2	171	08:09	No	No
2001 Nov 10[c]	M1.0	1600	00:50	No	No
2001 Dec 29[c]	M1.1	1600	05:45	No	No
2003 Jan 22[a]	M1.2	171	04:44	Small	05:06

[a] Type II flares.
[b] Type IIIA flares.
[c] Type IIIB flares.

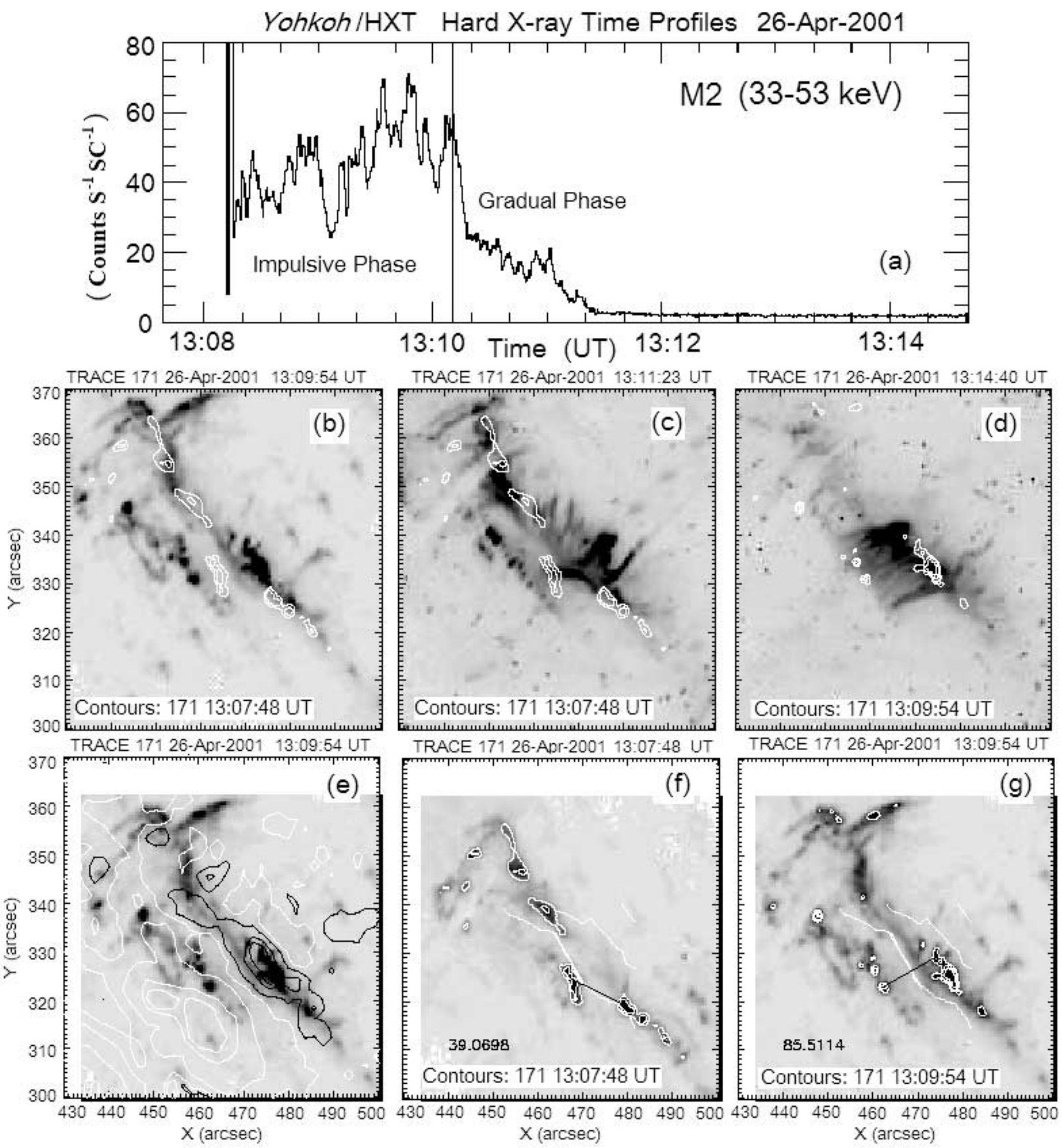

FIG. 1.— Event on 2001 April 26. (*a*) HXR (E = 33–53 keV) time profile observed by *Yohkoh* HXT. The end of the impulsive phase is marked as a vertical line. (*b–d*) EUV images at 171 Å observed by *TRACE* at different times. (*e*) *TRACE* EUV image overlaid with corresponding photospheric magnetic field (*SOHO* MDI) contours. The black and white contours represent the positive and negative magnetic polarities, respectively. (*f*, *g*) *TRACE* EUV images at different times overlaid with white contours that represent the brightenings. The white lines refer to the magnetic inversion line (MIL, *SOHO* MDI), and the thick white lines represent the simplified MIL. The brightenings connected by the black lines are conjugate footpoints.

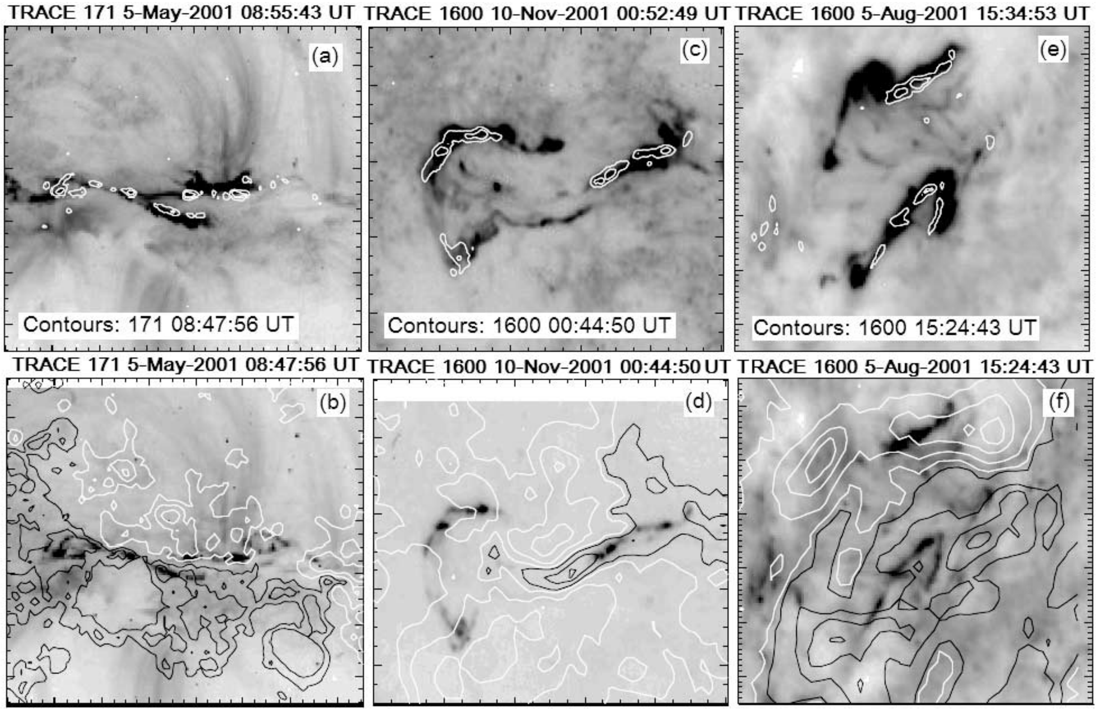

Fig. 2.— Type II and III flares. *Left*: Images for event 2001 May 5, and the FOV is $150'' \times 125''$. (*a*) *TRACE* image at around the *GOES* flare peak time overlaid with white contours representing the bright kernels at the flare onset. (*b*) *TRACE* image at the flare onset overlaid with photospheric magnetic contours. The black and white contours refer to the positive and negative magnetic polarities (*SOHO* MDI), respectively. *Middle*: Similar to the left panels, but for event 2001 November 10, and the FOV is $100'' \times 85''$. *Right:* Similar to the left panels, but for event 2001 August 5, and the FOV is $70'' \times 60''$.

selection criteria are different. All of the flares we selected must have two long and nearly parallel ribbons observed by *TRACE*, which is not required by Bogachev et al. (2005). (2) Bogachev et al. (2005) used HXR data observed by *Yohkoh* HXT ($2.47''$ pixel^{-1}), while we are measuring the EUV/UV footpoints using the much higher spatial resolution ($0.5''$ pixel^{-1}) data observed by *TRACE*.

As mentioned in § 1, there are mainly three types of HXR footpoint motions: ribbon separation, shear motion, and motion in the same direction (Bogachev et al. 2005). In this paper, although we focus our study on the shear motion of EUV/UV footpoints, we have also checked for the other two types of motions, i.e., ribbon separation and motion in the same direction. We have found that all of the 43 type I flares show both ribbon separation and shear motion, and the brightest footpoints in 22 out of the 43 type I flares show "same direction" motion along with the shear motion and ribbon separation. This indicates that a mixture of these three types of motion often exists in two-ribbon eruptive flares.

3.1.2. *Shear Angles of the Footpoints in Type I Flares*

In order to get a quantitative determination of the shear motion of conjugate footpoints, we have selected 24 events out of the 43 type I flares, representing those events for which the MIL information and *TRACE* observations are good enough to (1) represent the magnetic inversion line using a straight line and (2) identify the initial and final conjugate footpoints. The initial and final shear angles of these events have been measured and listed in Table 1. The shear angle is defined as the angle between the line connecting the conjugate footpoints and the line perpendicular to the magnetic inversion line.

We have developed a semiautomatic program to measure the shear angles of these events. The projection effects of events close to the limb have been corrected by moving the source region to the solar disk center in software. The process of measuring the shear angles is described as follows:

1. Inspect and compare all of the EUV/UV images overlaid with magnetic field contours during the flare to select two EUV/UV images. The first image is the one when the initial brightenings (e.g., white contours on Fig. 1*b*) appear, and the second image is the one when the shear change of footpoints stops (e.g., Fig. 1*b*). For those flares without *SOHO* MDI observations, all of the EUV/UV images are shown as contours overlaid on the BBSO Hα image closest in time, and the MIL is indicated by the filament.
2. Select the initial and final conjugate footpoints from the two images. Most events start as two bright kernels appearing on both sides of the MIL. These two bright kernels will be identified as the initial conjugate footpoints if they are subsequently connected by corresponding postflare loops (e.g., Fig. 1*c*). Two long ribbons composed of many bright kernels have been formed by the time the shear motion of the footpoints stops. We choose the brightest brightening pair at the end of shear change as the final conjugate footpoints. Furthermore, the corresponding postflare loops for most of these brightening pairs at this time are roughly parallel to each other (e.g., Fig. 1*d*), which means that the shear angles of most of the brightening pairs are similar.
3. The angle between the line connecting the two conjugate footpoints (black line in Figs. 1*f* and 1*g*) and the simplified magnetic inversion line (thick white line in Figs. 1*f* and 1*g*) is measured using our semiautomatic program. This angle can be measured by clicking the start and end points of the MIL and the two conjugate footpoints on the image. Note that the shear angle is complementary to the angle thus measured.

The various parameters of all type I flares are listed in Table 1. The histogram of event number in terms of the initial and final shear angles (Fig. 3*a*) shows that the initial and final angles in most events are in the range from 50° to 80° and from 15° to 55°,

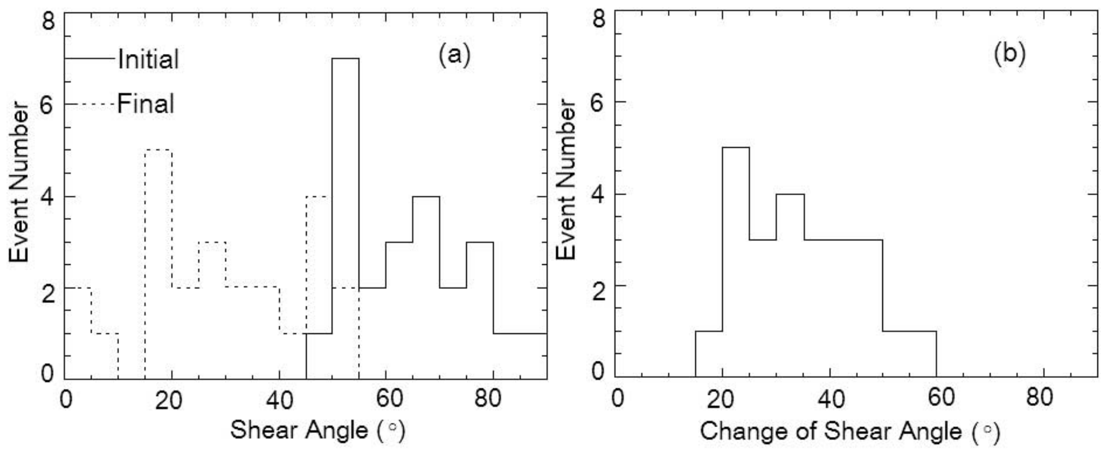

Fig. 3.—Histograms for the 24 type I flares with measured shear angle. (*a*) Histogram of event number in terms of the initial and final shear angles. (*b*) Histogram of event number in terms of the change of shear angle. The bin size in these two histograms is 5°.

respectively. The distribution of the final shear angle may suggest that the magnetic field does not generally relax fully to a potential state (Gibson & Fan 2006b). This is because reconnection under high electrical conductivity approximately conserves the global magnetic helicity, according to Berger & Field (1984). Thus, coronal fields will naturally produce a flux rope, rather than a potential field, as a metastable state (Zhang & Low 2005). It is worth noting here that, due to the uncertainties in our method of measuring shear angle (e.g., we use a simplified straight line to represent the magnetic inversion line), we cannot exclude the possibility that the magnetic field does relax to a fully potential state after the flare for some events, especially those events having final shear angle less than 15°. In order to make sure if the magnetic field relaxes to a fully potential state or not, we should make detailed calculations using the potential magnetic field model, which is beyond the scope of this paper.

Figure 3*b* is the histogram of event number in terms of the change of shear angle, which shows that the change of shear angle is distributed in the range between 15° and 60°.

3.2. *Type II and III Flares*

These types of flares have no obvious shear change of the footpoints. All of these flares have relatively low soft X-ray flux (*GOES* class <M5).

Type II flares (marked as "a" in Table 2) show very small ribbon separation during the flare (e.g., Fig. 2*a*). We found two such events. In both cases, a filament is seen before the flare in both *TRACE* and the Hα images (BBSO). The two ribbons initially appear close to the magnetic inversion line, then move outward very slightly away from the MIL. There is no observable filament activation associated with event 2001 May 5, but a filament eruption is seen to be associated with event 2003 January 22. Both type II flares have single-bipole magnetic field configuration (Fig. 2*b*).

We found five type III events (marked as "b" and "c" in Table 2), in which there is no observed ribbon separation. The brightenings of all type III flares appear at a position far from the magnetic inversion line, and the shear of the conjugate brightenings is very weak at the flare onset. As the flare progresses, the two ribbons may show some expansion along the direction parallel to the inversion line, but there is no motion along the direction perpendicular to the MIL at all throughout the entire flare process (i.e., Figs. 2*c* and 2*e*). Type III flares are divided into two subgroups (i.e., type IIIA and type IIIB marked as "b" and "c" in Table 2, respectively) based on the photospheric magnetic field configuration. The difference between type IIIA and type IIIB flares is that type IIIA flares have a complicated magnetic field configuration (e.g., Fig. 2*d*), whereas type IIIB flares have a simple single-bipole magnetic field configuration (e.g., Fig. 2*f*).

4. EJECTIVE AND CONFINED FLARES

Flares have been categorized in many different ways, but two particular types, the simple-loop (compact or confined) flare and the two-ribbon (dynamic or ejected) flare, may be particularly significant (Pallavicini et al. 1977; Moore et al. 1980; Priest 1981). In compact flares we see brightenings of loops that do not show any apparent expansion, rise, or other kinds of motion. In Hα, the brightened footpoints of the flare stay in the same position until they decay. They do not appear to be associated with filament disruption (which is a characteristic feature of the two-ribbon flares), nor with white-light coronal transients (which are consequences of the filament disruptions; Priest 1981). The two-ribbon flares are much larger and more dramatic than a compact flare and take place near a solar prominence or filament. During the flash phase, two ribbons of Hα emission form, one on each side of the filament (or filament channel), and throughout the main phase the ribbons move apart at 2–10 km s^{-1}. Occasionally, the filament remains intact, although slightly disturbed, but usually it rises and disappears completely (Priest 1981). Following Svestka (1986), the first class of flares are called "confined" flares to emphasize their essential difference from the other classes, and the other class are called "ejective" flares (Machado et al. 1988).

In this section we compare our classification scheme (§ 3) with that of Svestka (1986) and introduce some available models for these flares. We classify those flares having both ribbon separation and corresponding CMEs into the ejective flare category. For some flares we do not find corresponding CMEs from the *SOHO* LASCO CME Catalog, and we call these flares "possibly ejective." Flares having no ribbon separation nor corresponding CMEs are classified into the confined flare category. We regard the flare and CME as associated if the CME onset time (first appearance time at LASCO C2) is within a ± 2 hr time window of the flare peak time and the position of the flare lies in the range of the CME span, defined as the position of the CME $\pm$ half of the CME width $\pm 15°$ (Zhang & Golub 2003). If the CME candidate is a halo CME, then the center of the *TRACE* field must lie within 45° of disk center in both longitude and latitude; otherwise, the latitude of the center position of the *TRACE* field must lie in the range of the CME span, according to Zhang et al. (2002).

4.1. *Ejective or Possibly Ejective Flares*

From Tables 1 and 2 we can see that 36 type I flares plus one type II flare belong to the ejective flare category. For this type of flare, there is now a generally accepted picture for the overall three-dimensional magnetic field and its change during the flare. This standard picture is basically the one proposed by Hirayama (1974), which (with various modifications, refinements, and changes in emphasis) has been adopted by many flare modelers (Moore et al. 1995 and references therein). In this scheme, the flare energy release is driven by the eruption of a magnetic flux rope from the sheared core of a closed bipolar magnetic field (Moore 1988; Forbes 1992). The strong-to-weak shear motion of the footpoints is interpreted as magnetic reconnection progressing from a highly sheared to a less sheared region (Fig. 11 in Paper I). This strong-to-weak shear motion of the footpoints or of the "postflare" loops is seen in a magnetohydrodynamic (MHD) simulation of the nonlinear development of instabilities of magnetically sheared arcades made by Manchester (2003; see his Fig. 2). MHD simulations of the eruption of a three-dimensional flux rope done by Gibson & Fan (2006b) and Manchester et al. (2004) also show this motion (see their Figs. 5*g*–5*i*).

For the other seven type I flares and one type II flare, the corresponding CME information is uncertain. The CME onset times for all of the flares we studied are listed in the last column of Tables 1 and 2. For two flares the CME information is uncertain because there is a gap in LASCO observations (marked as "No data"). For the other six flares, we do not find corresponding CMEs fitting our criteria. Note that although we do not find corresponding CMEs from the LASCO C2 observations, we cannot say that these flares are not associated with CMEs because the associated CME may be too weak to be detected by the *SOHO* LASCO C2. We call these flares possibly ejective flares because they show ribbon separation, but there is no certain corresponding CME information.

For two out of these eight possibly ejective flares, we see obvious filament eruptions in EUV observations made by *TRACE*. Although the corresponding CME information is uncertain, we suggest that these two possibly ejective flares, similar to ejective flares, may also be caused by the ejective eruption of the sheared core field (Moore et al. 2001). It is worth noting that in this scheme, all or part of the filament (sheared core field) is often seen to erupt in association with a flare. However, according to Gibson & Fan (2006a, 2006b), the degree to which the initially dipped field was filled with filament mass, as well as the location of this mass relative to where the flux rope breaks in two, would then determine whether all, some, or none of the filament would actually be observed to erupt and escape with the CME. If only the lower dips were filled with filament mass, the filament might not show any sign of eruption at all, which may explain why we do not see filament eruption in the other six possibly ejective flares (e.g., event 2001 May 5). Since the flux rope or the envelope of the sheared core field can break in two (Gibson & Fan 2006a, 2006b; Paper I), a weak CME may happen if only a smaller upper part of the flux rope (CME) is ejected, and the larger lower part of the flux rope is left behind. Therefore, these six possibly ejective flares may be caused by partial eruption of the flux rope (or sheared core field).

4.2. *Confined Flares*

It is known that ribbons of large two-ribbon flares separate as a function of time, which can be interpreted by the classical two-dimensional magnetic reconnection model discussed in § 1. However, the separation of ribbons is not universal, and we observed several small two-ribbon flares (i.e., type III flares) that have no ribbon separation at all throughout the entire flare process. The ribbons of these flares are not close together at the flare onset and no strong shear of the footpoints is observed either, which is consistent with the earlier results reported by Tang (1985) and Kurokawa (1989).

We find that all five type III flares belong in the confined category for which no corresponding CMEs have been found from the *SOHO* LASCO observations, and all five of these flares have low soft X-ray peak flux (GOES class <M5). These observations suggest that only a small amount of energy is released in these flares; therefore, there might be very little free energy stored prior to the flare.

In the following we discuss our observations in the context of models for confined flares:

1. *Emerging* (*or evolving*) *flux model*.—According to this model, a (small) confined flare occurs if the new flux appears in a region where no great amount of magnetic energy in excess of potential is stored (Heyvaerts et al. 1977; Shibata et al. 1992). All three type IIIA flares have complicated magnetic field configuration, such as in the flare on 2001 November 10 (e.g., Fig. 2*d*): the negative polarity is surrounded by the positive polarities and the magnetic inversion line is strongly contorted; therefore, this MIL can be treated as two magnetic inversion lines. However, the two type IIIB flares have a single bipolar configuration, and the magnetic inversion line is nearly straight. More than one magnetic inversion line is needed to make this model work. Therefore, this model seems possible for the type IIIA flares but may not fit the type IIIB flares.
2. (*Resistive*) *kink instability*.—When a loop is twisted by more than a critical amount, it becomes kink or resistive kink unstable. If ideal kink occurs, the loop may become contorted and develop current sheets in the nonlinear development. If the resistive kink takes place, one or several current sheets form at which the magnetic energy is dissipated (Sakurai 1976; Priest 1981; Gerrard & Hood 2003). A recent simulation done by Török & Kliem (2005) shows that the kink instability of coronal magnetic flux ropes could drive confined eruptions if the decrease of the magnetic field above the flux rope is not steep enough. For our confined flares, we do not see any observational evidence that supports this model, but we also do not have enough observational evidence to rule out this possibility.
3. *Confined explosion of a sheared core bipole*.—The sheared core field and filament undergo an eruption that is soon arrested within the confines of the closed bipole, and the flare has a correspondingly short duration (Moore et al. 2001). This model predicts that the brightenings at the flare onset are highly sheared and close to the inversion line, while our observations show that the brightenings in the five confined (i.e., type III) flares at the flare onset are weakly sheared and far away from the inversion line (e.g., Fig. 2).

4.3. *An Energy Scale for Two-Ribbon Flares*

Table 3 shows the relationship between the two types of classification for all of the flares we studied using different criteria. From Table 3 we can see that ejective flares almost always show shear change of the footpoints (only 1 counterexample out of 37). There are two flares that show ribbon separation but no shear motion. However, shear motion of the footpoints is always accompanied by ribbon separation.

The eruptive or noneruptive behavior of flares is likely determined by the *relative* amount of free energy ε, i.e., the ratio of

TABLE 3
Classification of "Ejective" and "Confined" Flares

Type (Motion)	Ejective (CME)	Possibly Ejective (CME?)	Confined (No CME)
I (RS[a] and SM[b])	36	7	0
II (RS)	1	1	0
III (no motion)	0	0	5

[a] Ribbon separation.
[b] Shear motion.

the magnetic free energy ΔE released in the flare and the energy $\Delta E_{\rm open}$ required to open up the field. For $\varepsilon \geq 1$ sufficient energy is available to produce an eruption, whereas for $\varepsilon \ll 1$ only confined flares are energetically possible. We suggest that this ratio ε also determines the type of footpoint motions that occur within the flare. Figure 4 shows a schematic representation of the flare energy scale sequence of the three types (types I, II, and III) of flares. Type I flares are the most powerful eruptions, which show both shear motion of the footpoints and ribbon separation, and most of these flares are associated with CMEs. This suggests that a large amount of free energy is stored in the corona prior to this type of flare, $\varepsilon \geq 1$. Type II flares are relatively smaller flares, and they only show very small ribbon separation, but no measurable shear change of the footpoints, and only one of the observed type II flares is associated with a CME. These observations may indicate that the free energy stored in the magnetic field in these flares is relatively small, i.e., $\varepsilon < 1$, which causes very small ribbon separation and no obvious shear change of the footpoints. Type III flares show no shear change of the footpoints nor ribbon separation, and no corresponding CMEs. There is for such flares only minor nonpotentiality and thus the energy in the corona prior to eruption is small (Priest & Forbes 2002).

5. TIME DIFFERENCE BETWEEN THE CESSATION OF SHEAR MOTION AND THE END OF IMPULSIVE PHASE IN TYPE I FLARES

We have selected 14 events with good corresponding HXR (*Yohkoh* HXT or *RHESSI*) observations out of the 24 type I flares with measured shear angle, in order to answer the question, could the transition from impulsive to gradual phase be related to the magnetic shear change?

In the impulsive phase of these flares, the HXR and gamma-ray emission rises impulsively, often with many short but intense spikes of emission, each lasting a few seconds to tens of seconds. The end of the impulsive phase in this study is defined as the last peak of the impulsive phase (e.g., the vertical line in Fig. 1*a*). We note that in most events, the time of the end of the impulsive phase is earlier than the *GOES* soft X-ray peak time, which is listed in Table 1. In the gradual phase, the HXR and gamma-ray fluxes start to decay away more or less exponentially with a time constant of minutes (e.g., Fig. 1*a*).

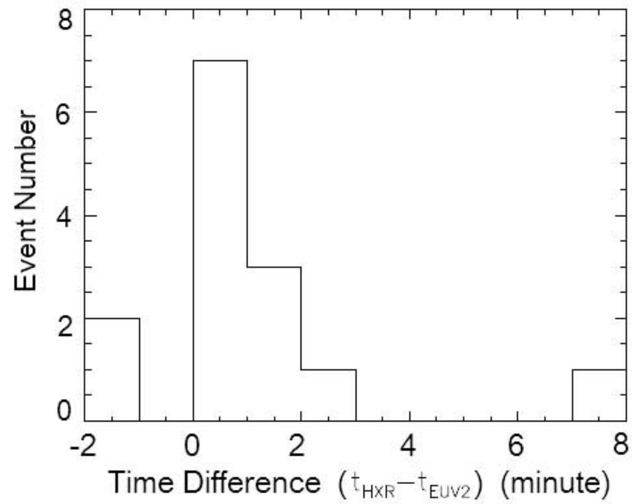

Fig. 5.—Histogram of event number in terms of the time difference between the end of the HXR impulsive phase and the cessation of the change of shear angle in the 14 type I flares with both measured shear angles and corresponding HXR observations. The time bin size is 1 minute.

The histogram of the time difference between the end of the HXR impulsive phase and the cessation of the shear change shows that in most events, the cessation of shear change is 0–2 minutes earlier than the time when the impulsive phase stops (Fig. 5).

This observation indicates that during the impulsive phase magnetic reconnection occurs mainly in the highly sheared region (within the filament channel), but reconnection progresses out to the weakly sheared region (outside the filament channel) during the gradual phase. This result implies that the change from impulsive phase to gradual phase may be related to the magnetic shear change as suggested by Lynch et al. (2004), although the two changes do not happen at exactly the same time. The observation also indicates that the splitting of the sheared envelope of the highly sheared core field happens near the end of the impulsive phase in most cases, since the cessation of shear change may be interpreted as this splitting of the sheared envelope (Paper I).

6. SUMMARY

We have, for the first time, carried out a statistical study of shear motion of the UV/EUV footpoints in a large sample (50) of well-observed X and M class two-ribbon flares, observed by *TRACE* in 1998–2005. These flares are classified into three groups: type I flares, which show shear motion of footpoints and ribbon separation; type II flares, which show ribbon separation but no measurable shear motion of footpoints; and type III flares, which

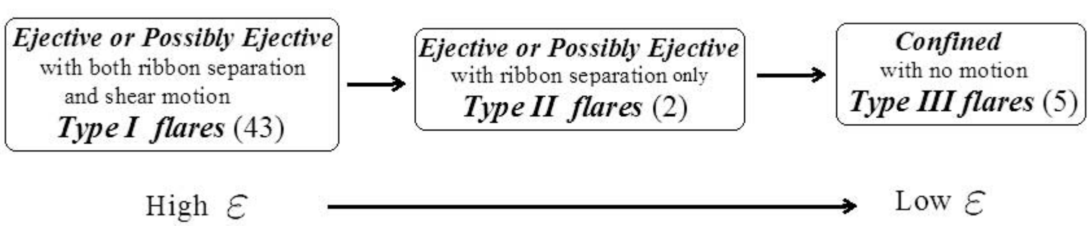

Fig. 4.—Schematic representation of the flare energy scale indicating the type of flare footpoint motions. Here "ε" refers to the relative amount of magnetic free energy in the corona prior to the flare.

show no shear motion of the footpoints or ribbon separation. We also compared our classification with the traditional classification of ejective and confined flares (Svestka 1986). Our results can be summarized as follows:

1. Our study shows that 86% (43 out of 50) of the flares belong to type I, and all type I flares (ejective or possibly ejective) show obvious ribbon separation during the flare. This 86% fraction is much larger than the 45% (14 out of 31) fraction reported by Bogachev et al. (2005). Our observations indicate that both shear motion of conjugate footpoints and ribbon separation are common features in two-ribbon flares. These flares may be interpreted with the well-accepted standard picture of two-ribbon eruptive flares, which is the (whole or partial) eruption of a magnetic flux rope from the sheared core of a closed bipolar magnetic field (Moore et al. 1995 and references therein). A detailed description of this standard model and the interpretation of shear motion of footpoints are given in Paper I.

2. Ejective flares (which have ribbon separation and corresponding CMEs) almost always show shear change of the footpoints (only 1 counterexample out of 37). There are two flares that show ribbon separation but no shear motion. However, shear motion of the footpoints is always accompanied by ribbon separation, which is not consistent with the result reported by Bogachev et al. (2005), who found that 8 out of the 31 flares show mainly shear motion.

3. The initial and final angles of the footpoints in 24 type I flares have been measured, and they are mainly distributed in the range from 50° to 80° and from 15° to 55°, respectively, in most events. This result may indicate that the magnetic field relaxes toward, but does not generally reach, a fully potential state. However, we cannot exclude the possibility that the magnetic field does relax to a fully potential state after the flare for some events, especially those events having final shear angle less than 15°, due to the uncertainties in our measurements of the shear angle. The *change* of shear angle is in the range between 15° and 60°. This measurement of the distributions of the initial and final shear angles may provide some constraints on three-dimensional magnetic reconnection models for solar eruptions.

4. Some flares show no shear change of the conjugate footpoints during the flare. These flares have either no obvious ribbon separation (five type III flares) or very small ribbon separation (two type II flares). Similar to type I flares, type II flares may also be driven by the (whole or partial) eruption of a magnetic flux rope from the sheared core of a closed bipolar magnetic field, but we speculate that these are partial eruptions involving a relatively small amount of axial magnetic flux. The brightenings of type III flares appear at a position far from the magnetic inversion line at the flare onset, and no ribbon separation is observed during the flare. These flares belong to the confined flare category. Our observations in the context of several models for confined flares are discussed in § 4.2.

5. The cessation of shear change is 0–2 minutes earlier than the end of the impulsive phase in 10 out of the 14 events with measured shear angle and corresponding HXR observations. This provides a positive answer to our hypothesis, namely, that the change from impulsive to gradual phase appears to be related to the magnetic shear change.

We acknowledge the referee for his or her valuable suggestions to improve this paper. Y. N. S. sincerely thanks Spiro Antiochos, Ed Deluca, Jun Lin, Mark Weber, Guangli Huang, and Judith Karpen for fruitful discussions and valuable suggestions. The authors wish to thank the teams of *TRACE*, *SOHO* MDI, NJIT BBSO, *Yohkoh*/HXT, and *RHESSI* for providing the valuable data. The authors would like to thank all those who put tremendous efforts into generating these catalogs: the *TRACE* Flare Catalog (footnote 3), kindly provided by the Solar and Stellar X-Ray Group at the Smithsonian Astrophysical Observatory; the *Yohkoh* Flare Catalog (footnote 5), kindly provided by J. Sato et al.; and the *GOES* Flare Catalog (footnote 4), kindly provided by the Space Environment Center, National Oceanic and Atmospheric Administration. The CME Catalog (footnote 6) is generated and maintained at the CDAW Data Center by NASA and the Catholic University of America in cooperation with the Naval Research Laboratory. *SOHO* is a project of international cooperation between ESA and NASA. The *TRACE* analysis was supported at Smithsonian Astrophysics Observatory (SAO) by a contract from Lockheed Martin. Y. N. S. was also supported by an SAO Predoctoral Fellowship, the NSFC projects with 10333030 and 10273025, and "973" program with 2006CB806302.

REFERENCES

Berger, M. A., & Field, G. B. 1984, J. Fluid Mech., 147, 133
Bogachev, S. A., Somov, B. V., Kosugi, T., & Sakao, T. 2005, ApJ, 630, 561
Forbes, T. G. 1992, in Eruptive Solar Flares, ed. Z. Svestka, B. V. Jackson, & M. E. Machado (Berlin: Springer), 79
Gerrard, C. L., & Hood, A. W. 2003, Sol. Phys., 214, 151
Gibson, S. E., & Fan, Y. 2006a, ApJ, 637, L65
———. 2006b, J. Geophys. Res., in press
Handy, B. N., et al. 1999, Sol. Phys., 187, 229
Heyvaerts, J., Priest, E. R., & Rust, D. M. 1977, ApJ, 216, 123
Hirayama, T. 1974, Sol. Phys., 34, 323
Ji, H. S., Huang, G. L., Wang, H. M., Zhou, T. H., Li, Y. P., Zhang, Y. A., & Song, M. T. 2006, ApJ, 636, L173
Kosugi, T., et al. 1991, Sol. Phys., 136, 17
Kurokawa, H. 1989, Space Sci. Rev., 51, 49
Lin, R. P., et al. 2002, Sol. Phys., 210, 3
Lynch, B. J., Antiochos, S. K., MacNeice, P. J., Zurbuchen, T. H., & Fisk, L. A. 2004, ApJ, 617, 589
Machado, M. E., Moore, R. L., Hernandez, A. M., Rovira, M. G., Hagyard, M. J., & Smith, J. B. 1988, ApJ, 326, 425
Manchester, W. 2003, J. Geophys. Res., 108, 1162
Manchester, W., IV, Gombosi, T., DeZeeuw, D., & Fan, Y. 2004, ApJ, 610, 588
Moore, R., et al. 1980, in Solar Flares: A Monograph from Skylab Solar Workshop II, ed. P. Sturrock (Boulder: Colorado Assoc. Univ. Press), 341
Moore, R. L. 1988, ApJ, 324, 1132
Moore, R. L., LaRosa, T. N., & Orwig, L. E. 1995, ApJ, 438, 985
Moore, R. L., Sterling, A. C., Hudson, H. S., & Lemen, J. R. 2001, ApJ, 552, 833
Pallavicini, R., Serio, S., & Vaiana, G. S. 1977, ApJ, 216, 108
Priest, E. R. 1981, Solar Flare Magnetohydrodynamics (New York: Gordon & Breach)
Priest, E. R., & Forbes, T. G. 2002, A&A Rev., 10, 313
Qiu, J., Lee, J., & Gary, D. E. 2004, ApJ, 603, 335
Sakurai, T. 1976, PASJ, 28, 177
Shibata, K., Nozawa, S., & Matsumoto, R. 1992, PASJ, 44, 265
Su, Y. N., Golub, L., Van Ballegooijen, A. A., & Gros, M. 2006, Sol. Phys., 236, 325 (Paper I)
Svestka, Z. 1986, in The Lower Atmosphere of Solar Flares, ed. D. F. Neidig (Tucson: Univ. Arizona Press), 332
Svestka, Z., & Cliver, E. W. 1992, in Eruptive Solar Flares, ed. Z. Svestka, B. V. Jackson, & M. E. Machado (New York: Springer), 1
Tandberg-Hanssen, E., & Emslie, A. G. 1988, The Physics of Solar Flares (Cambridge: Cambridge Univ. Press)
Tang, F. 1985, Sol. Phys., 102, 131
Török, T., & Kliem, B. 2005, ApJ, 630, L97
Zhang, M., & Golub, L. 2003, ApJ, 595, 1251
Zhang, M., Golub, L., Deluca, E., & Burkepile, J. 2002, ApJ, 574, L97
Zhang, M., & Low, B. C. 2005, ARA&A, 43, 103

VOLUME 665

NUMBER 2, PART 1

THE ASTROPHYSICAL JOURNAL

2007 AUGUST 20

(*Continued on inside page*)

PUBLISHED BY THE UNIVERSITY OF CHICAGO PRESS FOR
THE AMERICAN ASTRONOMICAL SOCIETY

ASJOAB 665(2, Pt. 1) 887–1508 (2007)

(*Continued from front cover*)

(*Continued on following page*)

(Continued from preceding page)

THE ASTROPHYSICAL JOURNAL, 665:1448–1459, 2007 August 20

WHAT DETERMINES THE INTENSITY OF SOLAR FLARE/CME EVENTS?

YINGNA SU,[1,2] ADRIAAN VAN BALLEGOOIJEN,[1] JAMES MCCAUGHEY,[1]
EDWARD DELUCA,[1] KATHARINE K. REEVES,[1] AND LEON GOLUB[1]
Received 2007 February 19; accepted 2007 May 8

ABSTRACT

We present a comprehensive statistical study addressing the question of what determines the intensity of a solar flare and associated coronal mass ejection (CME). For a sample of 18 two-ribbon flares associated with CMEs, we have examined the correlations between the *GOES* soft X-ray peak flare flux (PFF), the CME speed ($V_{\rm CME}$) obtained from *SOHO* LASCO observations, and six magnetic parameters of the flaring active region. These six parameters measured from both *TRACE* and *SOHO* MDI observations are: the average background magnetic field strength (B), the area of the region where B is counted (S), the magnetic flux of this region (Φ), the initial shear angle (θ_1, measured at the flare onset), the final shear angle (θ_2, measured at the time when the shear change stops), and the change of shear angle ($\theta_{12} = \theta_1 - \theta_2$) of the footpoints. We have found no correlation between θ_1 and the intensity of flare/CME events, while the other five parameters are either positively or negatively correlated with both $\log_{10}$(PFF) and $V_{\rm CME}$. Among these five parameters, Φ and θ_{12} show the most significant correlations with $\log_{10}$(PFF) and $V_{\rm CME}$. The fact that both $\log_{10}$(PFF) and $V_{\rm CME}$ are highly correlated with θ_{12} rather than with θ_1 indicates that the intensity of flare/CME events may depend on the *released* magnetic free energy rather than the *total* free energy stored prior to the flare. We have also found that a linear combination of a subset of these six parameters shows a much better correlation with the intensity of flare/CME events than each parameter itself, and the combination of $\log_{10}\Phi$, θ_1, and θ_{12} is the top-ranked combination.

Subject headings: Sun: corona — Sun: coronal mass ejections (CMEs) — Sun: flares — Sun: magnetic fields — Sun: photosphere

1. INTRODUCTION

Solar flares, prominence eruptions, and coronal mass ejections (CMEs) are magnetic phenomena thought to be powered by the magnetic free energy (i.e., the difference between the observed total magnetic energy and the potential field magnetic energy) stored in the corona prior to the eruption. Storage of free energy requires a nonpotential magnetic field, and it is therefore associated with a shear or twist in the coronal field away from the potential, current-free state (Priest & Forbes 2002). One indication of such a stressed magnetic field is the presence of a prominence. Another important indicator of a stressed magnetic field is the presence of sigmoid signatures discovered by Rust & Kumar (1996) and Canfield et al. (1999) with *Yohkoh*. Indeed, they have found that active regions that are sigmoidal to be the most likely to erupt. Lin (2004) pointed out that the free energy stored in a stressed magnetic structure prior to the eruption depends on the strength of the background field, so the stronger the background field, the more free energy can be stored, and thus the more energetic the eruptive process. The results obtained by Falconer et al. (2006) agree with the total nonpotentiality (total free energy) of an active region being roughly the product of the overall twist and the flux content of its magnetic field.

A positive correlation between the potential field magnetic energy of the active region and the CME speed has been found by Venkatakrishnan & Ravindra (2003). Guo et al. (2006, 2007) have found a weak correlation between the total magnetic flux of an active region and the CME speed. However, a statistical study of 49 filament eruption-associated CMEs by Chen et al. (2006) showed that the CME speeds are strongly correlated with both the average magnetic field and the total magnetic flux in the filament channel, and the corresponding linear correlation coefficients (LCCs) are 0.7 and 0.68, respectively. Using the catastrophic loss of equilibrium model, Lin (2002, 2004) found that the cases with higher background fields correspond to fast CMEs and lower fields corresponds to slow CMEs. Reeves & Forbes (2005) also found that when the background magnetic field is weak, the radiation emitted by the reconnected X-ray loops beneath a CME (i.e., flare intensity) is faint for an extended version of the Lin & Forbes (2000) model.

Good correlations have been found between different parameters representing the magnetic shear (or twist) or the nonpotentiality of the active region and the flare/CME productivity (Falconer et al. 2006; Jing et al. 2006, and references therein). As mentioned previously, several authors have found a positive correlation between the background magnetic field strength, magnetic flux, or potential magnetic field energy and the CME speed. However, to our knowledge, few studies have been made of the relationship between the magnetic shear or nonpotentiality of the background field and the intensity of flare/CME events (i.e., peak flare flux and CME speed). Our previous study (Su et al. 2007, hereafter Paper I) shows that 86% of the 50 events we examined show a strong-to-weak shear motion of the footpoints during the flare, which indicates that it is a common feature in two-ribbon flares. In Paper I, we have also measured the initial shear angle (θ_1, measured at the flare onset) and final shear angle (θ_2, measured at the time when the shear change stops) of the flare footpoints for 24 events having shear motion of the footpoints and good observations. A detailed interpretation of this shear motion is given by Su et al. (2006), according to a three-dimensional magnetic field configuration having highly sheared inner and less sheared outer magnetic field lines in the preflare

[1] Harvard-Smithsonian Center for Astrophysics, Cambridge, MA 02138.
[2] Purple Mountain Observatory, Nanjing, 210008, China; and Graduate University of Chinese Academy of Sciences, China.

phase (Moore et al. 2001, and references therein). Some detailed studies of both the shear motion and the contracting motion of the footpoints in some individual flares are carried out by Ji et al. (2006, 2007).

Solar flares can be classified as A, B, C, M, or X class according to the soft X-ray peak flux measured by *GOES*, and CME speed can also vary from less than 100 km s^{-1} to several thousand km s^{-1}. An important question is: what determines the magnitude of these quantities? In this paper we address this question by examining how the peak flare flux (PFF, Watt m^{-2}) and CME speed ($V_{\rm CME}$, km s^{-1}) correlates with six magnetic parameters using a subset of two-ribbon flares selected from Paper I. Three of the parameters are measures of the magnetic size: the average background magnetic field strength (B, gauss), the area of the region where B is counted (S, cm^2), and the magnetic flux of this region (Φ, Mx). The other three parameters are measures of the magnetic shear: the initial shear angle (θ_1, degrees), the final shear angle (θ_2, degrees), and the change of shear angle ($\theta_{12} = \theta_1 - \theta_2$, degrees) of the footpoints during the flare. We examine the correlations between the intensity of flare/CME events and each of these six parameters as well as three types of multiparameter combinations. We also study the fraction of the contribution to the total variance of the observed $\log_{10}$(PFF) and $V_{\rm CME}$ from each parameter for these three types of combinations.

This paper is arranged as follows. The data sets and the measurement methods are described in § 2. Our results are presented in § 3, and summary and discussion are given in § 4. The detailed formulae for calculating the coronal magnetic field strength and the multiple linear regress fit are listed in the appendices.

2. DATA SELECTION AND METHODS

In Paper I, we have found that 43 out of the 50 selected two-ribbon flares show both strong-to-weak shear motion of the footpoints and ribbon separation. All of these 43 flares (which are listed in Table 1 in Paper I) have two long and parallel ribbons located on the two opposite magnetic polarities, as can be seen from a combination of the *TRACE* EUV/UV and *SOHO* MDI observations, and an example is shown in Figure 1. In this study, we first select a subset of 31 flares from the 43 flares, to examine the correlations between the $\log_{10}$(PFF), $V_{\rm CME}$, and the background field strength. All of these 31 flares are associated with CMEs and have good corresponding MDI observations. Among these 31 events, 26 events are close to the disk center (longitude $< 45°$), while the other 5 events are close to the solar limb (longitude $> 45°$). The associated CME for each flare is identified based on both temporal (*GOES* flare peak time ± 2 hr) and spatial windows. A detailed description of the criteria can be found in Paper I. From the 31-flare sample we then select 18 flares with measured shear angles of the footpoints to examine the correlations between six magnetic parameters and the intensity of these flare/CME events.

The peak flare flux is derived from the *GOES* soft X-ray classification, which is listed in Table 1 in Paper I. In addition to the peak flare flux, we also considered the *GOES* integrated X-ray flare flux (IFF, J m^{-2}), which is taken from the National Geophysical Data Center.[3] The CME speed is the linear speed taken from the *SOHO* LASCO CME catalog.[4] Since most of our events originated near the solar disk center, they probably involve projection effect for the CME speed. In order to correct the projection effect of the CME speed, we adopt a formula by Leblanc et al. (2001), which assumes radial propagation of CMEs. In this formula, the radial speed ($V_{\rm rad}$) is given by

[3] See http://www.ngdc.noaa.gov/stp/SOLAR/ftpsolarflares.html.
[4] See http://cdaw.gsfc.nasa.gov/CME_list/.

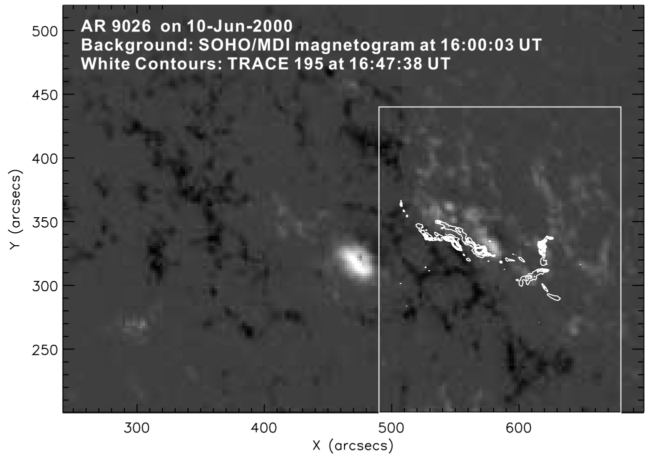

Fig. 1.—*SOHO* MDI image overlaid with *TRACE* contours (*in white*) at 195 Å on 2000 June 10. The white and black spots in MDI image show the positive and negative polarities, respectively. The area enclosed in the white box is the region where the three parameters representing the magnetic size are measured.

$$V_{\rm rad} = V_{\rm sky} \frac{1 + \sin\alpha}{\sin\phi + \sin\alpha}, \qquad (1)$$

in which α is the half angular width of the CME, and ϕ is the angle between the radial passing through the solar origin and the Earth direction given by $\cos\phi = \cos\lambda \cos\psi$, where λ and ψ are heliolatitude and heliolongitude, respectively. Unfortunately, it is very difficult to measure the angular width of halo CME, which is the dominating type of CMEs that we studied and also subject to projection effects. Therefore, we have taken the average angular width value (i.e., $\alpha = 36°$) listed in St. Cyr et al. (2000) for all the 31 events, as suggested by Leblanc et al. (2001). Using the above formula and the coordinate information of all the events, we have estimated their radial speed as the corrected CME speed. The estimated correction factor ranges from 1.09 to 3.8. In this paper, we call the CME speed obtained directly from the catalog $V_{\rm CME}$, and the radial speed after the correction of projection effect $V_{C-{\rm CME}}$, respectively.

2.1. *Measurement Uncertainties of the Shear Angles*

Within our 31-flare sample, the shear angles (θ_1, θ_2, θ_{12}) of 20 flares have been measured and listed in Table 1 in Paper I. The shear angle is defined as the angle between the normal to the magnetic inversion line and the line connecting the conjugate footpoints. The detailed measurement method of these shear angles is illustrated in Figure 1 in Paper I. There are three types of uncertainties in the measurement of the shear angles. First, there are some uncertainties in defining conjugate footpoints, especially for the initial footpoints, which are defined as the first two brightenings that appeared at the flare onset. The difficulty arises because the corresponding postflare loops do not always show up in *TRACE* data for the initial conjugate footpoints. To minimize this uncertainty, we select 18 flares from the 20 flares having measured shear angles, because we do not see the corresponding postflare loops for the initial conjugate footpoints in the other two flares (i.e., flares on 2000 November 24 and 2003 May 31). Second, the inversion line is often difficult to define due to the separation of magnetic polarities and complex shape of the inversion line. Therefore, as described in Paper I, to measure both θ_1 and θ_2 we replaced the real complicated magnetic inversion line with a simplified straight line, which causes some uncertainty in these two angles. However, the change of shear angle θ_{12} is unaffected by such uncertainty. Third, the footpoints always extend over multiple pixels; therefore, for each footpoint we measure an average position with some uncertainty. The uncertainty of the footpoint positions results in an uncertainty of the shear angle, which is listed in Table 1 in Paper I. Despite these uncertainties, the shear angle is a useful proxy for the nonpotential fields involved in these flares.

2.2. *Measurement Methods of the Magnetic Size*

The other three parameters (i.e., B, S, and Φ) are measured from the line of sight *SOHO* MDI magnetograms (at a cadence of 96 minutes) immediately before each flare. To measure these parameters, we first align the *TRACE* EUV/UV images with the corresponding *SOHO* MDI magnetograms. To do the alignment, we first determine the offset between the *TRACE* white light (WL) image and the corresponding MDI magnetogram. We then apply this offset to the *TRACE* EUV/UV images. Figure 1 shows a magnetogram of active region 9062 overlaid with the white contours, which refer to the two flare ribbons observed at 195 Å at 16:47:38 UT on 2000 June 10. By comparison of the MDI magnetogram with the corresponding *TRACE* EUV image, we then select a subarea (the area enclosed in the white box in Fig. 1) of the magnetogram that includes the magnetic elements immediately surrounding the flare ribbons, since these elements are expected to be the dominating magnetic fields that provide energy to the solar flares and CMEs. This selected subarea of the magnetogram is used to measure the three parameters representing the magnetic size.

MDI magnetograms systematically underestimate magnetic field strength and saturate at high magnetic field strength values (Berger & Lites 2003). Following Green et al. (2003) we first multiply the raw MDI data by 1.45 for values below 1200 G and by 1.9 for values above 1200 G to obtain the corrected flux density ($B_{\rm MDI}$). Since most of our events are not located exactly at the solar disk center, the correction for the angle between the magnetic field direction and the observer's line of sight is needed. To do this correction, we assume a purely radial magnetic field and apply the following cosine corrections to each pixel following McAteer et al. (2005):

$$B_{\rm cor} = \frac{B_{\rm MDI}}{\sin[\arccos(d/r)]}, \tag{2}$$

where d is the distance from disk center, and r is the heliocentric radius of the solar disk, which is set to a typical value of 960″. After these corrections, we have applied two methods to measure the background magnetic field strength.

The first method (method 1) is calculating the average photospheric magnetic field strength. In each selected subarea of the magnetogram and for each magnetic polarity, we average the magnetic field strength of all pixels within a contour at 20% of the maximum magnetic field value. We select the 20% contour, because it best defines the areas of the positive and negative polarities most closely associated with the flare for our data sample. For example, if there are sunspots involved, the 20% contour will enclose the sunspots. We refer to the average magnetic field strength for the positive and negative polarities as $B_{\rm pos}$ and $B_{\rm neg}$. B is defined as the average of the absolute value of $B_{\rm pos}$ and $B_{\rm neg}$, i.e., $(|B_{\rm pos}| + |B_{\rm neg}|)/2$. The area ($S = \sum S_i$) and magnetic flux ($\Phi = \sum B_i S_i$) are the sum taken over all the pixels within this 20% contour, and B_i, S_i are the magnetic field strength and the area corresponding to each pixel, respectively. Similar to B_i, the projection effect of S_i is also corrected by applying the cosine corrections. One may argue that this method is highly arbitrary, because it depends heavily on the maximum magnetic field strength value at a single pixel. But we should note that the measurements are also controlled by the distribution of values within the 20% maximum value contour. We also tried a fixed threshold of 200 G, which includes more disconnected and weaker background fields. This method produces worse correlations with the peak flare flux and CME speed than the 20% contour method. Therefore, we will use the 20% contour method in this paper.

The second method (method 2) for measuring the background field is estimating the coronal field strength at a point P above the magnetic inversion line (MIL). The preflare magnetic field in active regions is expected to be strongly sheared, so a potential-field model cannot accurately describe the direction of the coronal field. However, to estimate the field strength, a potential-field model may be adequate. The point P is located at a height h above the photosphere. For all of the events, we set h to be 7250 km (10″), which is a typical value of the half distance between the two flare ribbons at the *GOES* flare peak time for most of the events we studied. The projection of P in the photosphere $\rm P_0$ is on the magnetic inversion line (MIL) involved in the flare/CME events. The formulae we used to estimate the magnetic field strength at P are shown in Appendix A. From these formulae we find that the field strength $B_{\rm cor}$ is heavily dependent on the photospheric field at the points close to the point $\rm P_0$. In order to minimize the random errors, for each event we make 10 measurements of $B_{\rm cor}$, by moving the point $\rm P_0$ along the magnetic inversion line between the two flare ribbons. $B_{\rm cor}$ used below is the average of these 10 values.

3. RESULTS

3.1. *Peak Flare Flux and CME Speed versus Magnetic Field Strength*

The left four panels in Figure 2, from the top to the bottom, show scatter plots of $\log_{10}$(PFF), $\log_{10}$(IFF), $V_{\rm CME}$, and $V_{C-{\rm CME}}$ versus B (method 1) for all of the 31 events, respectively, and the right four panels show how the relationships change when B is replaced with $B_{\rm cor}$ (method 2). The solid lines show the linear fits to the data points, and the LCC of each plot is also presented in each panel.

Figure 2 shows that both B and $B_{\rm cor}$ are positively correlated with the intensity of flare/CME events represented by $\log_{10}$(PFF), $\log_{10}$(IFF), $V_{\rm CME}$, and $V_{C-{\rm CME}}$. The distribution of the points in the lower four panels of Figure 2 are more scattered and the correlations are slightly worse in comparison to the corresponding upper four panels, which may be due to larger observational uncertainties in the CME speed measurements. We also see that B has slightly worse correlations with $\log_{10}$(PFF) and $\log_{10}$(IFF), but slightly better correlations with both $V_{\rm CME}$ and $V_{C-{\rm CME}}$ than $B_{\rm cor}$. But overall, there is no significant difference between these two parameters. Therefore, we choose B to represent the background magnetic field strength in the following detailed studies.

The upper four panels of Figure 2 show that the IFF has better correlations with both B and $B_{\rm cor}$, in comparison to the PFF, but only slightly. Since there is not much difference between the scatter plots corresponding to IFF and PFF, and PFF is more widely used to represent the flare class, we choose PFF to represent the flare intensity in the following detailed study. In

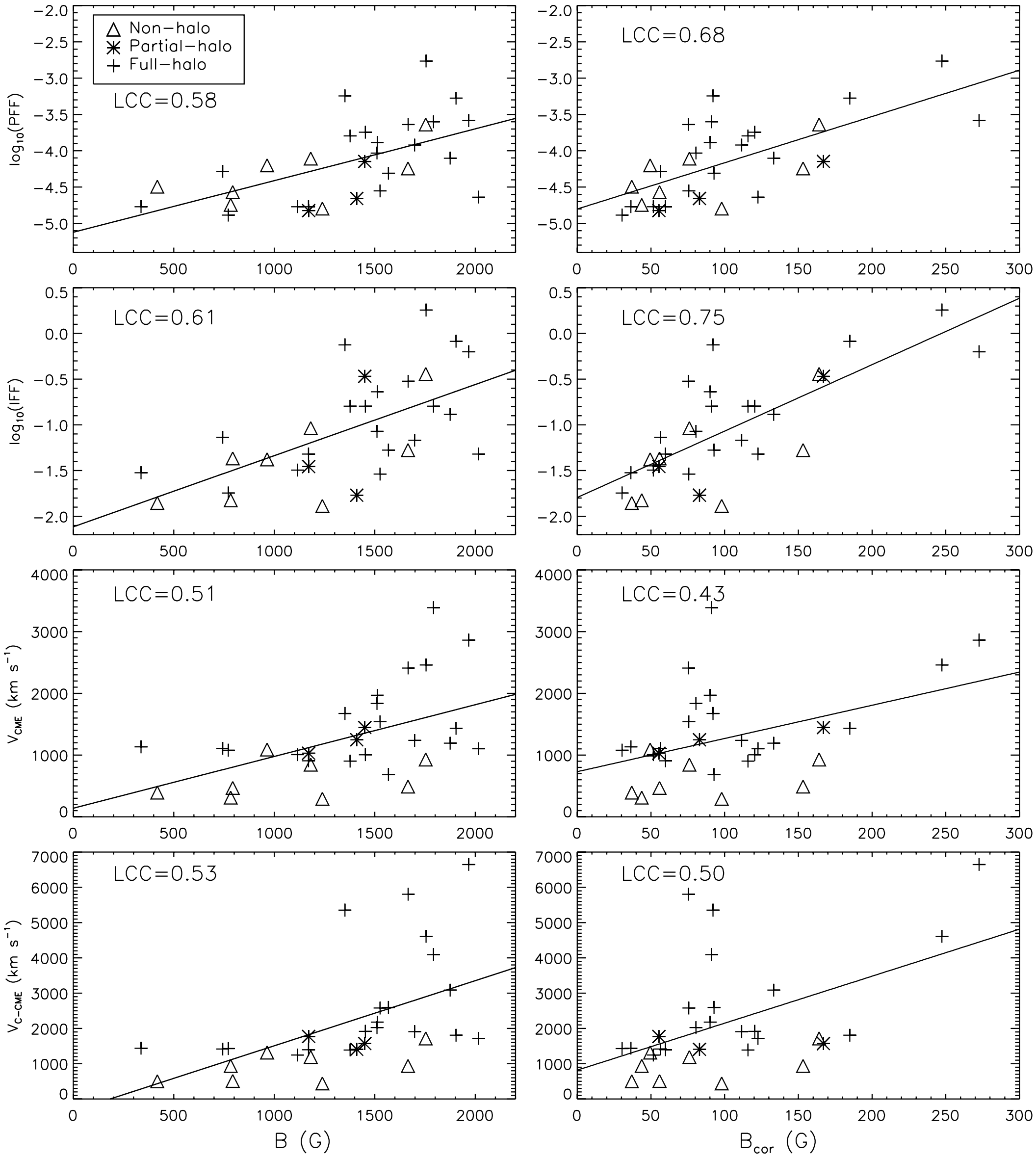

Fig. 2.—Scatter plots of the logarithm of the peak flare flux [$\log_{10}$(PFF), *top row*], the integrated flare flux [$\log_{10}$(IFF), *second row*], the CME speed ($V_{\rm CME}$, *third row*), and the corrected CME speed ($V_{C-\rm CME}$, *bottom row*) vs. the background magnetic field strength for all of the 31 events included in this paper. The magnetic field strengths in the left (B) and right ($B_{\rm cor}$) columns are calculated using methods 1 and 2, respectively. The solid lines in each panel are the linear fits to the data points, and the linear correlation coefficient (LCC) of the data points is presented in each panel. The flares associated with non-halo, partial-halo, and full-halo CMEs are marked using different symbols, i.e., triangles, asterisks, and plus signs, respectively.

comparison to $V_{\rm CME}$, the $V_{C-\rm CME}$ shows slightly better correlations with B and $B_{\rm cor}$ (see lower four panels in Fig. 2), which indicates that the correction of the CME speed has only slightly improved the correlations. Moreover, some overcorrection may exist in this correction method as suggested by Gopalswamy et al. (2001). Therefore, the original CME speed ($V_{\rm CME}$) is used to represent the CME speed in the following detailed analysis.

CMEs are categorized as non-halo, partial-halo, and full-halo CMEs for those having angular width lower than 120°, between 120° and 320°, and greater than 320°, respectively (Lara et al. 2006). The lower four panels of Figure 2 show that most of the non-halo CMEs (*triangles*) have slower speed than the partial-halo (*asterisks*) and full-halo CMEs (*plus signs*), which is consistent with the result reported by Lara et al. (2006), who propose that the observed "halo" is the manifestation (compressed material) of the shock wave driven by fast CMEs. But we do not see an obvious difference between the speeds of partial-halo and full-halo CMEs as reported by Lara et al. (2006), which may be due to our smaller data sample. We also see no obvious differences in the PFF and IFF between the flares associated with these three types of CMEs as shown in the upper four panels of Figure 2.

Figure 3*a* presents the scatter plot of the coronal field strength ($B_{\rm cor}$) versus the CME speed ($V_{\rm CME}$) for the 31 events included in this study. Different symbols represent the events with different ranges of CME mass, and those CMEs with unknown mass are marked with diamonds. The CME mass is taken from the *SOHO* LASCO CME catalog. One should note that there are generally large uncertainties in these numbers, because the estimation of the CME mass involves a number of assumptions (Vourlidas et al. 2000). Figure 3*a* shows that the CMEs with larger mass tend to have faster speed in our sample. If the magnetic forces driving the CME were roughly the same in all cases, we would expect that the CME speed is inversely related to CME mass, contrary to our finding in Figure 3*a*. This indicates

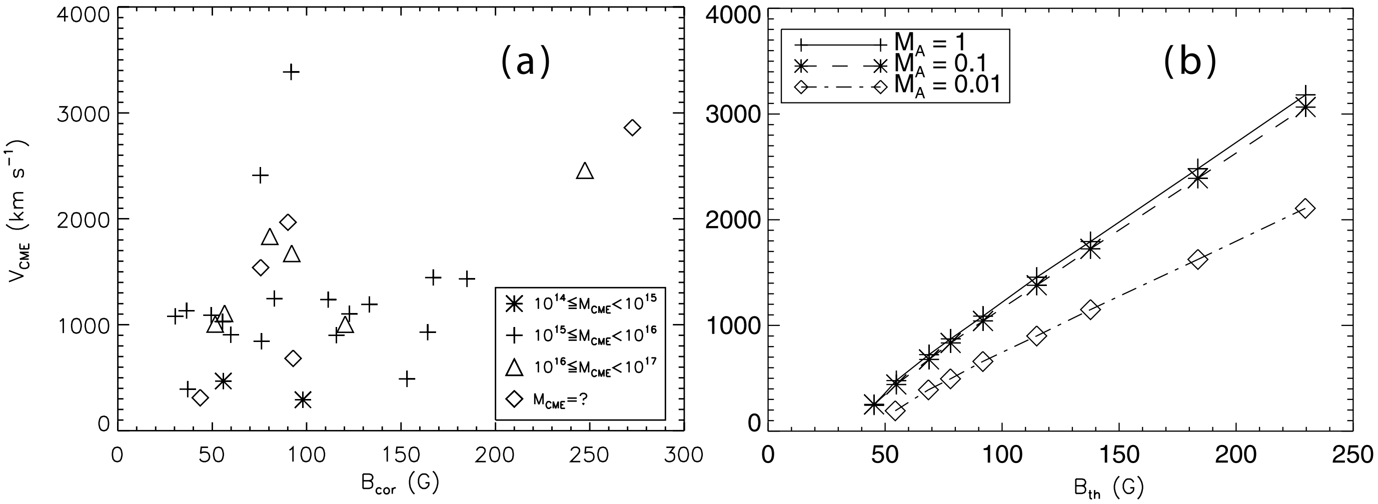

FIG. 3.—(*a*) Scatter plots of the CME speed vs. B_{cor} for all of the 31 events. B_{cor} is the magnetic field strength at a 10″ height above the photosphere, which is calculated from the observations using method 2. The CMEs with different ranges of mass (in units of g) are marked with different symbols, and those CMEs with unknown mass are marked as diamonds. (*b*) Theoretical correlation plots of CME speed and the background magnetic field strength at a 10″ height above the photosphere calculated from a catastrophic loss of equilibrium model (Reeves & Forbes 2005). The different types of lines correspond to different values of Alfvén Mach number M_A.

that the scatter in this plot is not simply due to the different CME mass.

We calculate CME speed as a function of the background field strength at 10″ height above the photosphere (B_{th}), using the extended Lin & Forbes model (2000) by Reeves & Forbes (2005). The result is shown in Figure 3*b*. The plots with different inflow Alfvén Mach number (M_A) are marked with different symbols. In the model, the CME accelerates in the early stages of the event and then asymptotically approaches a constant velocity. This constant velocity is reported in the plot and refers to a height of about three solar radii, which is similar to that of the LASCO observations. The model predicts that the CME speed increases with the background field strength, and for events with the same background field strength, the CME speed also increases with the Mach number (i.e., reconnection rate), but saturates for $M_A \geq 0.1$. This saturation occurs because the force on the flux rope due to the current sheet becomes small when $M_A \geq 0.1$ is large (see Reeves 2006). Consistent with the theoretical model, our observations show that the events with stronger background fields tend to have faster CME speeds. A comparison of Figures 3*a* and 3*b* suggests that much of the scatter in the plot of Figure 3*a* may be caused by different reconnection rates. However, there may be other contributions to the scatter in Figure 3*a*, such as the measurement uncertainties for the CME speed.

3.2. *Peak Flare Flux and CME Speed versus Six Magnetic Parameters*

In § 3.1, we examined the relationship between the intensity of the 31 flare/CME events and the background field strength. In this section, we carry out a further detailed study for a subset of 18 events with measured shear angles of the footpoints. The magnetic parameters in these 18 events we considered can be classified into two categories: parameters representing the magnetic size ($\log_{10}B$, $\log_{10}S$, and $\log_{10}\Phi$), and parameters representing the magnetic shear (θ_1, θ_2, and θ_{12}).

At first, we examine the correlations between each parameter. To do this study, we first check the correlations between the parameters in the same category. The correlation plots between each pair of parameters representing magnetic size are shown in Figures 4*a*–4*c*. We find that both $\log_{10}B$ and $\log_{10}S$ are positively correlated with $\log_{10}\Phi$. This is not surprising, because Φ is the product of B and S. We also find a weak anticorrelation between $\log_{10}B$ and $\log_{10}S$. For the other category with parameters representing magnetic shear, we find that θ_2 is highly correlated with both θ_1 and θ_{12}, as shown in Figures 4*d*–4*e*. But we find no correlation between θ_1 and θ_{12}. This result indicates that θ_2 is not an independent parameter. We then check the correlations between the parameters in different categories. We find a weak correlation between $\log_{10}B$ and θ_{12} (LCC = 0.48), while all of the other parameters in different categories are not correlated with each other (LCC $\leq$ 0.3). Figure 4*f* shows the correlation plot of θ_1 versus θ_{12}/θ_1, so it is not surprising to see a weak correlation in this plot. Figure 4*f* also shows that for the same initial shear angle, the change of shear angle can vary in a very large range in different events ($0.24 \leq \theta_{12}/\theta_1 \leq 0.96$).

For these 18 events, the correlation plots of the three parameters representing magnetic size versus $\log_{10}$(PFF) and V_{CME} are shown in the top and bottom panels of Figure 5, respectively. These parameters are $\log_{10}B$ (*left panels*), $\log_{10}S$ (*middle panels*), and $\log_{10}\Phi$ (*right panels*). Each of these three parameters is positively correlated with both $\log_{10}$(PFF) and V_{CME}. Of these parameters, $\log_{10}S$ shows relatively weak correlation with the intensity of flare/CME events, and the corresponding LCCs are 0.34. The correlation between $\log_{10}B$ and the intensity of flare/CME events appears to be slightly better but still weak (LCC*s* = 0.43, 0.38). Among these three parameters, $\log_{10}\Phi$ is the parameter that shows the best correlations with both $\log_{10}$(PFF) (LCC = 0.72) and V_{CME} (LCC = 0.62).

Similar to Figure 5, the top and bottom panels in Figure 6 show the correlation plots of the three parameters representing magnetic shear versus $\log_{10}$(PFF) and V_{CME}. These parameters are θ_1 (*left panels*), θ_2 (*middle panels*), and θ_{12} (*right panels*). θ_1 is correlated neither with $\log_{10}$(PFF) nor with V_{CME}, while θ_2 is negatively correlated with the intensity of flare/CME events (LCCs = −0.42, −0.49). θ_{12} shows good positive correlations with both $\log_{10}$(PFF) (LCC = 0.65) and V_{CME} (LCC = 0.59).

To summarize, five of these six parameters except the initial shear angle (θ_1) show either positive or negative correlations with both $\log_{10}$(PFF) and V_{CME}. Among these five parameters, the total magnetic flux of the region where the magnetic field is counted ($\log_{10}\Phi$) and the change of shear angle (θ_{12}) of the

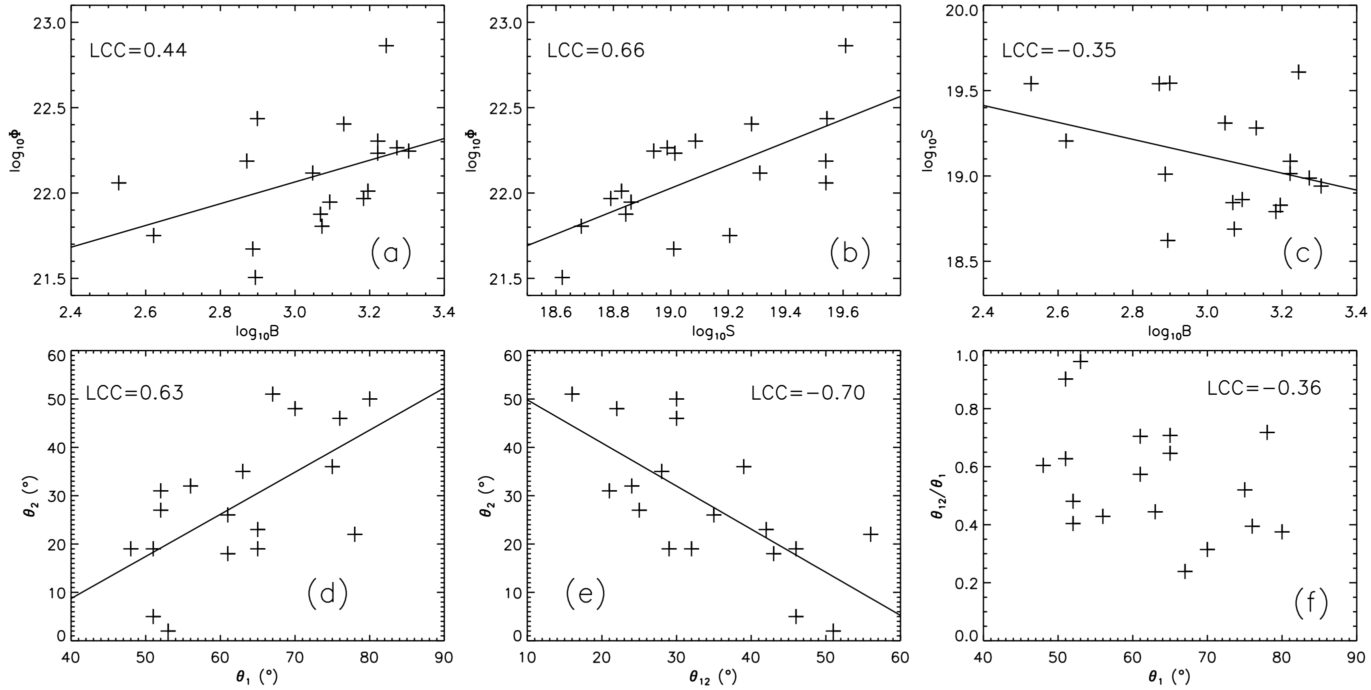

FIG. 4.—Scatter plots of six pairs of magnetic parameters measured from the 18 events with measured shear angles. (*a*) $\log_{10}B$ vs. $\log_{10}\Phi$, (*b*) $\log_{10}S$ vs. $\log_{10}\Phi$, (*c*) $\log_{10}B$ vs. $\log_{10}S$, (*d*) θ_1 vs. θ_2, (*e*) θ_{12} vs. θ_2, and (*f*) θ_1 vs. θ_{12}/θ_1. The solid lines in the figure refer to the linear fits to the data points.

footpoints during the flare are the two parameters that show the strongest correlations with the intensity of flare/CME events.

3.3. *Peak Flare Flux and CME Speed versus Multiparameter Combinations*

In § 3.2 we have found that $\log_{10}\Phi$ and θ_{12} are the two parameters that show the best correlations with the intensity of the 18 flare/CME events. One of the alternative interpretations is that Φ is a combination of B and S, while θ_{12} is a combination of θ_1 and θ_2. In the other words, only four (i.e., $\log_{10}B$, $\log_{10}S$, θ_1, and θ_2) of our six parameters are single parameter measured from observations. This result indicates that a combination of two parameters shows much better correlation with the intensity of the flare/CME events than the individual parameter. Therefore, we consider three multiparameter combinations in this section. In order to study the correlations between each of these three

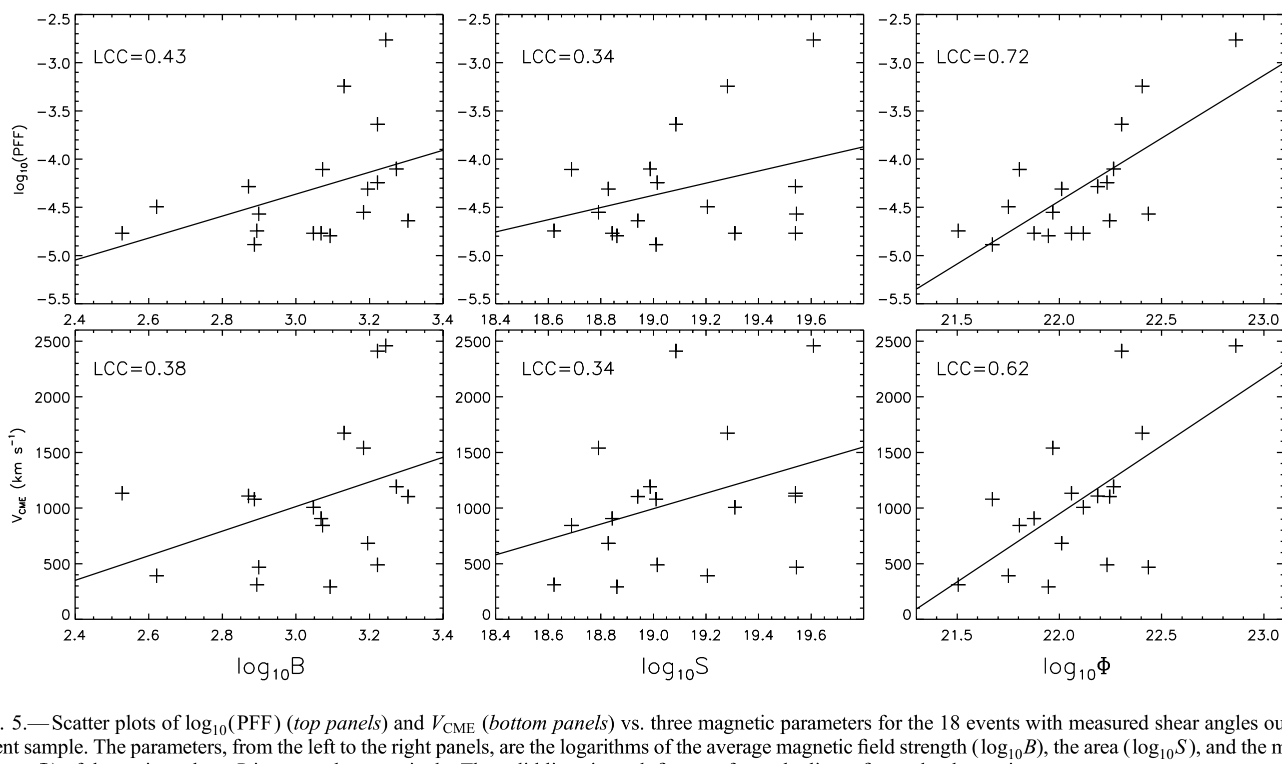

FIG. 5.—Scatter plots of $\log_{10}(\mathrm{PFF})$ (*top panels*) and V_{CME} (*bottom panels*) vs. three magnetic parameters for the 18 events with measured shear angles out of our 31-event sample. The parameters, from the left to the right panels, are the logarithms of the average magnetic field strength ($\log_{10}B$), the area ($\log_{10}S$), and the magnetic flux ($\log_{10}\Phi$) of the region where B is counted, respectively. The solid lines in each figure refer to the linear fits to the data points.

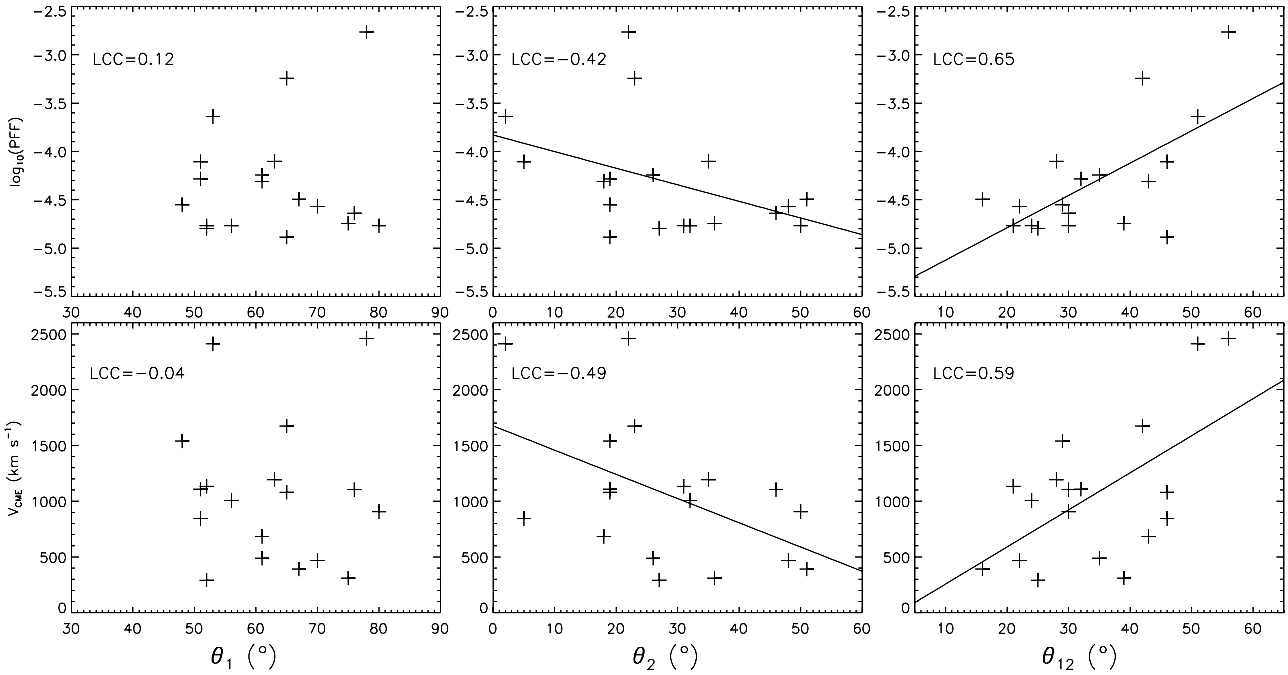

FIG. 6.— Similar to Fig. 5, but scatter plots of $\log_{10}$(PFF) (*top panels*) and $V_{\rm CME}$ (*bottom panels*) vs. the other three parameters for the 18 events with measured shear angle. These parameters are the initial shear angle (θ_1, *left panels*), the final shear angle (θ_2, *middle panels*), and the change of shear angle (θ_{12}, *right panels*) of the footpoints, respectively.

combinations and the intensity of the flare/CME events, we have done multiple linear regression fits to the observed $\log_{10}$(PFF) and $V_{\rm CME}$ for each combination, using the "regress" function in IDL. Appendix B shows the expression for the fitting function ($Y_{\rm fit}$), which is a linear combination of all the parameters in each combination.

At first, we create a combination of four parameters (combination 1), i.e., $\log_{10}B$, $\log_{10}S$, θ_1, and θ_{12}. The first three parameters in this combination are three single parameters measured from the observations. We choose θ_{12} instead of the other single parameter θ_2 in this combination, because θ_2 appears not to be an independent parameter as shown in § 3.2. The detailed information of the fitting functions for combination 1 is listed in the left three columns of Table 1. The first column lists all the parameters in combination 1, and the constant and coefficients (as well as 1 σ uncertainty) of each parameter in the fitting functions corresponding to $\log_{10}$(PFF) and $V_{\rm CME}$ are shown in the second and the third columns, respectively.

From the left three columns of Table 1 we can see that the coefficients of $\log_{10}B$ and $\log_{10}S$ are equal within the errors of the linear regression fit, and we also note that these two parameters may not be independent from each other (see Fig. 4*c*). Therefore, we replace $\log_{10}B$ and $\log_{10}S$ in combination 1 with a combination of them ($\log_{10}\Phi$) to create combination 2 (i.e., $\log_{10}\Phi$, θ_1, and θ_{12}). The detailed information of the fitting functions for combination 2 is listed in the middle three columns of Table 1, from which we see that the coefficient of $\log_{10}\Phi$ has smaller 1 σ uncertainty than the coefficients of both $\log_{10}B$ and $\log_{10}S$. The left panels in Figure 7, from the top to the bottom, show the scatter plots of $Y_{\rm obs}$ [the observed $\log_{10}$(PFF) and $V_{\rm CME}$] versus $Y_{\rm fit}$ [the fitted $\log_{10}$(PFF) and $V_{\rm CME}$] for combination 1; the plot for $\log_{10}$(PFF) is shown in the upper left panel, and the plot for $V_{\rm CME}$ is shown in the lower left panel. Similar to the left panels, the middle panels in Figure 7 show the scatter plots for combinations 2. A comparison of the left and middle panels of Figure 7 shows that combination 2 has better correlation between the observed and fitted $\log_{10}$(PFF) (LCC $= 0.87$) than combination 1 (LCC $= 0.83$). Although combination 2 has slightly worse correlation for $V_{\rm CME}$ (LCC $= 0.79$) than combination 1 (LCC $= 0.78$), overall, combination 2 appears to be better than combination 1.

The left and middle three columns of Table 1 shows that the coefficient of θ_1 are very small, and the 1 σ uncertainty in this coefficient is greater than its value. This indicates that this parameter does not play an important role in the fitting functions corresponding to both combinations 1 and 2. Therefore, we

TABLE 1

CONSTANTS, COEFFICIENTS, AS WELL AS THEIR 1 σ UNCERTAINTIES OF THE MULTIPLE LINEAR REGRESSION FITS FOR THREE TYPES OF MULTIPARAMETER COMBINATIONS

	COEFFICIENTS			COEFFICIENTS			COEFFICIENTS	
PARAMETER	$\log_{10}$(PFF)	$V_{\rm CME}$	PARAMETER	$\log_{10}$(PFF)	$V_{\rm CME}$	PARAMETER	$\log_{10}$(PFF)	$V_{\rm CME}$
$\log_{10}B$	0.93 ± 0.49	(0.97 ± 0.60)E3	...	...	...	...	...	...
...	...	...	$\log_{10}\Phi$	1.10 ± 0.24	(1.04 ± 0.34)E3	$\log_{10}\Phi$	1.10 ± 0.23	(1.01 ± 0.34)E3
$\log_{10}S$	1.00 ± 0.30	(1.08 ± 0.37)E3	...	...	...	...	...	...
θ_1	(0.03 ± 0.87)E−2	(−0.09 ± 0.11)E2	θ_1	(−0.13 ± 0.74)E−2	(−0.10 ± 0.10)E2	...	...	...
θ_{12}..............	(2.86 ± 0.90)E−2	(0.29 ± 0.11)E2	θ_{12}..............	(2.63 ± 0.69)E−2	(0.27 ± 0.10)E2	θ_{12}..............	(2.62 ± 0.67)E−2	(0.27 ± 0.10)E2
Constant	−2.73E1	−2.30E4	Constant	−2.93E1	−2.23E4	Constant	−2.93E1	−2.21E4

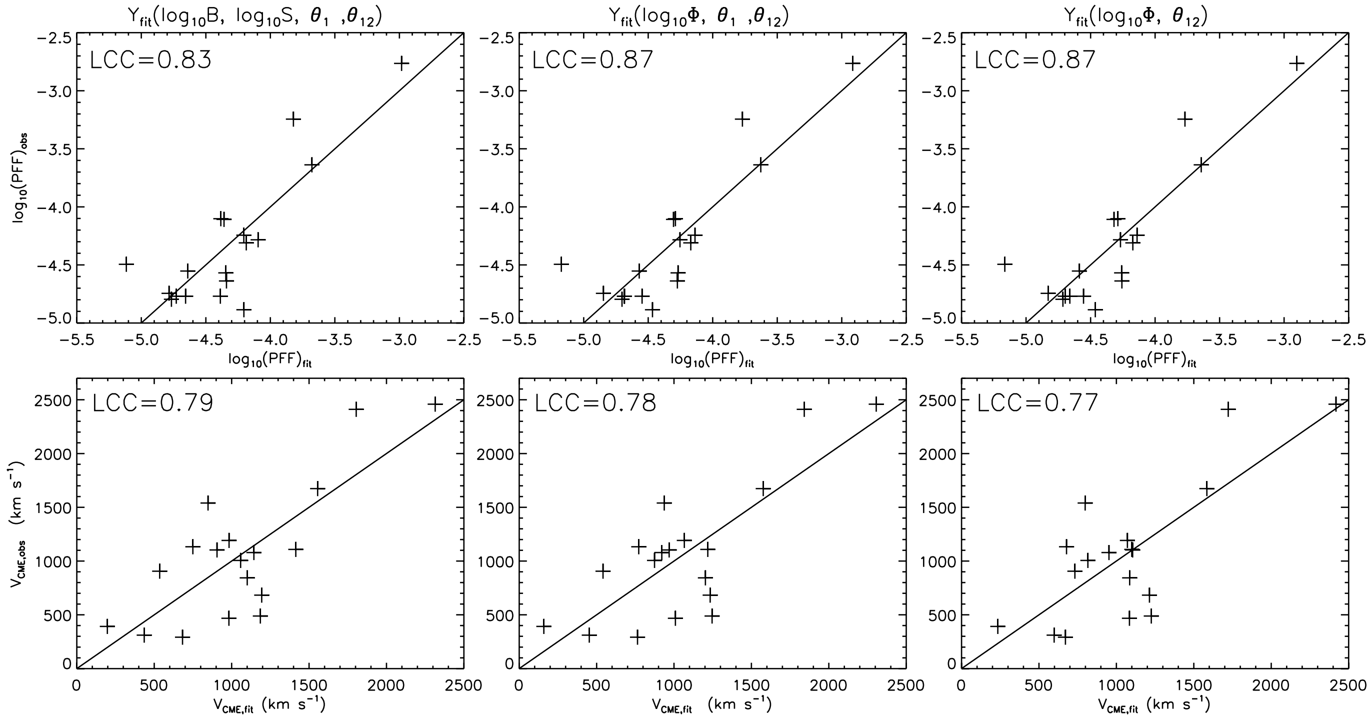

Fig. 7.—Scatter plots of the observed log 10(PFF) (*top panels*) and $V_{\rm CME}$ (*bottom panels*) vs. the fitted log 10(PFF) and $V_{\rm CME}$ ($Y_{\rm fit}$) corresponding to three types of multiparameter combinations for the 18 events with measured shear angles. *Left*: Combination 1 ($\log_{10}B$, $\log_{10}S$, θ_1, θ_{12}); *middle*: combination 2 ($\log_{10}\Phi$, θ_1, and θ_{12}); *right*: combination 3 ($\log_{10}\Phi$ and θ_{12}). The solid lines in each figure refer to the linear fits to the data points.

create combination 3 (i.e., $\log_{10}\Phi$, θ_{12}) by removing the parameter θ_1 from combination 2. The detailed information of the fitting functions for combination 3 is listed in the right three columns of Table 1. The right panels of Figure 7 show the scatter plots for combination 3, and the LCCs in these plots are only slightly worse than those in the corresponding middle panels. This further confirms that θ_1 plays only a minor role in combination 2. This result is also consistent with the fact that the coefficients and 1 σ uncertainties for $\log_{10}\Phi$ and θ_{12} in combinations 2 and 3 are very similar to each other (see Table 1).

The top panels of Figure 7 show strong and linear correlation between the observed and fitted values of $\log_{10}(\mathrm{PFF})$ for each parameter combination, with LCCs equal or larger than 0.83. This implies that the observed magnetic parameters that we measured play an important role in determining the peak flare flux. The bottom three panels also show strong linear correlations between $V_{\rm CME}$ and the parameter combinations, but worse ($0.77 \leq \mathrm{LCC} \leq 0.79$), and the distributions of the plots are more scattered than the corresponding top panels. Consistent with the earlier result found in Figure 2, this result may be caused by the larger measurement uncertainties in the CME speed as compared to the peak flare flux.

In this subsection, we have mainly addressed the question of how well the fitting function reproduces the observed intensity of flare/CME events. Now we study the contributions of the various magnetic parameters to the total variances of both $\log_{10}(\mathrm{PFF})$ and $V_{\rm CME}$. Table 2 shows the fraction (σ_i^2) of each parameter's contribution to the total variances ($\sigma_{\rm tot}^2$) of $\log_{10}(\mathrm{PFF})$ and $V_{\rm CME}$ for the three combinations. The calculation methods of σ_i^2 and $\sigma_{\rm tot}^2$ are presented in Appendix B. For combination 1, the largest fractional contribution to the total variances comes from $\log_{10}S$, and the second largest contribution comes from θ_{12}. The contribution from $\log_{10}B$ is slightly less than θ_{12}, while θ_1 shows significantly less contribution than the other three parameters. For both combinations 2 and 3, $\log_{10}\Phi$ is the top-ranked parameter, which shows the strongest contribution to the total variance of the intensity of flare/CME events, while θ_{12} is the second-ranked parameter. Similar to combination 1, θ_1 in combination 2 again has a very small contribution to the total variances of $\log_{10}(\mathrm{PFF})$ and $V_{\rm CME}$. The fraction ($\sigma_o^2/\sigma_{\rm tot}^2$) of the

TABLE 2

The Contributions from each Parameter in Three Types of Multiparameter Combinations (σ_i^2) and Other Unknown Sources (σ_o^2) to the Total Variances of the Observed $\log_{10}(\mathrm{PFF})$ ($\sigma_{\rm tot}^2 = 0.29$, PFF is in units of W m^{-2}) and $V_{\rm CME}$ ($\sigma_{\rm tot}^2 = 3.45\times10^5$ km^2 s^{-2})

Parameter	$(\sigma_{i/o}^2/\sigma_{\rm tot}^2)100\%$ log$_{10}$(PFF)	$(\sigma_{i/o}^2/\sigma_{\rm tot}^2)100\%$ $V_{\rm CME}$	Parameter	$(\sigma_{i/o}^2/\sigma_{\rm tot}^2)100\%$ log$_{10}$(PFF)	$(\sigma_{i/o}^2/\sigma_{\rm tot}^2)100\%$ $V_{\rm CME}$	Parameter	$(\sigma_{i/o}^2/\sigma_{\rm tot}^2)100\%$ log$_{10}$(PFF)	$(\sigma_{i/o}^2/\sigma_{\rm tot}^2)100\%$ $V_{\rm CME}$
$\log_{10}B$	12.5%	11.2%	...	...	...	...	...	...
...	...	...	$\log_{10}\Phi$	36.7%	27.6%	$\log_{10}\Phi$	36.4%	25.7%
$\log_{10}S$	29.3%	28.3%	...	...	...	...	...	...
θ_1	0.0%	2.1%	θ_1	0.1%	2.7%	...	...	...
θ_{12}	30.7%	26.8%	θ_{12}	26.0%	23.4%	θ_{12}	25.8%	21.9%
Others	30.3%	38.1%	Others	23.5%	38.6%	Others	23.6%	41.3%

total variances due to unknown sources and/or measurement errors is also calculated and listed in Table 2 (see Appendix B for a detailed description of the method). The sum of all the fractions in each column is not 100% because of some approximations that have been made in calculating these fractions (Appendix B). For a large enough data sample, and when there is no correlation at all between magnetic parameters, this sum should be 100%. We find that the observed magnetic parameters account for a large fraction of the observed total variance; less than one-third of the variance of $\log_{10}$(PFF) is due to unknown sources or measurement errors. The total variances of $\log_{10}$(PFF) and $V_{\rm CME}$ are 0.29 (PFF is in units of W $\rm m^{-2}$) and $3.45 \times 10^5\ \rm km^2\ s^{-2}$, respectively.

4. SUMMARY AND DISCUSSION

For a sample of 31 two-ribbon flares associated with CMEs, we have measured the magnetic field strength (from *SOHO* MDI magnetograms) of the magnetic polarities involved in the flares using two methods: the average photospheric magnetic field strength (B) within a contour of 20% of the maximum field strength, and the magnetic field strength at a single point located at 10″ height above the photosphere ($B_{\rm cor}$). We have found that both measures show that for events with larger magnetic field strength, the corresponding peak flare flux tends to be larger and the corresponding CME speed tends to be faster. This result is consistent with previous theoretical studies by Lin (2002, 2004) and Reeves & Forbes (2005), who found that the cases with higher background fields correspond to fast CMEs and strong flares, whereas lower fields correspond to slow CMEs and weak flares. This result is found through some calculations under the framework of a catastrophic loss of equilibrium model. Similar results have also been found by Chen et al. (2006) for a sample of CMEs associated solely with filament eruptions.

We have selected 18 events with measured shear angles out of the 31-event sample for further detailed study. For these 18 events, we have measured six parameters using both *SOHO* MDI magnetograms and corresponding *TRACE* observations of the flare footpoints. Three of these six parameters are measures of the magnetic size, and they are the average photospheric magnetic field strength (B), the area of the region where B is counted (S), and the magnetic flux of this region (Φ). The other three parameters represent the magnetic shear as determined from flare observations. These are the initial shear angle (θ_1, measured at the flare onset), the final shear angle (θ_2, measured at the time when the shear change stops), and the change of shear angle ($\theta_{12} = \theta_1 - \theta_2$) of the footpoints. With our six measures, we address the question what determines the intensity of the flare/CME events by examining three sets of correlations: (1) the correlations of the parameters with each other; (2) the correlations of the logarithm of the peak flare flux [$\log_{10}$(PFF)] as well as CME speed ($V_{\rm CME}$) versus each of the six parameters; (3) the correlations of the observed $\log_{10}$(PFF) and $V_{\rm CME}$ versus three types of multiparameter combinations, which are $\log_{10}B$, $\log_{10}S$, θ_1, and θ_{12} (combination 1); $\log_{10}\Phi$, θ_1, and θ_{12} (combination 2); and $\log_{10}\Phi$ and θ_{12} (combination 3).

The logarithms of all three parameters representing magnetic size show positive correlations with both $\log_{10}$(PFF) and $V_{\rm CME}$. More specifically, $\log_{10}\Phi$ shows much better correlations (LCCs = 0.72, 0.62) with both $\log_{10}$(PFF) and $V_{\rm CME}$ than the other two parameters (LCCs $\leq$ 0.43), i.e., $\log_{10}B$ and $\log_{10}S$, probably because the magnetic flux Φ is the product of the other two parameters. This result differs from the result reported by Chen et al. (2006), who found that the average field strength is better correlated with CME speed than the magnetic flux in the filament channel for the CMEs associated with filament eruptions.

We have, for the first time, found that there are no correlations between θ_1 and $\log_{10}$(PFF) as well as $V_{\rm CME}$, while θ_{12} shows a strong positive correlation with the intensity of flare/CME events. The initial shear angle (θ_1) of the footpoints measured at the flare onset may represent the preflare magnetic free energy to some extent, according to our cartoon in Figure 11 in Su et al. (2006), while the change of shear angle (i.e., $\theta_{12} = \theta_1 - \theta_2$) may serve as a proxy of the released magnetic free energy during the flare, but one should keep in mind that the shear angle is not the only parameter that determines the magnetic free energy. Therefore, our result indicate that the intensity of flare/CME events may depend on the *released* magnetic free energy rather than the *total* magnetic free energy stored prior to the flare. This may make it very difficult to predict the magnitude of the flare/CME events. Emslie et al. (2004) suggested that not all of the "free" energy may be available on short timescales to power flares and CMEs, owing to the constraints imposed by helicity conservation. An alternative interpretation of the lack of correlation with θ_1 is that this result is due to the large uncertainties in our measurements of the shear angles, which are fully discussed in § 2.1. More specifically, the uncertainty in the definition of magnetic inversion line may cause large uncertainties in measuring both θ_1 and θ_2, while the change of shear angle is unaffected by such uncertainty. The fact that for the same initial shear angle (θ_1), the change of shear angle (θ_{12}) can vary greatly in different events (Fig. 4*f*) may indicate that the released free magnetic energy could be different in the active regions with the same stored total free energy prior to the eruptions.

For each of the three types of multiparameter combinations we have done multiple linear regression fits to the observed $\log_{10}$(PFF) and $V_{\rm CME}$. For each combination the corresponding fitting functions are a linear combination of all the parameters in this combination. We have also calculated the fraction of each parameter's contribution to the total variances of $\log_{10}$(PFF) and $V_{\rm CME}$. For all of the three combinations, we see strong linear correlations between the observed and fitted values of $\log_{10}$(PFF) and $V_{\rm CME}$. This implies that the observed magnetic parameters play an important role in determining the intensity of the flare/CME events. Furthermore, all three combinations show better correlation with the intensity of flare/CME events than any individual magnetic parameter. Among these three combinations, combination 2 ($\log_{10}\Phi$, θ_1, and θ_{12}) shows the strongest linear correlation between the observed and fitted values of both $\log_{10}$(PFF) and $V_{\rm CME}$. This result indicates that it is very useful to combine B and S into a single magnetic parameter, the flux Φ. Combination 3 ($\log_{10}\Phi$ and θ_{12}) shows only slightly worse correlation with the intensity of flare/CME events than combination 2. Moreover, in combination 2, the fractions of the contribution to the total variances of $\log_{10}$(PFF) and $V_{\rm CME}$ from both $\log_{10}\Phi$ (36.7% and 27.6%) and θ_{12} (26.0% and 23.4%) are significantly greater than θ_1 (0.1% and 2.7%). These results imply that the initial shear angle θ_1 only plays a minor role in determining the peak flare flux and CME speed, which is consistent with the result reported in the last paragraph. These results also suggest that the magnetic flux of the region, where the magnetic field is counted (Φ), and the change of shear angle of the footpoints during the flare (θ_{12}) are two separate but comparably important parameters in determining the intensity of flare/CME events. In other words, large released free energy (a combination of Φ and θ_{12}) tends to produce large flares and fast CMEs.

Although the fitting functions corresponding to the three multiparameter combinations show very strong and linear correlations with the intensity of flare/CME events, we still can see some scatter in these plots (Fig. 7). Some of this scatter may result from different reconnection rates, different durations of reconnection and CME acceleration, different configurations of the ambient magnetic field, and measurement uncertainties. First of all, as shown in Figure 3*b* different reconnection rates may cause the scatter of CME speed, if the background field strength is fixed. Accordingly, different reconnection rates may also cause the scatter of the peak flare flux, if the other parameters are fixed. This is because the fraction of the released energy that is converted into flare or CME energy depends on the reconnection rate as reported by Reeves & Forbes (2005), who also found that greater than 50% of the released energy becomes flare energy when $M_A < 0.006$. Secondly, although many events with larger CME speed and greater peak flare flux tend to originate from strong magnetic field regions, the weak magnetic fields could also produce large CME speed if the durations of reconnection and acceleration are very long as illustrated in Qiu & Yurchyshyn (2005). Thirdly, Liu (2007) found that CMEs under heliospheric current sheet are significantly slower than CMEs under unidirectional open field structures. This implies that the ambient magnetic field structure plays a role in determining the speed of halo CMEs. Therefore, different ambient magnetic structure may make some contributions to the scatter of the plots in the bottom panels of Figure 7. Finally, many uncertainties existed in our measurements of the six parameters and the measurements of CME speed. This may also add some contributions to the scatter of the plots in Figure 7.

In summary, the magnetic flux (Φ) and the change of shear angle (θ_{12}) of the footpoints during the flare show the most significant correlations with the intensity of flare/CME events [$\log_{10}(\mathrm{PFF})$, V_{CME}]. The fact that both $\log_{10}(\mathrm{PFF})$ and V_{CME} are highly correlated with the change of shear angle (θ_{12}) rather than with the initial shear angle (θ_1) indicates that the intensity of flare/CME events may depend on the *released* magnetic free energy rather than the *total* free energy stored prior to the flare. We also found that a linear combination of a subset of our six parameters shows a much better correlation with the intensity of flare/CME events than each parameter itself, and the combination of $\log_{10}\Phi$, θ_1, and θ_{12} is the top-ranked combination. Moreover, in this combination, the fractions of the contribution to the total variances of $\log_{10}(\mathrm{PFF})$ and V_{CME} from both $\log_{10}\Phi$ and θ_{12} are significantly greater than θ_1.

We sincerely thank the anonymous referee for constructive suggestions which have been very useful in improving this paper. Y. N. Su is grateful to Jun Lin, Steven Saar, Guangli Huang, and Monica Bobra for helpful discussions and suggestions. The authors wish to thank the teams of *TRACE*, *SOHO* MDI, and *SOHO* LASCO for providing the valuable data. The CME Catalog (see footnote 4) is generated and maintained at the CDAW Data Center by NASA and The Catholic University of America in cooperation with the Naval Research Laboratory. *SOHO* is a project of international cooperation between ESA and NASA. The *TRACE* analysis was supported at Smithsonian Astrophysics Observatory (SAO) by a contract from Lockheed Martin. Y. N. Su was supported by an SAO Predoctoral Fellowship, the NSFC projects with grants 10333030 and 10273025, and "973" program with grant 2006CB806302.

APPENDIX A

ESTIMATE OF THE CORONAL MAGNETIC FIELD STRENGTH

To estimate the coronal magnetic field strength in the flaring active region, we use a simple potential-field model. Let P be a point at height h above the magnetic inversion line and let P_0 be the projection of P on the photosphere. We use a Cartesian coordinate system (x, y, z) with the origin at P_0; x and y are the horizontal coordinates along and perpendicular to the magnetic inversion line, respectively, and z is the height above the photosphere. The point P is located at $r = (0, 0, h)$, and the potential field $B_{\mathrm{cor}}(r)$ at this point can be estimated using the formula

$$B_{\mathrm{cor}}(r) = \int\int \frac{B_0(x_0, y_0)(r - r_0)}{2\pi|r - r_0|^3}\, dx_0\, dy_0, \tag{A1}$$

where $B_0(x_0, y_0)$ is the photospheric radial field strength at point $r = (x_0, y_0, 0)$ in the selected subarea of the magnetogram. Equation (A1) can be written as

$$\begin{aligned} B_{\mathrm{cor},x} &= -\sum_{ij} \frac{B_{0,ij} x_{0,i}}{2\pi(x_{0,i}^2 + y_{0,j}^2 + h^2)^{3/2}}, \\ B_{\mathrm{cor},y} &= -\sum_{ij} \frac{B_{0,ij} y_{0,j}}{2\pi(x_{0,i}^2 + y_{0,j}^2 + h^2)^{3/2}}, \\ B_{\mathrm{cor},z} &= \sum_{ij} \frac{B_{0,ij} h}{2\pi(x_{0,i}^2 + y_{0,j}^2 + h^2)^{3/2}}, \end{aligned} \tag{A2}$$

and the field strength of the potential field is

$$B_{\mathrm{cor}} = |B_{\mathrm{cor}}(r)| = \sqrt{B_{\mathrm{cor},x}^2 + B_{\mathrm{cor},y}^2 + B_{\mathrm{cor},z}^2}. \tag{A3}$$

The height of h of point P is assumed to be 7250 km ($10''$). In this method, all points in the selected subarea of the magnetogram contribute to the coronal field strength at point P.

APPENDIX B

MULTIPLE LINEAR REGRESSION FIT

To study the relationship between the observed $\log_{10}(\mathrm{PFF})$ as well as V_{CME} and the observed magnetic parameters (i.e., $\log_{10}B$, $\log_{10}S$, $\log_{10}\Phi$, θ_1, and θ_{12}) for our 18-event sample, we perform a multiple linear regression fit to the observed data by fitting a general linear equation. The fitting equation is expressed as

$$Y_{\mathrm{fit},\,j} = a_0 + \sum_{i=1}^{m} a_i X_{ij}, \tag{B1}$$

where X_{ij} is the measurement of the magnetic parameter i (e.g., $\log_{10}B_i$ or $\theta_{12,\,j}$, where $j = 1, 2, \ldots n$); and $Y_{\mathrm{fit},\,j}$ refers to the fitted values of $\log_{10}(\mathrm{PFF})$ and V_{CME}. In this equation, a_0 is a constant, a_i is the coefficient of each magnetic parameter, m is the number of parameters used in the fit, and n is the flare events number. Let $Y_{\mathrm{obs},\,j}$ be the observed values of $\log_{10}(\mathrm{PFF})$ and V_{CME}. The mean value of $Y_{\mathrm{fit},\,j}$ is assumed to be equal to the mean value of $Y_{\mathrm{obs},\,j}$, so equation (B1) yields

$$Y_{\mathrm{fit},\,j} - \overline{Y_{\mathrm{obs}}} = \sum_{i=1}^{m} a_i\left(X_{ij} - \overline{X_i}\right), \tag{B2}$$

where $\overline{X_i}$ is the mean value of parameter X_{ij}.

The variance of $Y_{\mathrm{obs},\,j}$ due to a known magnetic parameter X_{ij} is defined as

$$\sigma_i^2 = \frac{1}{n}\sum_{j=1}^{n}\left[a_i(X_{ij} - \overline{X_i})\right]^2, \tag{B3}$$

and the variance due to other unknown parameters and/or measurement errors is defined as

$$\sigma_o^2 = \frac{1}{n}\sum_{j=1}^{n}(Y_{\mathrm{obs},\,j} - Y_{\mathrm{fit},\,j})^2. \tag{B4}$$

The total variance of $Y_{\mathrm{obs},j}$ is

$$\begin{aligned}\sigma_{\mathrm{tot}}^2 &= \frac{1}{n}\sum_{j=1}^{n}\left(Y_{\mathrm{obs},j} - \overline{Y_{\mathrm{obs}}}\right)^2 = \frac{1}{n}\sum_{j=1}^{n}\left[(Y_{\mathrm{obs},j} - Y_{\mathrm{fit},j}) + (Y_{\mathrm{fit},j} - \overline{Y_{\mathrm{obs}}})\right]^2\\ &= \frac{1}{n}\sum_{j=1}^{n}\left[\left(Y_{\mathrm{obs},j} - Y_{\mathrm{fit},j}\right)^2 + 2(Y_{\mathrm{obs},\,j} - Y_{\mathrm{fit},\,j})(Y_{\mathrm{fit},\,j} - \overline{Y_{\mathrm{obs}}}) + (Y_{\mathrm{fit},\,j} - \overline{Y_{\mathrm{obs}}})^2\right].\end{aligned} \tag{B5}$$

The last term on the right-hand side of equation (B5) can be written as

$$\frac{1}{n}\sum_{j=1}^{n}(Y_{\mathrm{fit},\,j} - \overline{Y_{\mathrm{obs}}})^2 = \frac{1}{n}\sum_{j=1}^{n}\left[\sum_{i=1}^{m} a_i(X_{ij} - \overline{X_i})\right]^2 = \frac{1}{n}\sum_{j=1}^{n}\left\{\sum_{i=1}^{m}\left[a_i(X_{ij} - \overline{X_i})\right]^2 + 2\sum_{k\neq i} a_i a_k (X_{ij} - \overline{X_i})(X_{kj} - \overline{X_j})\right\} \tag{B6}$$

The second terms on the right-hand side of equations (B5) and (B6) will be very small and can be neglected if there are no correlations between different magnetic parameters, and the sample is big enough. After inserting equations (B3) and (B4) to equation (B5), the total variance of $Y_{\mathrm{obs},\,j}$ can be approximated as

$$\sigma_{\mathrm{tot}}^2 \approx \sigma_o^2 + \sum_{i=1}^{m}\sigma_i^2. \tag{B7}$$

REFERENCES

Berger, T., & Lites, B. W. 2003, Sol. Phys., 213, 213
Canfield, R. C., Hudson, H. S., & McKenzie, D. E. 1999, Geophys. Res. Lett., 26, 627
Chen, A. Q., Chen, P. F., & Fang, C. 2006, A&A, 456, 1153
Emslie, A. G., et al. 2004, J. Geophys. Res., 109, A10104
Falconer, D. A., Moore, R. L., & Gary, G. A. 2006, ApJ, 644, 1258
Gopalswamy, N., Yashiro, S., Kaiser, M. L., Howard, R. A., & Bougeret, J.-L. 2001, J. Geophys. Res., 106, 29219
Green, L. M., Démoulin, P., Mandrini, C. H., & Van Driel-Gesztelyi, L. 2003, Sol. Phys., 215, 307
Guo, J., Zhang, H. Q., & Chumak, O. V. 2007, A&A, 462, 1121
Guo, J., Zhang, H. Q., Chumak, O. V., & Liu, Y. 2006, Sol. Phys., 237, 25

Ji, H. S., Huang, G. L., & Wang, H. M. 2007, ApJ, 660, 893
Ji, H. S., Huang, G. L., Wang, H. M., Zhou, T. H., Li, Y. P., Zhang, Y. A., & Song, M. T. 2006, ApJ, 636, L173
Jing, J., Song, H., Abramenko, V., Tan, C. Y., & Wang, H. M. 2006, ApJ, 644, 1273
Lara, A., Gopalswamy, N., Xie, H., Mendoza-Torres, E., Pérez-Eríquez, & Michalek, G. 2006, J. Geophys. Res., 111, A06107
Leblanc, Y., Dulk, G. A., Vourlidas, A., & Bourgeret, J. L. 2001, J. Geophys. Res., 106, 25301
Lin, J. 2002, Chinese J. Astron. Astrophys., 2, 539
———. 2004, Sol. Phys., 219, 169
Lin, J., & Forbes, T. 2000, J. Geophys. Res., 105, 2375
Liu, Y. 2007, ApJ, 654, L171
McAteer, R. T. J., Gallagher, P. T., Ireland, J., & Young, C. A. 2005, Sol. Phys., 228, 55
Moore, R. L., Sterling, A. C., Hudson, H. S., & Lemen, J. R. 2001, ApJ, 552, 833
Priest, E. R., & Forbes, T. G. 2002, Astron. Astrophys. Rev., 10, 313
Qiu, J., & Yurchyshyn, V. B. 2005, ApJ, 634, L121
Reeves, K. K. 2006, ApJ, 644, 592
Reeves, K. K., & Forbes, T. G. 2005, ApJ, 630, 1133
Rust, D. M., & Kumar, A. 1996, ApJ, 464, L199
St. Cyr, O. C., et al. 2000, J. Geophys. Res., 105, 18169
Su, Y. N., Golub, L., & Van Ballegooijen, A. A. 2007, ApJ, 655, 606 (Paper I)
Su, Y. N., Golub, L., Van Ballegooijen, A. A., & Gros, M. 2006, Sol. Phys., 236, 325
Venkatakrishnan, P., & Ravindra, B. 2003, Geophys. Res. Lett., 30, 2181
Vourlidas, A., Subramanian, P., Dere, K. P., & Howard, R. A. 2000, ApJ, 534, 456

CODEN:PASJA 59(SP3) S571–S869 (2007)

ISSN:0004–6264

Publications of the Astronomical Society of Japan

Special Issue: Initial Results from Hinode

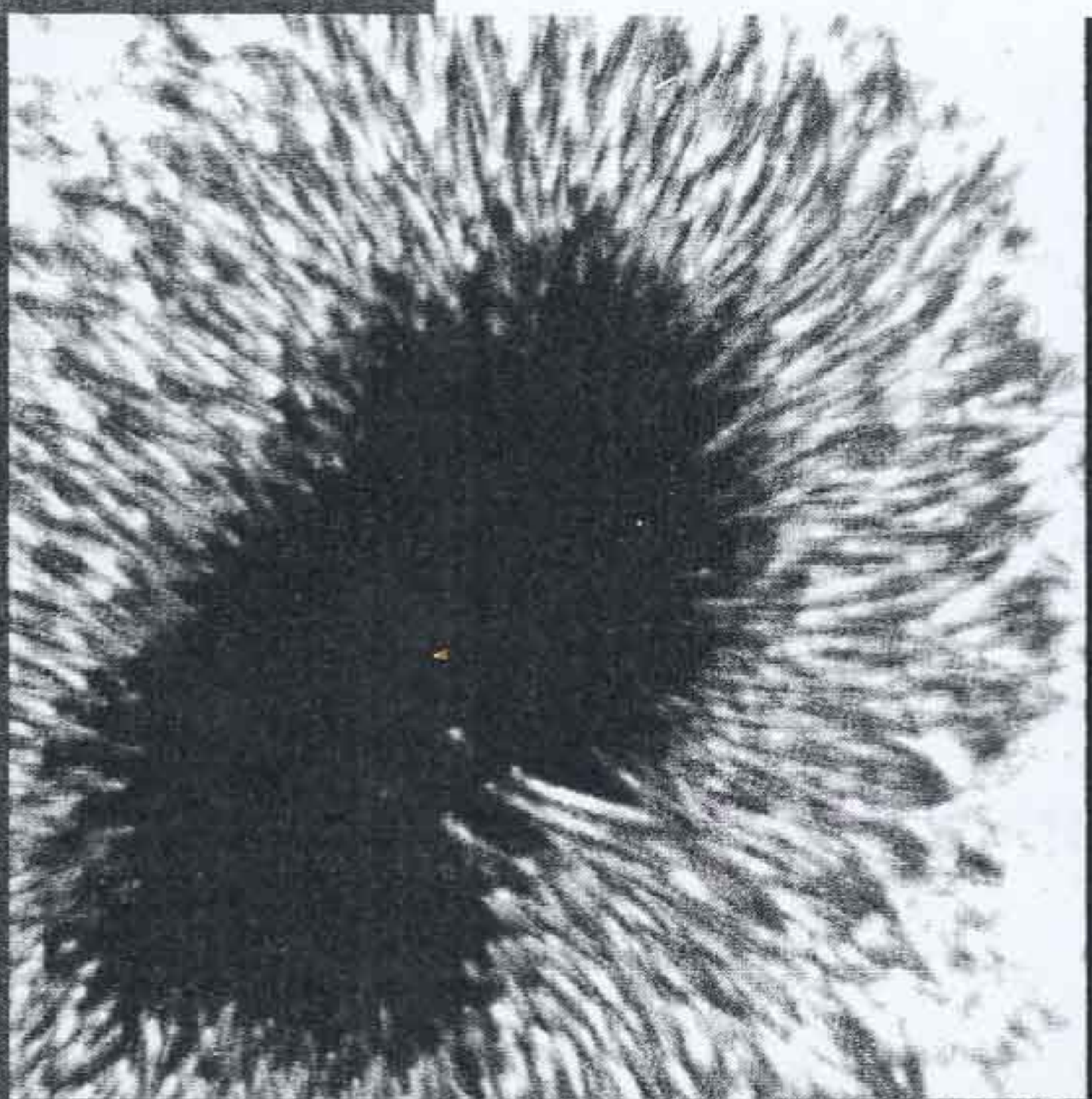

2007

Vol.59, No.SP3

Astronomical Society of Japan
(Founded in 1908)

CONTENTS OF VOLUME 59, No. SP3

Special Issue: Initial Results from Hinode

PASJ: Publ. Astron. Soc. Japan **59**, S785–S791, 2007 November 30

Evolution of the Sheared Magnetic Fields of Two X-Class Flares Observed by Hinode/XRT*

Yingna SU,[1,2,3] Leon GOLUB,[1] Adriaan VAN BALLEGOOIJEN,[1] Edward E. DELUCA,[1] Kathy K. REEVES,[1]
Taro SAKAO,[4] Ryouhei KANO,[5] Noriyuki NARUKAGE,[4] and Kiyoto SHIBASAKI[6]
[1]*Harvard-Smithsonian Center for Astrophysics, 60 Garden Street, Cambridge, MA 02138, USA*
ynsu@head.cfa.harvard.edu
[2]*Purple Mountian Observatory, 2 West Beijing Road, Nanjing 210008, P.R.China*
[3]*Graduate University of Chinese Academy of Sciences 19A Yuquanlu, Beijing 100049, P.R.China*
[4]*Institute of Space and Astronautical Science, Japan Aerospace Exploration Agency,*
3-1-1 Yoshinodai, Sagamihara, Kanagawa 229-8510
[5]*National Astronomical Observatory of Japan, 2-21-1 Osawa, Mitaka, Tokyo 181-8588*
[6] *Nobeyama Solar Radio Observatory, NAOJ, Minamimaki, Minamisaku, Nagano 384-1305*

(Received 2007 May 31; accepted 2007 August 17)

Abstract

We present multi-wavelength observations of the evolution of the sheared magnetic fields in NOAA Active Region 10930, where two X-class flares occurred on 2006 December 13 and December 14, respectively. Observations made with the X-ray Telescope (XRT) and the Solar Optical Telescope (SOT) aboard Hinode suggest that the gradual formation of the sheared magnetic fields in this active region is caused by the rotation and west-to-east motion of an emerging sunspot. In the pre-flare phase of the two flares, XRT shows several highly sheared X-ray loops in the core field region, corresponding to a filament seen in the TRACE EUV observations. XRT observations also show that part of the sheared core field erupted, and another part of the sheared core field stayed behind during the flares, which may explain why a large part of the filament is still seen by TRACE after the flare. About 2–3 hours after the peak of each flare, the core field becomes visible in XRT again, and shows a highly sheared inner and less-sheared outer structure. We also find that the post-flare core field is clearly less sheared than the pre-flare core field, which is consistent with the idea that the energy released during the flares is stored in the highly sheared fields prior to the flare.

Key words: Sun: corona — Sun: filaments — Sun: flares — Sun: magnetic fields — Sun: X-rays, gamma rays

1. Introduction

Solar flares, prominence eruptions, and coronal mass ejections (CMEs) are magnetic phenomena thought to be powered by the magnetic free energy (i.e., the difference between the total magnetic energy and the potential field magnetic energy) stored in the corona prior to eruption. The storage of free energy requires a nonpotential magnetic field, and is therefore associated with a shear or twist in the coronal field away from the potential, current-free state (Priest & Forbes 2002). One indication of such a stressed magnetic field is the presence of a prominence. Another important indicator of a stressed magnetic field is the presence of sigmoid signatures, discovered by Rust and Kumar (1997) and Canfield et al. (1999) with Yohkoh/SXT. Indeed, they have found that sigmoidal active regions to be the most likely to erupt.

A strong-to-weak shear motion of the hard X-ray footpoints during the flare was firstly reported by Masuda et al. (2001). This motion was claimed to be a common feature in two-ribbon flares by Su et al. (2007a), who identified this motion in 86% of 50 two-ribbon flares observed by TRACE. A further detailed study by Su et al. (2007b) shows that the change of the shear angle of the footpoints during the flare is positively correlated with the intensity of solar flare/CME events for an 18-event sample. Studies of both shear motion and contracting motion of the footpoints in several individual flares were carried out by Ji et al. (2006, 2007). A detailed interpretation of this shear motion was given by Su et al. (2006), based on a three-dimensional model for eruptive flares (Moore et al. 2001, and references therein). According to this model, the pre-flare configuration contains a highly sheared core field inside, and a less sheared envelope field outside in the pre-flare magnetic configuration. Does this configuration really exist? If so, how do the sheared fields build up? How do the sheared fields evolve during the flares? Continuous observations of NOAA Active Region (AR) 10930 by Hinode (Kosugi et al. 2007) provide an opportunity for us to address these questions. AR 10930 is a complex active region, which produced four X-class flares in 2006 December; two of them were observed by both the X-ray Telescope (XRT) and the Solar Optical Telescope (SOT) aboard Hinode. In this paper, we consider the evolution of the highly sheared coronal fields prior to, during, and after the flares, in order to obtain some insights into the physics of coronal storage and release of magnetic energy.

* Movies for figure 3 are available in the electronic version ⟨http://pasj.asj.or.jp/v59/sp3/59s332/⟩.

2. Instrumentation and Data

The Hinode satellite (previously called Solar-B) is equipped with three advanced solar telescopes, i.e., XRT, SOT, and the EUV Imaging Spectrometer (EIS). It was launched on 2006 September 22 (UT). XRT is a high-resolution grazing-incidence telescope, which provides unprecedented high-resolution, high cadence observations of the X-ray corona through a wide range of filters. XRT can "see" emission for a range of temperatures, $6.1 < \log T < 7.5$, with a temperature resolution of $\Delta(\log T) = 0.2$. Temperature discrimination is achieved with a set of diagnostic filters (nine X-ray filters in total) in the focal plane. XRT also contains visible light optics. The focal-plane detector of XRT is a $2\,\mathrm{k} \times 2\,\mathrm{k}$ back-illuminated CCD with $1''\!.0$ per pixel, giving a $2000''$ field of view (FOV), which can see the entire solar disk. Details of the XRT instrumentation and the performance can be found in DeLuca et al. (2005) and Golub et al. (2007).

The G band and Ca II H data used in this study are from the Broadband Filter Imager (BFI) of SOT (Tsuneta et al. 2007). BFI produces photometric images with broad spectral resolution in 6 bands (CN band, Ca II H line, G band, and 3 continuum bands) at the highest spatial resolution available from SOT ($0''\!.0541$/pixel) and at rapid cadence (< 10 s typical) over a $218'' \times 109''$ FOV. The scientific capabilities of SOT are described in detail by Shimizu (2004). The EUV (195 Å) images used in this study were taken by TRACE, which is a high-resolution imaging telescope (Handy et al. 1999). The photospheric magnetograms were taken by SOHO/MDI. The X-ray time profiles of the two X-class flares were obtained by GOES.

Two X-class flares occurred in AR 10930 on 2006 December 13 and 14, and were observed simultaneously by XRT and SOT onboard Hinode. These two flares are the first X-class flares observed by XRT of the Hinode mission since its launch. XRT started to observe this active region at 08:52 UT on 2006 December 9, and tracked this region continuously for the remainder of its disk passage. The XRT observations of this region were obtained with the Be-thin filter from December 9 to December 14, and the temperature-response curve of this filter can be found in Golub et al. (2007). Most of the XRT images were taken with a $512'' \times 512''$ FOV and a cadence of 60 s or less. Some full FOV X-ray images were also taken occasionally as context or synoptic images. Similar to XRT, SOT was also observing this active region at the same time. The SOT G band and Ca II H images were taken with a $218'' \times 109''$ FOV and a cadence of 120 s. TRACE was observing this region at 1600 Å and white light (WL) most of the time, and some EUV (195 Å) images were also taken from time to time.

All of the XRT data used in this study were calibrated using the standard Solar Soft IDL routines. We then normalized the calibrated XRT data to its maximum value (Dmax). The logarithm of the normalized XRT data is plotted in figures 1–5 (except figure 2) and movies 1 and 2, which refer to the XRT movies of the two flares. The maximum and minimum values of the data are 0 and -1.8 for most of the XRT images and the two movies, except for figures 3b–3d, which have a minimum value of -1.2. All of the XRT images in this paper are presented in a reversed color scale, but the TRACE and SOT images are in a normal color scale. To increase the signal-to-noise ratio of some of the XRT images, we first summed a series of XRT data within 10 minutes, then divided by the number of images. This method was adopted for figures 3b, 4c, and 5c; the time presented in the corresponding figures refers to the time of the first XRT image. This technique was used only for images that are very similar to each other.

The TRACE, XRT, and SOT images are co-aligned with the MDI images by applying the following procedure. For the December 13 flare, we first determined the offset of the TRACE coordinates by aligning the TRACE WL images with the corresponding WL images taken by MDI using the location of the sunspots. We then applied this offset to the TRACE EUV images used in this study. We applied the same method to determine the offset between the SOT and MDI images. The offset between the XRT and SOT images with corrected coordinates were determined by aligning the brightenings (i.e., flare footpoints) in the SOT Ca II H line images and the corresponding XRT images. We then applied the same procedure to align the images for the December 14 flare. We applied the same offset of the XRT images obtained from the December 13 flare to the XRT images on December 10 and 12; the misalignment of the XRT, SOT, and MDI images on December 10 and 12 is estimated to be less than $3''$.

3. Results

3.1. *Formation of the Sheared Magnetic Fields*

The formation process of the sheared magnetic fields observed by XRT aboard Hinode and SOHO/MDI is shown in figure 1. Corresponding to the X-ray images in figures 1a and 1f, the Hinode/SOT G band images overlaid without and with MDI photospheric magnetic field contours are displayed in the top and bottom panels of figure 2. Figure 1a shows that most of the X-ray loops overlying the magnetic inversion line (MIL, marked as a thick white line) are nearly perpendicular to the MIL, which indicates that the core field was close to a potential state at 00:19 UT on 2006 December 10. The corresponding G band images in figures 2a and 2c show that AR 10930 is composed of a bipole, which contains one big sunspot with negative magnetic fields (black contours) and a small spot with positive magnetic fields (white contours). The two spots share a common penumbra. Following Moore et al. (2001), we define the core field as the fields that are rooted close to the MIL through the middle of the bipole. This core field is visible in XRT observations most of the time. Around 22:46 UT on December 10, one bright loop with an obvious higher shear shows up on the right-hand side of the core field, while there are no obvious changes in the other loops (figure 1b). About 11 hours later, two highly sheared loops were visible in the XRT obserations (figure 1c), while we still saw no shear increase in the rest of the loops. Figure 1d shows an X-ray image taken 12 hours later than that presented in figure 1c. Most of the X-ray loops in the core field region in figure 1d have a higher shear than those in figure 1c. The core field in figure 1d shows an S-shaped structure (i.e., Sigmoid) composed of two sets of disconnected loops; also, a clearer

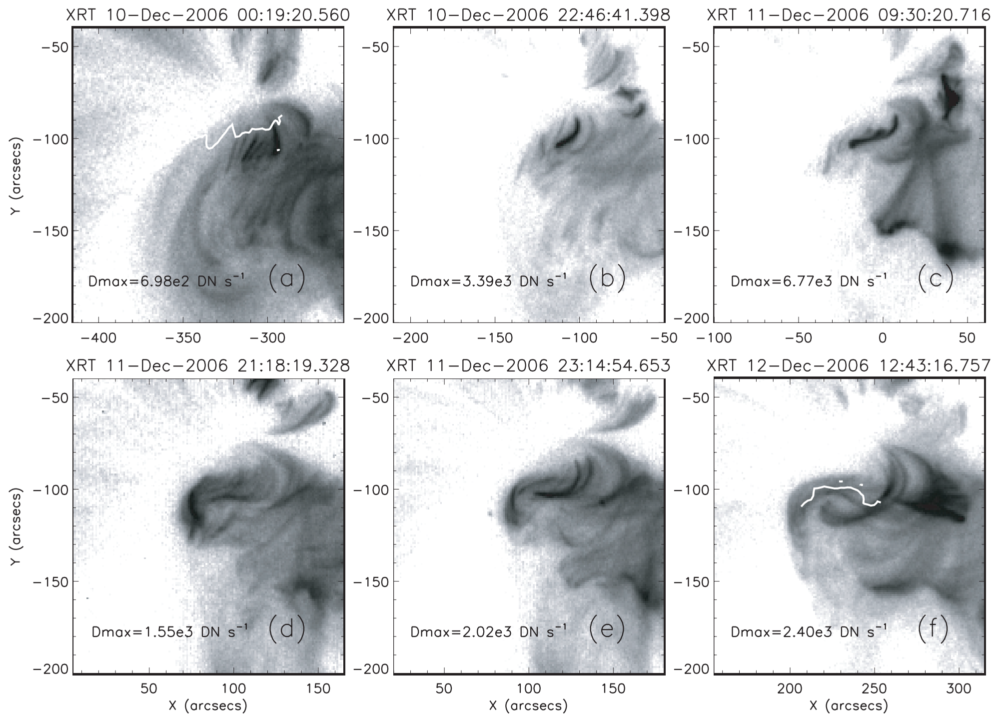

Fig. 1. Formation of the sheared magnetic fields observed by XRT aboard Hinode. (a)–(f) A series of X-ray images observed with Be-thin filter by XRT from 2006 December 10 to December 12. The maximum intensity (Dmax) of the XRT image is shown in the lower-left corner of each panel. The SOHO/MDI photospheric magnetic inversion line is represented as a thick white line.

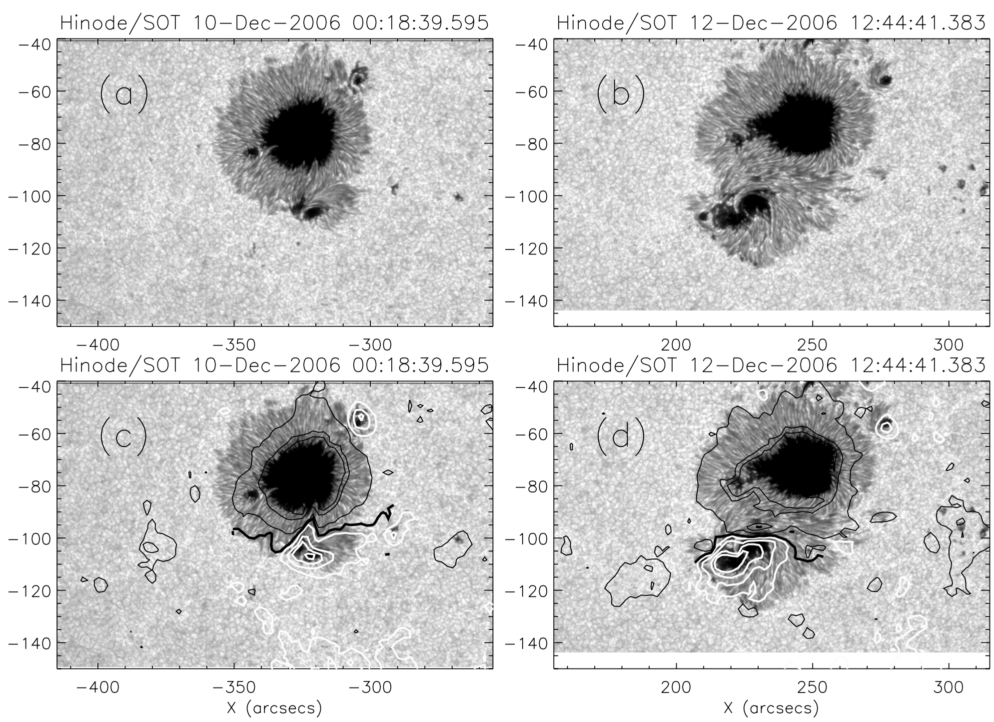

Fig. 2. Hinode/SOT G band images overlaid with SOHO/MDI magnetic contours. (a) and (b): G band images closest in time to the X-ray images in figures 1a and 1f, respectively. (c) and (d): Same G band images as in (a) and (b) overlaid with MDI magnetic contours. The white and black contours represent the positive and negative line-of-sight photospheric magnetic fields observed by MDI, and the thick black line represent the magnetic inversion line.

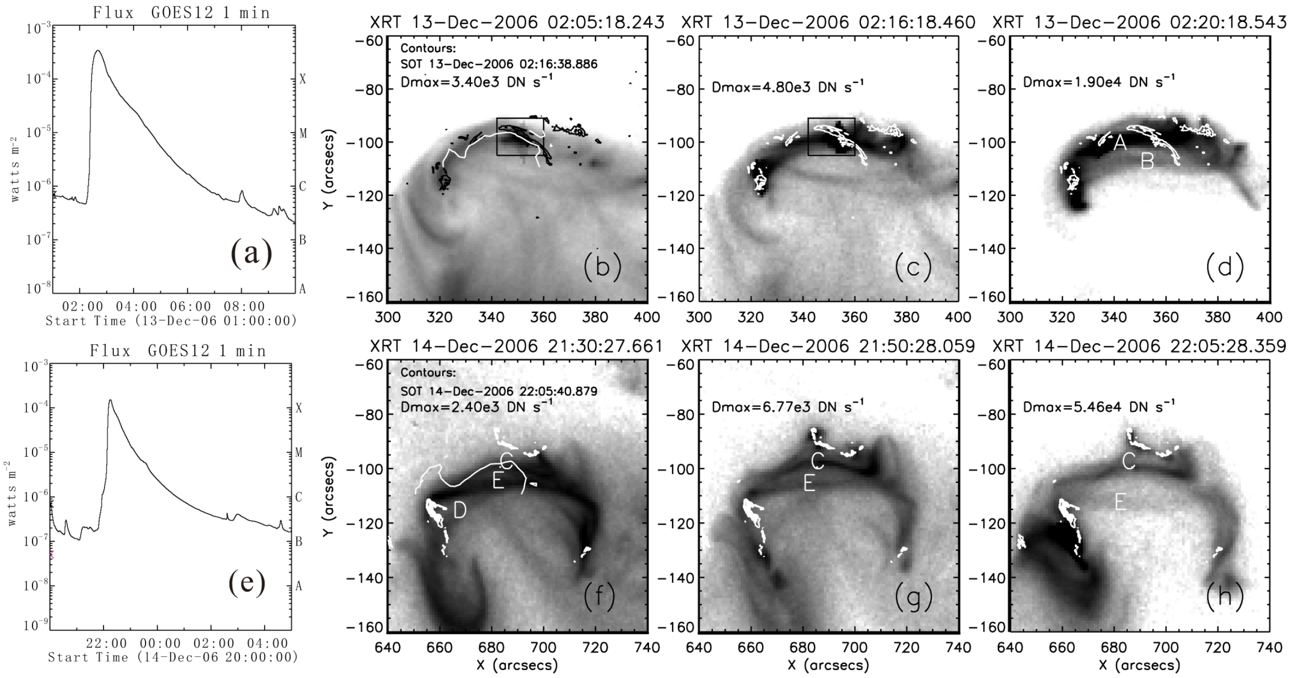

Fig. 3. XRT observations of the sheared magnetic field evolution during two X-class flares. (a) and (e): GOES X-ray time profiles for the 2006 December 13 and December 14 flares. (b) shows an XRT image prior to the December 13 flare, and two XRT images during this flare are presented in (c) and (d). The long-lasting brightening prior to the flare is enclosed by the black box in (b) and (c). The contours in (b)–(d) refer to the brightenings at 02:16 UT observed by SOT in Ca II H. (f)–(h) The XRT images at the early phase of the December 14 flare. The white contours overlaid on these images represent the brightenings at 22:05 UT on December 14 observed by SOT in Ca II H. The white lines in (b) and (f) refer to the SOHO/MDI magnetic inversion line. The maximum intensity (Dmax) of the XRT image is shown in the upper-left corner of each panel. A–E are the loops discussed in the text.

S-shaped structure can be seen in figure 1e. Most of the magnetic loops in the core field region became nearly parallel to the MIL by 12:43 UT on 2006 December 12 (figure 1f), which indicates that the coronal core field had become highly non-potential. The corresponding SOT image (figures 2b and 2d) shows that the penumbral fibrils between the two sunspots was also nearly parallel to the MIL, which indicates that the photospheric core field was also highly non-potential at this time.

Figure 1 shows that it took about two and a half days for the formation of the sheared coronal core field in AR 10930. The SOT G band and MDI movies in this time period show that the lower positive polarity spot was rotating in a counter-clockwise direction, while there is no evidence of rotation in the upper sunspot. A large amount of magnetic flux emerged to the west of the positive polarity spot, and newly emerged following flux accumulated in the spot as it rotated. A clear west-to-east motion of the lower spot can also be seen in a comparison of figures 2a and 2b. All of these observations appear to indicate that the highly sheared core field in AR 10930 is formed by this flux emergence and the accompanying rotation and west-to-east motion of the lower positive polarity sunspot.

3.2. *Evolution of Sheared Magnetic Fields during the Flares*

The evolution of the sheared X-ray loops observed by XRT during the December 13 and December 14 flares are presented in the top and bottom panels of figure 3, respectively. The GOES soft X-ray time profile of the December 13 flare (figure 3a) shows that it is an X3.4 flare, which started at 02:14 UT, peaked at 02:40 UT, and ended around 09:00 UT. An X-ray image prior to the flare is displayed in figure 3b, and two X-ray images from the early phase of the flare are shown in figures 3c and 3d. The black or white contours overlaid on these three X-ray images refer to the first brightenings seen in the SOT Ca II H line observations at 02:16 UT. At about 10 minutes prior to the flare, two compact brightenings in the highly sheared core field region started to appear, and the long-lasting one is shown to be enclosed by a black box in figures 3b and 3c. After the flare onset, several brightenings showed up in the footpoints of the highly sheared loops (figure 3c), and the pre-flare compact brightening still exists, which is located between the two flare footpoints. An X-ray image taken four minutes later is shown in figure 3d, which shows two highly sheared and nearly parallel loops. The fainter loop (i.e., loop B) erupted, while the brighter loop (i.e., loop A) was left behind (see movie 1*). Later on, the flare propagated to the less sheared envelope field region, which is located outside of the core field. We can see a strong-to-weak shear motion of the footpoints in the SOT Ca II H line observations during this flare, meaning that the footpoints started far apart, but close to the MIL, then moved toward each other and away from the MIL.

Figure 3e shows that the December 14 flare is an X1.5 flare, which started at 21:07 UT, peaked at 22:15 UT, and ended around 04:00 UT on December 15. Figures 3f–3h show three X-ray images at the early phase of the flare. The white contours overlaid on these three X-ray images refer to the brightenings seen in the SOT Ca II H line observations at 22:05 UT, after

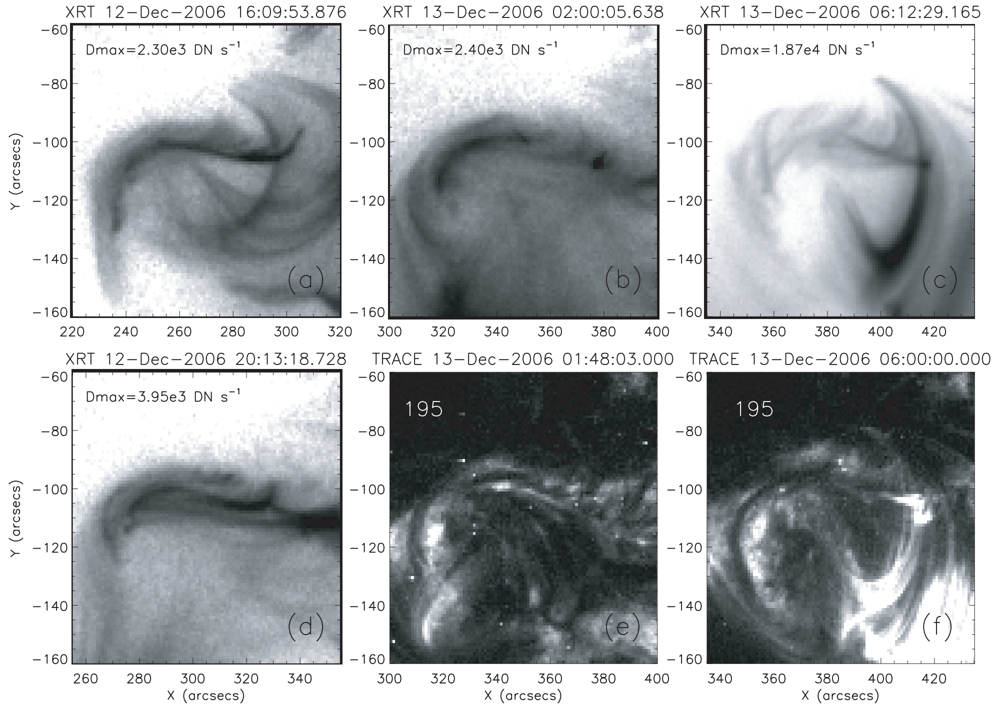

Fig. 4. Pre-flare and post-flare XRT and TRACE images of the X3.4 flare on 2006 December 13. (a), (b), and (d): Three X-ray images observed by XRT prior to the flare. (c) XRT image after the flare. (e) and (f): Two EUV images observed by TRACE prior to and after the flare for comparison with (b) and (c). The maximum intensity (Dmax) of the XRT image is shown in the upper-left corner of each panel.

which the flare ribbons started to extend along the MIL and moved away from the MIL rapidly. In the early phase, we identified three X-ray loops, i.e., loop C, loop D, and loop E, as shown in figure 3f. Loop D started to erupt around 21:26 UT (see movie 2*), after which we could see some brightenings (SOT Ca II H line) and post-flare loops (XRT) in the lower-left corner of figure 3f; some brightenings also appeared at the same position as the white contours close to loop C, which can be seen in figure 3g. From figure 3g we also see that loop E shows a continuous S-shaped structure, which is partly covered by white contours. A better view of this loop can be seen in movie 2. This S-shaped loop E started to erupt around 22:01 UT (see movie 2), which can be seen by a comparison of figures 3g and 3h. However, loop C showed no obvious motion during the entire flare process seen in the XRT observations. We also see a strong-to-weak shear motion of the footpoints in the SOT Ca II H line observations in this flare.

Both the December 13 and December 14 flares started from the highly sheared core field. In both of these flares, we can see that some of the highly sheared loops erupted, and other highly sheared loops were left behind. However, the initiation of the two flares appears to be different. In the December 13 flare, a compact brightening appeared first; we then see some brightenings (i.e., flare footpoints) located on the two opposite sides of the compact brightening. These observations indicate that magnetic reconnections may occur in the highly sheared core field, which leads to the eruption of the flare (or loop B). The loop that is left behind (i.e., loop A) appears to be a newly reconnected loop, because we see corresponding brightenings in the two ends of this loop after the flare onset. However, there is no evidence of magnetic reconnection before the eruption of loop D in the December 14 flare. After the eruption of loop D, we see some brightenings that appear to be the footpoints of the newly reconnected loops, after which loop E erupted too. The XRT movie of this flare shows that loop C that was left behind appears not to be involved in the flare process, which can also be seen in a comparison of figures 3f–3h.

3.3. *Pre-Flare vs. Post-Flare Sheared Magnetic Fields*

The continuous observations of AR 10930 by XRT with high spatial and temporal resolution provides us an excellent opportunity to compare the pre-flare and post-flare magnetic configurations. Figures 4a–4d show XRT observations of the core field before and after the X3.4 flare on 2006 December 13. The corresponding filaments before and after the flare observed by TRACE are displayed in figures 4e–4f. Prior to the December 13 flare, XRT had detected two loop eruptions (likely filament eruptions), which started around 16:28 and 21:58 UT on December 12, respectively. Figures 4a and 4d show the core field before and after the first loop eruption, respectively. Both of these figures show that most of the X-ray loops in the core field region were highly sheared and nearly parallel to each other, and the brightest loops had the appearance of a continuous S-shaped structure. The magnetic configuration after the second loop eruption and 14 minutes prior to the December 13 flare is displayed in figure 4b, which is composed of several highly sheared loops. After the December 13 flare onset, the post-flare loops gradually propagated from the highly sheared core field region to the outer and less-sheared envelope field region; during this time the less bright core field became invisible. Around 05:23 UT, the core field appeared again, and a clear picture

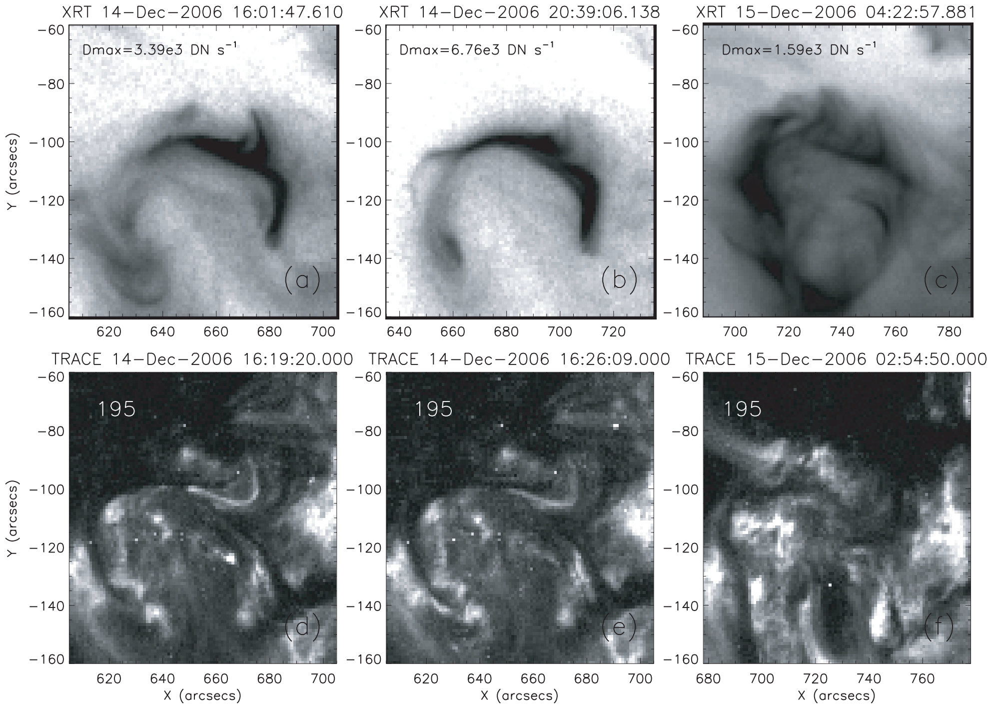

Fig. 5. Pre-flare and post-flare XRT and TRACE images for the X1.5 flare on 2006 December 14. (a) and (b): Two X-ray images observed by XRT prior to the flare. (c) XRT image after the flare. (d) and (e): Two EUV images observed by TRACE prior to the flare. (f) TRACE EUV image after the flare. The maximum intensity (Dmax) of the XRT image is shown in the upper left corner of each panel.

of the post-flare core field is displayed in figure 4c, which shows a higher sheared inner and less sheared outer structure (figure 4c). By comparing figures 4b and 4c, we can see that the post-flare core field was much less sheared than the pre-flare core field. Corresponding to the sheared core field observed by XRT, a filament is seen in TRACE prior to the December 13 flare (figure 4e). We still see most parts of the filament after the flare, as can be seen in figure 4f.

XRT images prior to and after the X1.5 flare on 2006 December 14 are shown in figures 5a–5c. The corresponding observations taken by TRACE are displayed in figures 5d–5f. A filament eruption occurred around 16:40 UT on December 14. One X-ray image prior to this eruption is shown in figure 5a, from which we see several highly sheared loops. A good TRACE image taken closest in time to figure 5a is shown in figure 5d. A comparison of the figures shows that the filament corresponds to a highly sheared X-ray loop. Figure 5b shows an X-ray image after the filament eruption and 30 minutes before the December 14 flare. We see no significant changes in the magnetic configuration before and after the filament eruption. Similar to the December 13 flare, the post-flare magnetic configuration of the December 14 flare shows a highly sheared inside and less sheared outside structure (figure 5c), and the post-flare core field is significantly less sheared than the pre-flare core field. Figure 5e shows the last good EUV image taken by TRACE prior to the December 14 flare, and a TRACE image after the flare is displayed in figure 5f. A comparison of figures 5e and 5f shows that a large part of the filament was still present after the flare.

4. Discussions and Conclusions

NOAA Active Region 10930 is a complex region, where four X-class flares occurred in 2006 December, and two of them (i.e., flares on December 13 and December 14) were observed by both XRT and SOT aboard Hinode. The continuous observations of this region by XRT and SOT provide an opportunity to study the long-term evolution of the sheared core field. In this paper, we have addressed three questions: How do non-potential magnetic fields build up? How do they evolve during flares? What is the difference between the pre-flare and post-flare magnetic configurations?

The XRT observations show that the coronal magnetic fields were close to a potential state at 00:19 UT on 2006 December 10. About 22 hours later, a shear increase started from one X-ray loop on the right-hand side of the core field rooted close to the MIL between the two main magnetic polarities. After that, more and more loops gradually became highly sheared. Most of the loops in the core field region became highly sheared and nearly parallel to the MIL around 12:43 UT on 2006 December 12. The formation of the sheared magnetic fields was caused by the counter-clockwise rotation and the west-to-east motion of the lower emerging sunspot, which can be seen in the SOT G band and Ca II H line observations as well as the SOHO/MDI observations.

Both of the X-class flares on December 13 and December 14 started from a highly sheared core field. At the early phase of each flare, some highly sheared loops erupted, and some highly sheared loops were left behind. The highly sheared loop that was left behind in the December 13 flare seems to be a newly reconnected post-flare loop. However, the one that was left behind in the December 14 flare appears not to have been involved in any reconnection, as can be seen in the XRT observations. Corresponding to the highly sheared core field, a filament was seen in the EUV observations by TRACE prior to the two flares. A large part of the filament was still present after these two flares, which may have been caused by the fact that only part of the sheared magnetic fields erupted during the flares. The partial filament eruption is interpreted as being a partial eruption of a magnetic flux rope by Gibson and Fan (2006). The initiation of these two flares seems to be different. The X3.4 flare on December 13 appears to have been initiated by magnetic reconnection in the highly sheared core field, which agrees with the cartoon of the three-dimensional model for eruptive flares in Moore et al. (2001). However, the X1.5 flare on December 14 started from a sheared loop eruption, before which we can see no evidence of magnetic reconnection.

Two loop eruptions (likely filament eruptions) were seen by XRT prior to the December 13 flare. Most of the loops in the core field were highly sheared and nearly parallel to each other before and after the first loop eruption. The core field before both the December 13 and December 14 flares was composed of several highly sheared loops. About 2–3 hours after the peak of each flare, the core field was visible again from the XRT observations. The post-flare core field of each flare showed a higher sheared inner and less sheared outer structure, but containing significantly less shear compared to the pre-flare core field. This flare-related relaxation of magnetic shear was also found by Yohkoh/SXT (Sakurai et al. 1992). This observation is in agreement with the idea that a flare is caused by the release of magnetic energy stored in the highly sheared magnetic fields, but apparently only a fraction of the available energy is released.

A strong-to-weak shear motion of the footpoints was observed in both of two flares on December 13 and 14. This motion suggests that the pre-flare magnetic field configuration is composed of a highly sheared core field and overlying less sheared envelope field. We did not see these overlying less-sheared envelope fields in the XRT observations prior to the two flares, which is in agreement with the Yohkoh/SXT observations (Sterling et al. 2000). Moreover, a long-term XRT observation of AR 10930 shows that the core field is visible most of the time, while the overlying loops can only be seen temporarily after the flares or loop eruptions. The heating mechanism for the core field is apparently different from that of the post-flare loops. We are left with two open questions: Why do we not see the overlying unsheared sheared loops in the pre-flare phase? What is the heating mechanism of the core field?

We thank the anonymous referee and the editors for valuable suggestions to improve this paper. Hinode is a Japanese mission developed and launched by ISAS/JAXA, with NAOJ as domestic partner and NASA and STFC (UK) as international partners. It is operated by these agencies in co-operation with ESA and the NSC (Norway). US members of the XRT team are supported by NASA contract NNM07AA02C to Smithsonian Astrophysical Observatory (SAO). The TRACE analyses are supported at SAO by a contract from Lockheed Martin. Y. Su is also supported by an SAO pre-doctoral Fellowship, the NSFC projects with 10333030 and 10273025, and "973" program with 2006CB806302.

References

Canfield, R. C., Hudson, H. S., & McKenzie, D. E. 1999, Geophys. Res. Lett., 26, 627
DeLuca, E. E., Weber, M. A., Sette, A. L., Golub, L., Shibasaki, K., Sakao, T., & Kano, R. 2005, Adv. Space Res., 36, 1489
Gibson, S. E., & Fan, Y. 2006, ApJ, 637, L65
Golub, L., et al. 2007, Sol. Phys., 243, 63
Handy, B. N., et al. 1999, Sol. Phys., 187, 229
Ji, H., Huang, G., & Wang, H. 2007, ApJ, 660, 893
Ji, H., Huang, G., Wang, H., Zhou, T., Li, Y., Zhang, Y., & Song, M. 2006, ApJ, 636, L173
Kosugi, T., et al. 2007, Sol. Phys., 243, 3
Masuda, S., Kosugi, T., & Hudson, H. S. 2001, Sol. Phys., 204, 55
Moore, R. L., Sterling, A. C., Hudson, H. S., & Lemen, J. R. 2001, ApJ, 552, 833
Priest, E. R., & Forbes, T. G. 2002, A&AR, 10, 313
Rust, D. M., & Kumar, A. 1996, ApJ, 464, L199
Sakurai, T., Shibata, K., Ichimoto, K., Tsuneta, S., & Acton, L. W. 1992, PASJ, 44, L123
Shimizu, T. 2004, in ASP Conf. Ser. 325, The Solar-B Mission and the Forefront of Solar Physics, ed. T. Sakurai & T. Sekii (San Francisco: ASP), 3
Sterling, A. C., Hudson, H. S., Thompson, B. J., & Zarro, D. M. 2000, ApJ, 532, 628
Su, Y., Golub, L., & van Ballegooijen, A. A. 2007a, ApJ, 655, 606
Su, Y., Golub, L., van Ballegooijen, A. A., & Gros, M. 2006, Sol. Phys., 236, 325
Su, Y., van Ballegooijen, A., McCaughey, J., DeLuca, E., Reeves, K. K., & Golub, L. 2007b, ApJ, 665, 1448
Tsuneta, S., et al. 2007, Sol. Phys. submitted

ISSN: 0004-637X

THE ASTROPHYSICAL JOURNAL

VOLUME 691, PART 1 2009 JANUARY 20 NUMBER 1

(Continued on inside page)

Published for the
AMERICAN ASTRONOMICAL SOCIETY
by
IOP Publishing

(Continued from preceding page)

(Continued on following page)

(Continued from preceding page)

(Continued on following page)

(Continued from preceding page)

The Astrophysical Journal, 691:105–114, 2009 January 20 doi:10.1088/0004-637X/691/1/105

OBSERVATIONS AND NONLINEAR FORCE-FREE FIELD MODELING OF ACTIVE REGION 10953

Yingna Su[1,2], Adriaan van Ballegooijen[1], Bruce W. Lites[3], Edward E. DeLuca[1], Leon Golub[1], Paolo C. Grigis[1], Guangli Huang[2], and Haisheng Ji[2]
[1] Harvard-Smithsonian Center for Astrophysics, Cambridge, MA 02138, USA; ynsu@head.cfa.harvard.edu
[2] Purple Mountain Observatory, Nanjing, 210008, China
[3] High Altitude Observatory, P.O. Box 3000, Boulder, CO 80307-3000, USA
Received 2008 August 6; accepted 2008 September 22; published 2009 January 7

ABSTRACT

We present multiwavelength observations of a simple bipolar active region (NOAA 10953), which produced several small flares (mostly B class and one C8.5 class) and filament activations from April 30 to May 3 in 2007. We also explore nonlinear force-free field (NLFFF) modeling of this region prior to the C8.5 flare on May 2, using magnetograph data from *SOHO*/MDI and *Hinode*/SOT. A series of NLFFF models are constructed using the flux-rope insertion method. By comparing the modeled field lines with multiple X-ray loops observed by *Hinode*/XRT, we find that the axial flux of the flux rope in the best-fit models is $(7 \pm 2) \times 10^{20}$ Mx, while the poloidal flux has a wider range of $(0.1\text{–}10) \times 10^{10}$ Mx cm^{-1}. The axial flux in the best-fit model is well below the upper limit ($\sim 15 \times 10^{20}$ Mx) for stable force-free configurations, which is consistent with the fact that no successful full filament eruption occurred in this active region. From multiwavelength observations of the C8.5 flare, we find that the X-ray brightenings (in both *RHESSI* and XRT) appeared about 20 minutes earlier than the EUV brightenings seen in TRACE 171 Å images and filament activations seen in MLSO Hα images. This is interpreted as an indication that the X-ray emission may be caused by direct coronal heating due to reconnection, and the energy transported down to the chromosphere may be too low to produce EUV brightenings. This flare started from nearly unsheared flare loop, unlike most two-ribbon flares that begin with highly sheared footpoint brightenings. By comparing with our NLFFF model, we find that the early flare loop is located above the flux rope that has a sharp boundary. We suggest that this flare started near the outer edge of the flux rope, not at the inner side or at the bottom as in the standard two-ribbon flare model.

Key words: Sun: corona – Sun: filaments – Sun: flares – Sun: magnetic fields – Sun: photosphere – Sun: X-rays, gamma rays

Online-only material: color figure, mpeg animation

1. INTRODUCTION

It is well accepted that solar flares, prominence eruptions, and coronal mass ejections (CMEs) are different manifestations of a single physical process thought to be powered by the release of free energy stored in the corona prior to the activities. Storage of free energy requires a non-potential magnetic field, and it is therefore associated with a shear or twist in the coronal field away from the potential, current-free state (Priest & Forbes 2002). Twisted or sheared magnetic fields are often visible in the solar corona before solar eruptions (Rust & Kumar 1996; Canfield et al. 1999; Moore et al. 2001; Su et al. 2006, 2007a; 2007b, Ji et al. 2008), but it is unclear how the eruption gets started. To determine what triggers such eruptions and how the energy is released, we need to understand the three-dimensional (3D) structure of the coronal magnetic field configuration prior to the flare. Therefore, modeling of the preflare nonpotential fields is needed.

In this paper, we consider a C8.5 flare that occurred in Active Region (AR) 10953 on 2007 May 2, and we develop a model for the nonpotential fields before the flare. The evolution of the sheared magnetic field in this region was studied by Okamoto et al. (2008), using vector magnetograms from *Hinode*/SOT/SP. They suggested that the observed vector fields show the evidence for the emergence of a magnetic flux rope. The purpose of the current paper is to develop a 3D magnetic model of this flux rope, and to study where the flare occurs in relationship to the flux rope.

A realistic way to model the nonpotential coronal fields in active regions is to assume that the electric currents are parallel to the magnetic field, $\nabla \times \vec{B} = \alpha \vec{B}$, with α being constant only along every field line ($\vec{B} \cdot \nabla\alpha = 0$) but varying from field line to field line, giving us the nonlinear force-free field (NLFFF). Several authors have developed methods for reconstructing the NLFFFs by extrapolating observed photospheric vector fields into the corona (e.g., Mikić & McClymont 1994; Wheatland et al. 2000; Yan & Sakurai 2000; Bleybel et al. 2002; Régnier et al. 2002; Wheatland 2006; Wiegelmann 2004; Wiegelmann et al. 2006; Song et al. 2006). For reviews of these various methods, see Schrijver et al. (2006, 2008), Wiegelmann (2008), and Metcalf et al. (2008).

Measurements of photospheric vector magnetic fields and their use as boundary conditions in extrapolation are subject to a number of uncertainties (see McClymont et al. 1997). Most importantly, the magnetic field in the photosphere is not force free, and the highly sheared field in the filament channel is not always visible in the photosphere where the vector field measurements are made (Lites 2005). Therefore, in the present study we construct NLFFF models using the flux rope insertion method (van Ballegooijen 2004; van Ballegooijen & Mackay 2007), which uses observational constraints from coronal images in combination with photospheric magnetograms. The method only requires the radial component of the magnetic field in the photosphere, and therefore is less affected by errors in transverse field measurement. Using an improved version of this method, Bobra et al. (2008) constructed NLFFF models for two active

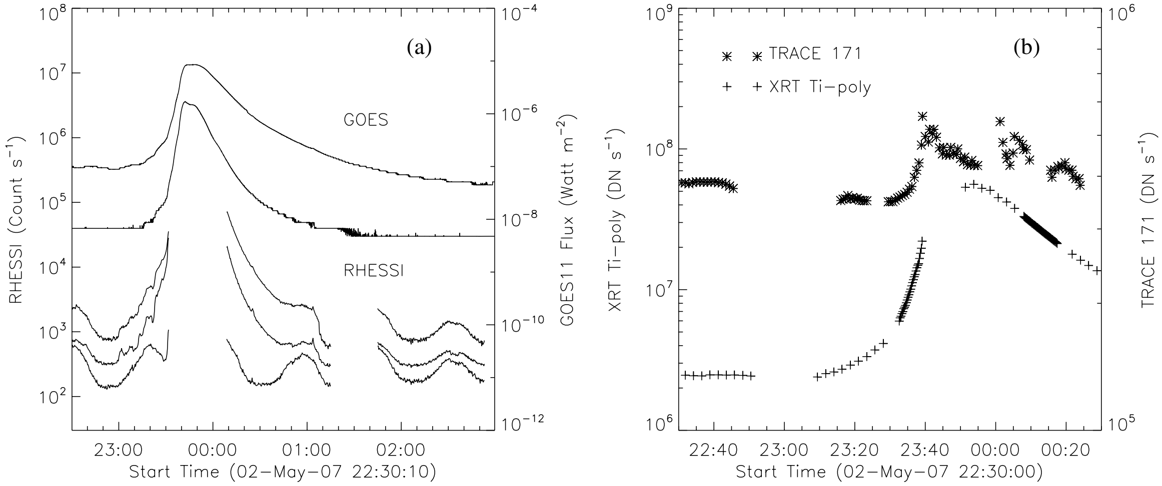

Figure 1. Light curves for the C8.5 two-ribbon flare occurred on 2007 May 2. The top two curves in the left panel refer to the *GOES* soft X-ray light curves at 1.0–8.0 Å and 0.5–4.0 Å while the bottom three, from top to bottom, refer to RHESSI X-ray light curves at 3–6 keV, 6–12 keV, and 12–25 keV, respectively. The RHESSI light curve at 3–6 keV is multiplied by 4 in order to give a nicer display. *TRACE* EUV and XRT X-ray light curves are marked by star sign and plus sign on the right panel, respectively.

regions based on magnetograms from the Michelson Doppler Images (MDI) aboard *SOHO* and nonpotential structures seen in *TRACE* EUV images. They found that *TRACE* images are not well suited to the task of finding sheared fields near polarity inversion lines (PILs). Therefore, in the current paper multiple nonpotential X-ray loops observed by *Hinode*/XRT are used to constrain the models. We also use vector magnetograms from *Hinode*/SOT/SP to derive the radial field in the photosphere. This allows us to correct for the fact that the observed AR is about 15° away from the disk center.

This paper is organized as follows. Section 2 describes the observations, and Section 3 describes how the NLFFF models are constructed and the modeling results. The discussion and interpretation are given in Section 4. Conclusions are presented in Section 5.

2. OBSERVATIONS

2.1. Data Sets and Instruments

NOAA Active Region (AR) 10953 is a simple bipolar active region, which produced several filament activations and small flares (< M class) in 2007 May. A long-term movie of the *SOHO*/MDI magnetograms shows that the leading sunspot in this active region is a decaying sunspot, which ejected numerous magnetic elements toward the polarity inversion line, where flux cancellations frequently occurred.

A C8.5 (*GOES* soft X-ray class) two-ribbon flare associated with a filament activation occurred in AR 10953 around 23:20 UT on 2007 May 02. This event was well observed in multiple wavelengths, i.e., soft X-rays by the X-ray Telescope (XRT; Golub et al. 2007) onboard *Hinode* (Kosugi et al. 2007), EUV by the *Transition Region and Coronal Explorer* (*TRACE*; Handy et al. 1999), and Hα by the Polarimeter for Inner Coronal Studies (PICS) which has been operated by the High Altitude Observatory at the Mauna Loa Solar Observatory (MLSO) since 1994. This flare was also observed by *RHESSI* (Lin et al. 2002) except the two gaps caused by the night time of the spacecraft. The full disk Hα images (∼1″.09 pixel^{-1}) taken at the Kanzelhöhe Solar Observatory (KSO) are also used. The XRT images presented in this study are taken with the Ti-poly filter and have field of view (FOV) of 512″×512″. The spatial resolution is around 2″ (1″.032 pixel^{-1}). The TRACE EUV images are taken at 171 Åwith an FOV of 1024″×1024″, and the spatial resolution is 1″. The full disk Hα images taken by PICS with 3 minute cadence have a spatial resolution of 2″.9. The X-ray light curves of this event are provided by *GOES* and *RHESSI*.

The magnetic field information is obtained from the line-of-sight photospheric magnetograms from *SOHO*/MDI and vector magnetogram from the Spectro-Polarimeter (SP) of the Solar Optical Telescope (SOT; Tsuneta et al. 2008) onboard *Hinode*. The *Hinode* SP data were calibrated with the standard "SP_ PREP" software. The calibrated Stokes spectra were then subjected to the Milne–Eddington inversion procedure developed for the HAO/Advanced Stokes Polarimeter (Skumanich & Lites 1987; Lites & Skumanich 1990; Lites et al. 1993) to derive the magnetic field vector, fill fractions, and thermodynamic parameters over the map. No inversion was attempted for regions of the map where the net line polarization did not exceed 0.4%. For those regions we assumed the field to be vertical and equal to the apparent flux density derived from the integrated Stokes V polarization signal. We then resolved the 180° azimuth ambiguity with the AZAM utility (Lites et al. 1995), which minimizes the spatial discontinuities in the azimuth angle when viewed in the local reference frame.

The *TRACE* and XRT images are co-aligned with the MDI magnetograms by applying the following procedures. We first determined the offset of the *TRACE* coordinates by aligning the *TRACE* WL images with the corresponding WL images taken by MDI using sunspots as references. The offset between the XRT and *TRACE* images with corrected coordinates is determined by aligning the brightenings (i.e., flare footpoints) in the *TRACE* EUV images and the corresponding XRT images. We aligned the Hα images from the PICS and KSO with the MDI magnetograms by eye.

The XRT images prior to the C8.5 flare show a number of highly sheared loops that indicate the presence of a coronal flux rope or highly sheared arcade above the PIL of the AR. These loops will be described in Section 3.2, where we use these loops to construct nonpotential field models of the AR.

2.2. Pre-EUV Flare X-ray Brightenings

The *GOES* (top two) and *RHESSI* (bottom three) X-ray light curves for the C8.5 two-ribbon flare are shown in Figure 1(a).

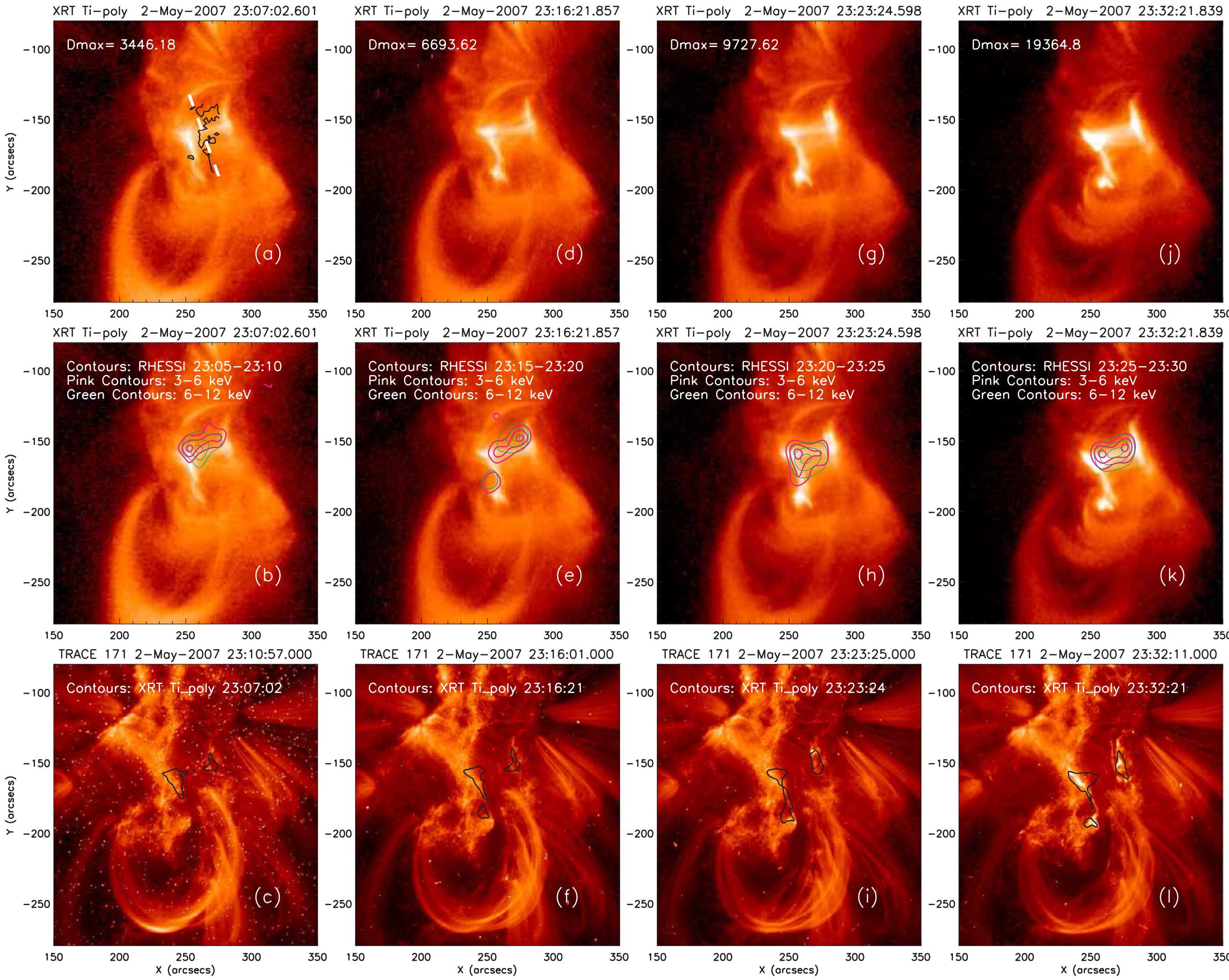

Figure 2. Pre-EUV X-ray brightenings during the C8.5 flare. The background images in the top and middle panels show the XRT observations at the early phase of the C8.5 flare. The XRT data are plotted in logarithm scale, and the maximum intensity (Dmax, DN s^{-1}) of the XRT images is shown on the top of each panel. The white line in panel (a) refers to the polarity inversion line obtained from MDI magnetogram, and the black dashed line is a simplified PIL corresponding to the Hα filament. The white and gray contours overlaid on the middle panels refer to 3–6 keV and 6–12 keV *RHESSI* observations, respectively. The X-ray contours (XRT) overlaid on the corresponding *TRACE* EUV images are shown in the bottom panels.

(A color version of this figure is available in the online journal.)

The two gaps in *RHESSI* light curves are during its night times. *GOES* light curves show that the flare started around 23:12 UT and peaked at 23:48 UT on 2007 May 2, and ended about 02:00 UT on 2007 May 3. Small spikes started to be seen after 23:00 UT in the lower energy band (3–6 keV and 6–12 keV) of *RHESSI* light curves. The higher energy band (12–25 keV) was dominated by the background most of the time, and a real increase in the light curve started around 23:30 UT. Figure 1(b) shows the integrated light curve of the flare region (as shown in Figure 2) in *TRACE* EUV and XRT X-rays. The first gap in the *TRACE* light curve is a real observational data gap. We also removed the images with strong particle hits, which lead to the other three gaps in the *TRACE* light curve. The images during the first gap in the XRT light curve were affected by strong atmospheric absorption. The images during the other gaps of the XRT light curve are saturated. From this figure we see that the soft X-ray light curve began to rise around 23:10 UT (similar to *GOES*), while the EUV flare started about 20 minutes later.

Figure 2 shows the XRT, *RHESSI*, and *TRACE* EUV images at the early phase of the C8.5 flare. The XRT data used in this figure are normalized to its maximum value (Dmax, in unit of DN s^{-1}), which is presented in the top of each panel. At 23:07 UT, XRT started to see two short ribbon-like brightenings connected by a loop that is nearly perpendicular to the underlying PIL (black and white lines in Figure 2(a)). Corresponding X-ray sources are seen in RHESSI observations in its lowest energy band (see Figure 2(b)). There are no counterparts of the X-ray brightenings in the EUV image as seen from Figure 2(c). A similar result is obtained from the observations at 23:16 UT and 23:23 UT (the middle two columns of Figure 2). A filament activation began around 23:20 UT, after which a rapid increase is seen in the *GOES* light curve, and tiny EUV footpoint brightenings became visible (Figure 2i). However, the EUV brightenings are much smaller than the corresponding X-ray brightenings at this time. Several minutes later, most of the EUV counterparts of the X-ray brightenings can be seen in the *TRACE* images (Figures 2l).

2.3. *Evolution of the Filament Activation*

The evolution of the filament activation associated with the C8.5 flare in Hα (MLSO/PICS) is shown in the top panels of

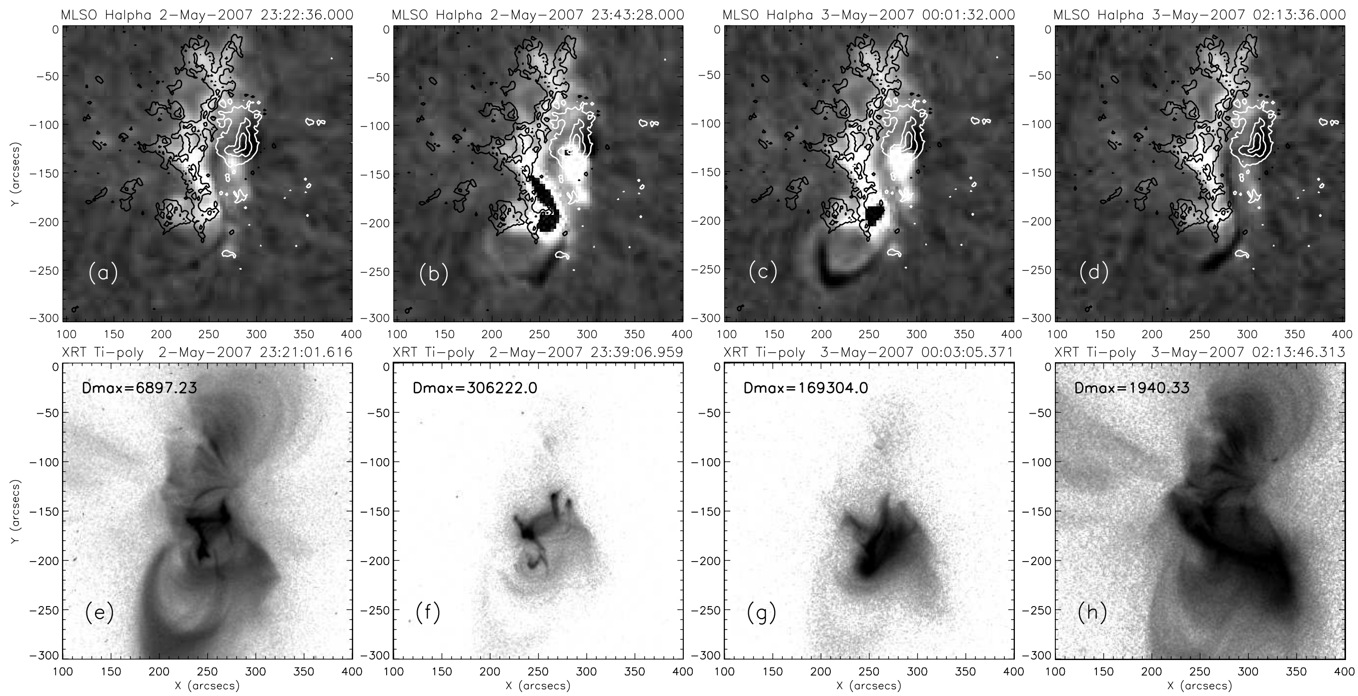

Figure 3. Evolution of the filament activation associated with the C8.5 flare. The top panels show the MLSO/PICS Hα observations of this filament activation. The white and black contours refer to the negative and positive magnetic fields observed by *SOHO*/MDI. The corresponding closest in time *Hinode*/XRT images are shown in the bottom panels. The evolution of this filament activation (in Hα, *TRACE* EUV, and XRT) is also available as a video in the electronic edition of the *Astrophysical Journal*.

Figure 3. The Hα image at the onset of the filament activation is displayed in Figure 3(a), which shows that the northern end of the filament is rooted in the leading sunspot with negative polarity (*white contours*), but the southern end of this filament is unclear. This southern end of the filament is very unstable, and many activations were observed at multiple wavelengths (i.e., Hα, EUV, and X-ray) from April 30 to May 3. After 23:20 UT, a large amount of filament material moved from the northern part of the filament to the southern part (Figure 3(b)), then streamed into the nearby positive polarity region (Figure 3(c)). This filament activation was also seen in *TRACE* EUV observations (see online video), while no clear evidence is seen in the X-ray images as shown in the bottom panels of Figure 3. Figure 3(d) shows an Hα image at about three hours after the onset of the filament activation. A comparison of Figures 3(a) and 3(d) shows that the shapes of the filament before and after the activation are very similar, but the Hα filament after the activation appears to be darker than before.

3. NLFFF MODELING

3.1. Flux Rope Insertion Method

A flux rope insertion method has been developed by van Ballegooijen (2004) and van Ballegooijen & Mackay (2007) for constructing NLFFF models of solar active regions and filaments. In this paper, we use an improved version of this method; a detailed description can be found in Bobra et al. (2008). The method involves inserting a magnetic flux rope into a potential-field model of an active region; the axial flux $\Phi_{\rm axi}$ and poloidal flux $F_{\rm pol}$ of the flux rope are treated as free parameters. Magnetofrictional relaxation is applied by solving the MHD induction equation, including the effects of magnetic diffusion (see equation A2 in Bobra et al. 2008). The computation is done on a 3D grid in spherical coordinates with the lower boundary located at the photosphere. At the lower boundary of the computation domain only the *radial* component B_r of the magnetic field needs to be specified; the tangential components B_θ and B_ϕ are allowed to vary in the relaxation process. The parameters $\Phi_{\rm axi}$ and $F_{\rm pol}$ are estimated by comparing the modeled field lines with observed Hα filaments and coronal loops.

The use of magnetic diffusion in NLFFF relaxation was investigated by Roumeliotis (1996), who used resistive diffusion in order to change the magnetic topology of the modeled field. The resistivity was assumed to be proportional to the magnitude of the Lorentz force, $\eta \sim |\mathbf{j} \times \mathbf{B}|$, where $\mathbf{B}$ is the magnetic field and $\mathbf{j}$ is the electric current density. The advantage of this approach is that diffusion occurs only in the unrelaxed state far from force-free equilibrium, not in the relaxed state when $|\mathbf{j} \times \mathbf{B}|$ is almost zero. However, in the present case, we want to preserve the magnetic topology of the flux rope as best as possible. Ordinary (resistive) diffusion does not conserve magnetic helicity (Berger 1984), so significant changes in topology can occur during the relaxation process. In the present work, we use *hyperdiffusion*, which is a type of magnetic diffusion that conserves magnetic helicity and is described by a fourth-order diffusion operator (see van Ballegooijen & Cranmer 2008, and references therein). The advantage of hyperdiffusion in the present application is that it acts to suppress small-scale numerical artifacts in the electric current distribution without significantly affecting the large-scale electric currents. Therefore, the topology of the magnetic field is nearly conserved during the relaxation process.

In this paper, we apply the flux rope insertion method to AR 10593 as observed on 2007 May 2 at 17:30 UT. The radial field B_r in the central part of the AR was derived from a photospheric vector magnetogram obtained with SOT/SP. The observed vector field was rotated to the local reference frame and remapped onto the longitude–latitude grid at the base of the 3D model. This grid has a heliocentric angular

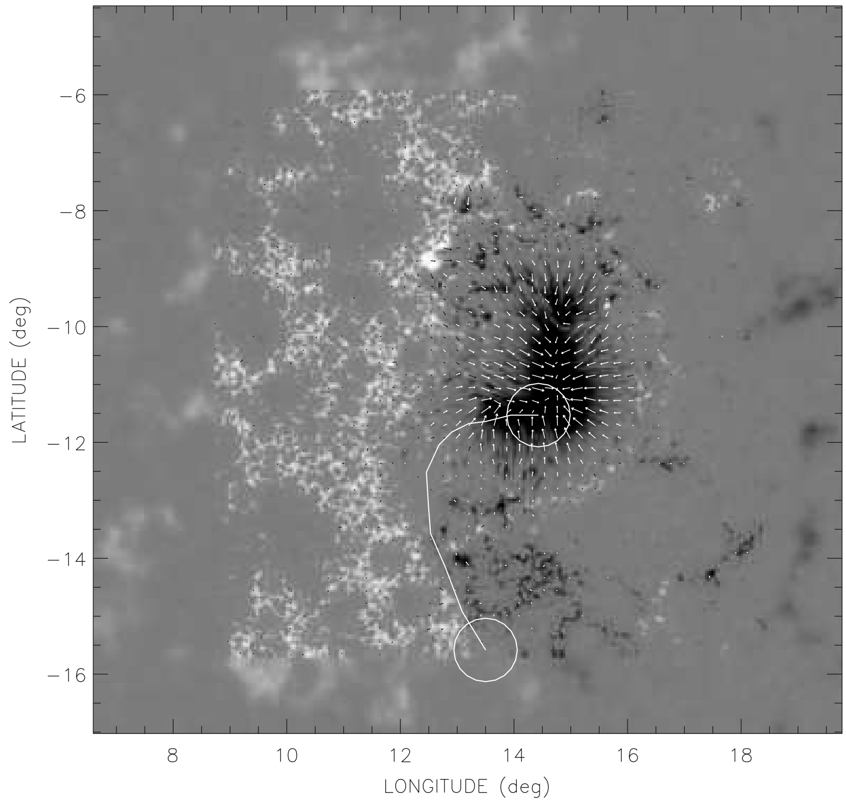

Figure 4. Magnetic map of AR 10953 on 2007 May 2 at 17:30 UT derived from *Hinode*/SOT/SP and *SOHO*/MDI data. The grayscale image shows the radial magnetic field B_r in the photosphere as function of longitude and latitude on the Sun (white for $B_r > 0$, black for $B_r < 0$). The strongest field strength in the sunspot umbra is −2958 G. The vectors show the horizontal components of the observed magnetic field. The vectors are plotted in black or white depending on whether the background is light or dark, and very short vectors are omitted from the plot. The white line ending with two circles refers to the selected filament path along which the flux rope is inserted.

resolution of 0.00065 cos λ radians, where λ is the latitude (for details see Bobra et al. 2008). In the areas outside the SOT/SP field of view, we estimated B_r from lower resolution *SOHO*/MDI magnetograms, assuming the field is nearly radial. Figure 4 shows the radial field as function of longitude and latitude. The vectors show the observed vector field in the local reference frame. The white line ending with two circles refers to the selected filament path along which the flux rope is inserted.

3.2. Modeling Results

For AR 10953 at 17:30 UT, we constructed a potential field model and a grid of NLFFF models with different values of axial and poloidal fluxes of the flux rope. Some of the models we constructed converge to a NLFFF equilibrium state, while others do not converge and the flux ropes lift off. Such "lift-off" occurs when the overlying coronal arcade is unable to hold down the flux rope in an equilibrium state, which happens when the axial and/or poloidal fluxes exceed certain limits. This lift-off is a result of the "loss of equilibrium" of the magnetic system, and is not a numerical problem. Therefore, stable NLFFF exists only when axial and poloidal fluxes are below certain limits.

The time of 17:30 UT is about 2.5 hr prior to a B3.8 flare (see Reeves et al. 2008) and 7.5 hr before the C8.5 flare. We determine the best model for AR 10953 based on the following two criteria: (1) this model should best fit the observed highly sheared X-ray loops; and (2) this model should converge to a stable solution.

3.2.1. Comparisons with X-ray Loops

To constrain the model, we select four nonpotential X-ray loops that appeared in the XRT images at various times. The loops are numbered 1 to 4, and are shown in the four columns of Figure 5. These loops are marked by white and black arrows in the top panels and represented by red lines in the bottom panels. Loop 1 shows a clear S-shaped structure, which first appeared in the XRT observations around 11:00 UT on May 2. Loop 2 is a long and highly sheared loop, and showed up in XRT observations at 15:07 UT on May 2. Both Loop 1 and Loop 2 vanished in association with a partial filament eruption after 16:30 UT. Loop 3 appeared around 22:31 UT and was visible in XRT images until the C8.5 flare began (∼ 23:11 UT). Loop 4 appeared after the filament eruption around 17:40 UT and disappeared around 19:20 UT. Moreover, the shape of Loop 4 is continuously evolving since its appearance in XRT. The blue and light blue lines refer to those model field lines that best fit the observed X-ray loops. These modeled field lines are from different models, and the poloidal flux (Pol) and axial flux (Axi) of the flux rope in these models are displayed in each panel. This figure indicates that our best-fit NLFFF models show very good fit to the observed sheared X-ray loops.

In order to find the model that best fits the observations of a particular loop, we use the following procedure. We define the "average deviation" (AD) between an observed loop and a modeled field line by measuring the distance between a point on the observed loop and the closest point on the projected field line in the image plane, and then averaging these distances for various points along the observed loop. This AD is in unit of solar radii. For each model we manually select the field

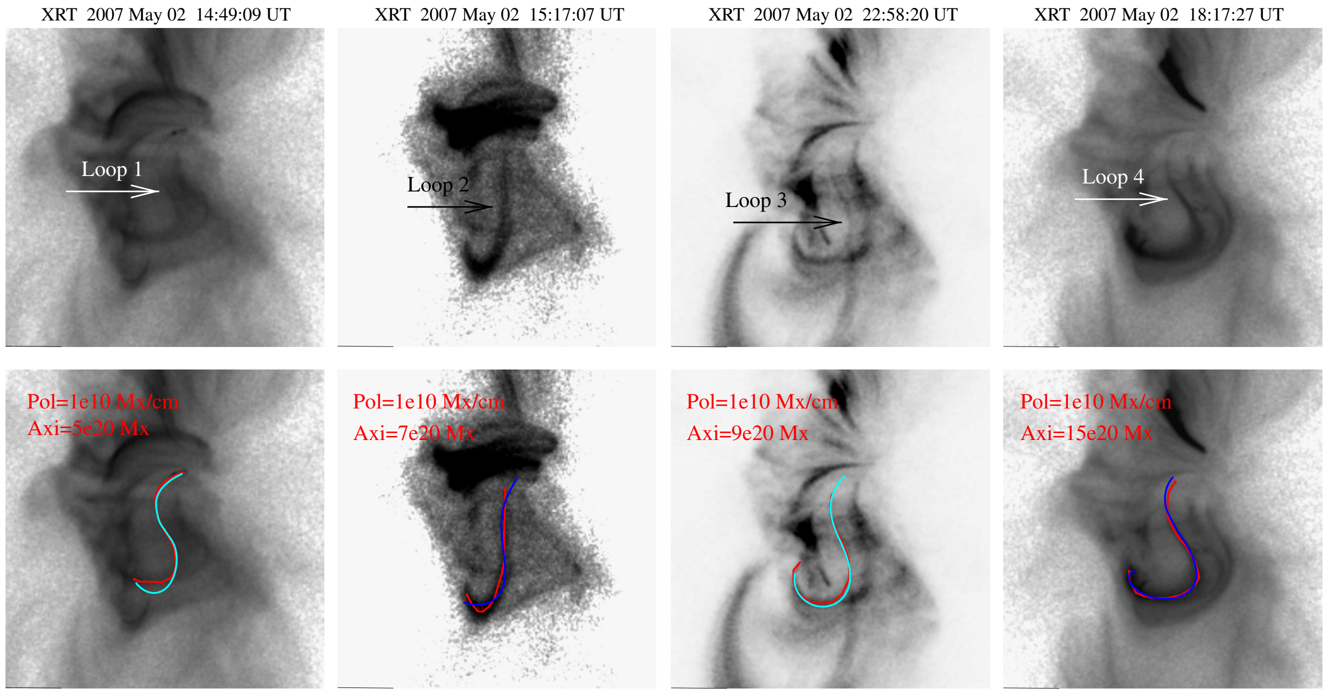

Figure 5. NLFFF models with different axial flux for AR 10953 vs. the observed nonpotential X-ray loops on 2007 May 2. The top panels show the four X-ray loops observed at different times prior to the C8.5 flare. The same loops (red line) overlaid with the best-fit model field lines (blue, light blue) are shown in the bottom panels. The axial and poloidal fluxes of each model are written on the upper part of each panel. The FOV of each panel is 0.2 $R_\odot$.

line that can minimize this AD; this is the 3D field line that best fits the observed coronal loop. Table 1 summarizes the ADs of the best-fit modeled field lines from the observed X-ray loops for various models of AR 10953. The left two columns of Table 1 show the loop number and poloidal flux (F_{pol}) of the model, and models with different axial flux (Φ_{axi}) are listed in the other columns. Table 1 is composed of four main rows, corresponding to different X-ray loops. The three rows of the first main row show the ADs of modeled field lines from Loop 1 for models with different F_{pol}. Similar information for Loops 2, 3, and 4 are shown in the second, third, and last main rows. The ADs for the models that are marginally stable are marked with underline in Table 1. Here "marginally stable" indicates that after 30,000 iterations of relaxation it is still unclear whether the model is stable or not. The ADs for the models which do not converge and the flux ropes lifting off are marked with double underlines in Table 1.

From Table 1 we can see that the models with axial flux of 5×10^{20} Mx, 7×10^{20} Mx, 9×10^{20} Mx, and 12×10^{20} Mx are the best-fit models for Loop 1, Loop 2, Loop 3, and Loop 4, respectively. The ADs of the best-fit models are written in italics. We also found that the best-fit model for Loop 4 is marginally stable, which is consistent with the XRT observations of continuous evolution of Loop 4. Therefore, the result for Loop 4 will not be considered to determine the best-fit model for AR 10953. The comparisons with Loops 1, 2, and 3 indicate that the best-fit model for AR 10953 has an axial flux of $(7 \pm 2) \times 10^{20}$ Mx. Table 1 also shows that the poloidal flux in the best-fit models is 1×10^{10} Mx. However, for most models, the difference between the ADs of the models with different order of magnitudes of poloidal flux are often within the error bars. This indicates that the poloidal flux of the best-fit model has a much wider range, i.e., the XRT observations do not provide strong constraints on the poloidal flux. Table 1 also shows that the upper limit on the axial flux for stable force-free configurations is 15×10^{20} Mx.

Table 1
AD of the Model Field Lines from the Observed X-ray Loops for Various Models of AR 10953 at 17:30 UT on 2007 May 2

Loop	F_{pol} (10^{10} Mx cm^{-1})	Φ_{axi} (10^{20} Mx)				
		5	7	9	12	15
		AD $\pm$ 0.2 (10^{-3} R_{sun})				
	0.1		2.8	3.2	5.3	
Loop 1	1	*1.7*	2.0	2.5	3.1	5.6
	10		2.7	2.8	3.4	
	0.1		2.2	2.4	2.6	
Loop 2	1	3.5	*2.2*	2.4	2.6	3.1
	10		3.7	2.4	2.7	
	0.1		1.9	1.3	1.7	
Loop 3	1	3.9	1.8	*1.3*	1.8	2.4
	10		3.7	1.8	1.9	
	0.1		4.4	3.2	2.0	
Loop 4	1	6.7	4.7	3.4	2.0	*1.2*
	10		5.8	5.3	3.8	

3.2.2. *Comparisons with Observed Vector Fields*

Figure 6 shows a comparison of modeled horizontal field (black arrows) and the horizontal field derived from the SOT/SP observations (blue arrows). This figure shows only a small region of the Southeastern quadrant of the sunspot penumbra (see Figure 4). This is where the largest deviations from the potential field model occur. Figure 6(a) shows the potential field, while Figures 6(b)–6(d) show NLFFF models with fixed poloidal flux but different axial flux, which are marked on the top of each panel. From Figure 6 we can see that all of the three NLFFF models show much better fit to the observations than the potential field model. The error of the azimuth angle (i.e., the average angle between the modeled and observed vectors) weighted by the square of the observed

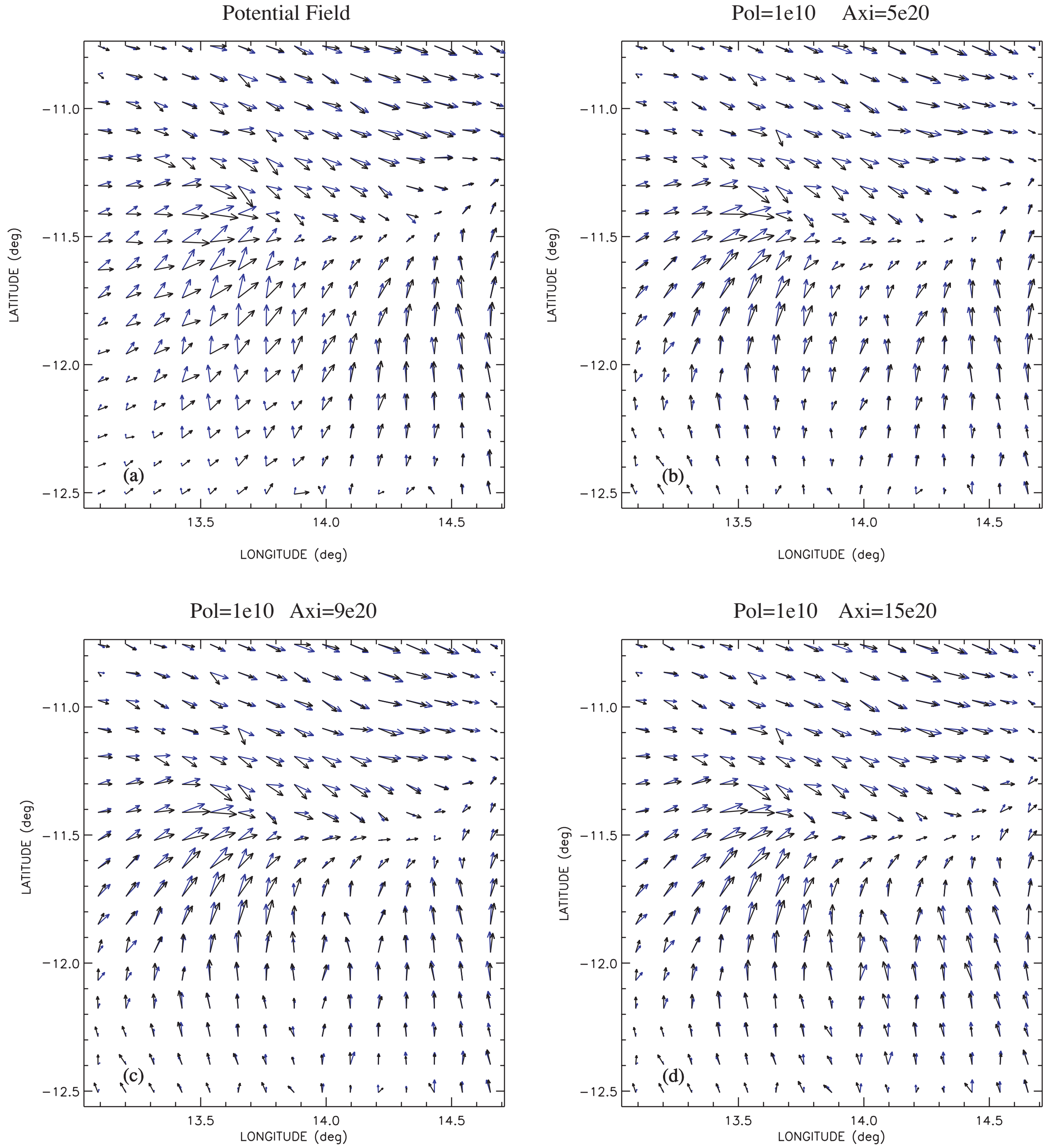

Figure 6. Comparison of observed (blue, SOT/SP) and modeled (black) vector magnetograms. The FOV of each panel is marked by a white box in Figure 4. The model in panel (*a*) is a potential field model, while the models in panels (*b*)–(*d*) are three NLFFF models with fixed poloidal flux but different axial flux, which are written on the top of each panel.

horizontal field in each panel has been calculated. The azimuth errors in Figures 6(a)–6(d) are 26°.10, 15°.73, 13°.88, and 13°.82, respectively. This result appears to suggest that the NLFFF model with higher axial flux fits the observed vector fields better, but the differences between the azimuth errors for the three NLFFF models are not significant. The azimuth errors are much larger than the measurement errors. Therefore, the present models do not provide an accurate fit to the vector field data.

4. DISCUSSION AND INTERPRETATION

Figure 7 shows the results of one of the best-fit models for Active Region 10953 at 17:30 UT. The blue lines in Figures 7(a)–7(b) are selected model field lines within the flux rope that best fit the observed X-ray Loops 1, 2, and 3. Figure 7(c) shows the distribution of the radial electric current density j_r at a height of 6.3 Mm above the photosphere; the currents flow upward on the eastern side of the flux rope ($j_r > 0$) and downward on the western side ($j_r < 0$). Figure 7(d) shows a vertical cross section of the flux rope along the yellow line shown in Figure 7(c); the center of the flux rope is located at $s = 30$, $z = 15$ (cell units). The grayscale image in Figure 7(d) shows the component of the current density parallel to the flux rope. The circular white region shows that the currents are concentrated at the edge of the flux rope, i.e., they have a *hollow core* distribution. In the gray central part of the flux rope the field lines are parallel to the PIL, and therefore highly

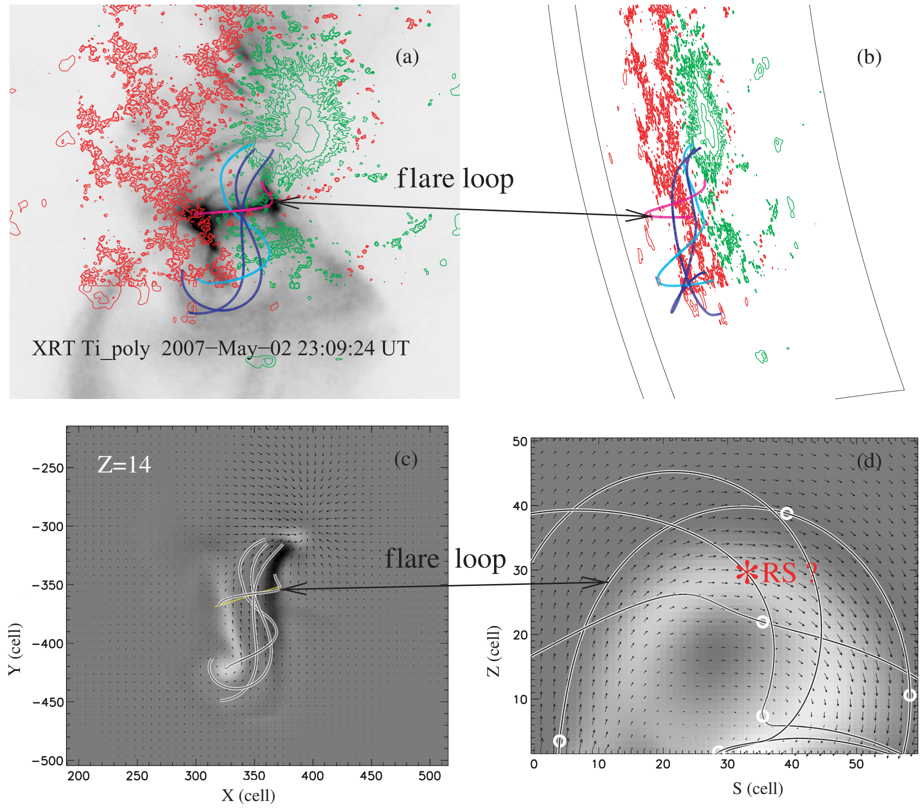

Figure 7. Results for one of the best-fit NLFFF model (Pol=1e10 Mx/cm, Axi=9e20 Mx) for Active Region 10953 at 17:30 UT on 2007 May 2. (*a*) XRT image at the flare onset overlaid with red and green contours representing positive and negative polarities. (*b*) A side view of (*a*). The FOV of (*a*) and (*b*) is 0.2 $R_\odot$. (*c*) Distribution of radial component of current density, $j_r(x, y, 14)$. (*d*) Hollow core distribution of electric currents in a vertical cross section of the flux rope. The location of the vertical plane is shown by the yellow line in panel (*c*). The white region refers to the current layer, and a possible RS at the flare onset is marked by a red star. The white circles represent the crossing point of the model field lines and the yellow line in panel (*c*). The color lines in panels (*a*) and (*b*) and the white lines in panels (*c*) and (*d*) refer to the selected model field lines. The field line marked by black arrows refer to one of the best-fit model field lines for a nearly potential flare loop, which appears at the flare onset.

sheared compared to the potential field, but nearly untwisted because there is no current in this region. In the white region the direction of the magnetic field changes from parallel to the PIL on the inside of the flux rope to perpendicular to the PIL on the outside. The coronal arcade overlying the flux rope is close to a potential field.

The pink line in Figures 7(a)–7(b) is the modeled field line that best fits the nearly unsheared X-ray loop observed at the onset of the C8.5 flare. The side view in Figure 7(b) indicates that this pink line overlies the other three field lines. Figure 7(d) shows that this field line is located just beyond the outer edge of the flux rope where the magnetic field is nearly unsheared and the current density is small. Therefore, the observation of an unsheared loop so close to the flux rope confirms that the magnetic shear falls off rapidly with distance from the outer edge of the flux rope, as assumed in the present model. We conclude that the electric currents in AR 10953 are concentrated in a relatively thin shell at the outer edge of the flux rope, not on the flux rope axis. A similar result was found by Bobra et al. (2008) for two other active regions.

Su et al. (2007a) classified flares according to the degree of shear of the flare footpoints. They showed that for most Type I (ejective) flares the initial flare brightenings are highly sheared with respect to the PIL, indicating that the reconnection site (RS) responsible for particle acceleration and heating initially lies somewhere inside the highly sheared magnetic field. Later during the flare the shear angle usually decreases. In contrast, Type II (confined) flares do not have highly sheared footpoint brightenings, and have no obvious shear change during the flare. The C8.5 flare considered here appears to start as a Type II flare because the X-ray loop observed at flare onset is nearly unsheared and apparently located just beyond the outer edge of the flux rope.

The fact that the observed X-ray loop is located *outside* the flux rope suggests that the flux rope is initially not the main source of energy for the flare. Su et al. (2007a) discussed three possible models for the initiation of Type II flares: emerging (or evolving) flux model; (resistive) kink instability; and confined explosion of a sheared bipole. In the last case one would expect that the reconnection first occurs inside or below the flux rope (Moore et al. 2001). Then the newly reconnected loop should be highly sheared and close to the PIL, which is contrary to our observations of the C8.5 flare. We also did not find any evidence to support the (resistive) kink instability model. Therefore, we focus our attention on the emerging or evolving flux model. This model was first proposed by Heyvaerts et al. (1977), who suggested that solar flares occur when loops of flux emerge from below the photosphere and interact with the overlying field. During the preflare heating phase, continuous reconnection occurs in the current sheets that forms between the new and old flux. Waves that radiate from the ends of the current sheet heat the plasma that passes through them and causes an increase in soft X-ray emission. This model has been generalized to give an Interacting Flux Model with either vertically emerging flux or horizontal spot motions (Priest & Forbes 2002). Interacting flux can show up in many ways, such as the motion of pores

(Raadu et al. 1988), of emerging flux (Simon et al. 1984; Rust et al. 1994) and of cancelling magnetic features (Martin et al. 1985; Wang & Shi 1993).

No large-scale flux emergence was evident in AR 10953 in a long-term movie of MDI magnetograms (May 1 to May 3). However, many moving magnetic features can be seen around the sunspot, and cancelling features are present near the PIL. Therefore, we speculate that at the flare onset magnetic reconnection occurred between two or more loops located somewhere near the outer edge of the flux rope (a possible RS is marked as a red star in Figure 7(d)), resulting in the direct heating of the observed X-ray loop. Although only one X-ray loop is visible in XRT at this stage, we suggest that the observed feature may consist of multiple reconnected (and heated) loops, or that one of the newly formed loops is denser than the others. Initially the flare involved only the magnetic field of these reconnecting loops, but after about 10 or 20 minutes the reconnection spread to the outer parts of the flux rope, triggering the release of a much larger amount of energy stored in the flux rope. Therefore, the main phase of the flare involved reconnection inside the flux rope. This scenario is consistent with the fact that during the main phase of the flare the EUV footpoint brightenings are highly sheared, as expected for reconnection occurring in a highly sheared magnetic field. In summary, we suggest that the initial phase of the C8.5 flare may have been caused by interactions of weakly sheared loops near the outer edge of the flux rope, but during the main phase of the flare the reconnection involved the inner parts of the flux rope, which are highly sheared.

As shown in Section 2.2, the X-ray brightenings (in both *RHESSI* and XRT) appeared about 20 minutes earlier than the *TRACE* EUV flare brightenings, which showed up associated with a filament activation. XRT observations show that these early X-ray brightenings appear to be two bright short ribbons connected with a nearly potential loop, i.e., a loop that follows more or less the direction of the potential magnetic field. The *RHESSI* spectral fitting suggests that the pre-EUV X-ray sources are dominated by thermal emission from an isothermal hot plasma with a temperature higher than 10 MK. This result is consistent with the absence of detectable hard X-ray emission ($>$ 25 keV) prior to the onset of the EUV flare.

It is known that there are mainly two kinds of mechanisms for the EUV footpoint brightenings: thermal conduction from the reconnected loops, and direct bombardment of the lower atmosphere by accelerated particles from the RS (Fletcher & Hudson 2001). The second EUV brightening mechanism can be excluded at the early phase of this flare, because of the absence of accelerated particles indicated by the X-ray observations. However, the hot X-ray sources suggest that there are direct heating in the lower corona probably due to reconnection. The question is why no EUV brightenings were observed corresponding to the long-lasting ($\sim$20 minutes) hot X-ray sources? One possibility is that at the pre-EUV X-ray flare phase, the thermal conduction from the corona was suppressed due to some unknown reasons, plus the energy released at this phase is also very low. Therefore, almost no energy was propagated to the chromosphere through thermal conduction to produce EUV brightenings.

5. CONCLUSIONS

Using the flux rope insertion method, we constructed a series of NLFFF models for AR 10953 prior to a B3.8 and a C8.5 flare on 2007 May 2. The models are created mainly based on the radial field derived from magnetograph data provided by *Hinode*/SOT/SP and *SOHO* MDI, and an Hα filament observed by KSO. By comparisons with four X-ray loops observed by *Hinode*/XRT, we find that the axial flux of the flux rope in the model is well constrained by Loops 1, 2, and 3, while Loop 4 may be in a nonstable state.

By comparisons with the observed X-ray loops, we find that the axial flux of the flux rope in the best-fit model is $(7 \pm 2) \times 10^{20}$ Mx, while the poloidal flux has a wider range, i.e., $(0.1\text{–}10) \times 10^{10}$ Mx cm^{-1}. The axial flux in the best-fit model is well below the upper limit ($\sim 15 \times 10^{20}$ Mx) for stable force-free configurations, which is consistent with the fact that no successful full filament eruption occurred in this active region. The magnetic free energy in one ($\Phi_{\rm axi} = 7 \times 10^{20}$ Mx, $F_{\rm pol} = 1 \times 10^{10}$ Mx cm^{-1}) of the best-fit models is 8.5×10^{31} erg, which is about 10% of the potential energy (9.6×10^{32} erg). This amount of free energy is sufficient to power a B3.8 flare and a C8.5 flare.

The interior of the flux rope in the best-fit model is highly sheared and weakly twisted. The electric current is concentrated at the edge of the flux rope, not on the axis (i.e., the highly sheared field region). This *hollow core* distribution is a consequence of the fact that the flux rope in this model is only weakly twisted, which is consistent with the finding by Bobra et al. (2008).

By comparisons of observed and modeled photospheric vector magnetograms, we find that our NLFFF models show much better fit to the observed vector fields than the potential field model. However, the azimuth errors (i.e., the average angle between the modeled and observed vectors) in the NLFFF models are about 15°, which is large compared to the measurement errors. There is no significant difference in the goodness-of-fit to the observed vector fields for the NLFFF models that we constructed. This poor fit is not surprising, since our models are mainly constrained by the observed X-ray loops, and no attempts was made to fit the observed vector field. Our best-fit model matches the observed loops well, but not the observed vector field. The flux rope insertion method is quite unlike the other kind of methods (Schrijver et al. 2008), which construct NLFF fields by extrapolating observed photospheric vector fields into the corona. These methods are mainly constrained by the photospheric vector fields, and Schrijver et al. (2008) found that even the best-fit model provides a rather poor match to the observed coronal loops. Therefore, our future goal of NLFFF reconstructions should be combining these two type of methods, and to produce models that provide a good fit to both the observed photospheric fields and the coronal fields (X-ray loops).

Two interesting observations are found in the C8.5 flare. The first one is that this flare started from nearly unsheared brightenings and loop, unlike most two-ribbon flares which begin with highly sheared footpoint brightenings as shown in Su et al. (2007a). By comparing with our NLFFF model, we find that this early flare loop is located above but very close to the outer edge of the flux rope. This flare is interpreted in the context of the Interacting Flux Model (Priest & Forbes 2002). We suggest that this flare may start near the outer edge of the flux rope, not at the inner side or at the bottom as suggested in the standard two-ribbon flare model (e.g., Moore et al. 2001).

Another interesting observation is that the X-ray brightenings (in both *RHESSI* and XRT) appeared about 20 minutes earlier than the EUV brightenings, which showed up associated with a filament activation. Our analysis suggests that the soft X-ray emission may be caused by direct coronal heating due to reconnection. The energy transported to the chromosphere may be too low to produce EUV brightenings.

We thank the referee for helpful suggestions to improve this paper. *Hinode* is a Japanese mission developed and launched by ISAS/JAXA, with NAOJ as domestic partner and NASA and STFC (UK) as international partners. It is operated by these agencies in co-operation with ESA and the NSC (Norway). The authors thank the team of *Hinode*/XRT, *Hinode*/SOT, *TRACE*, *RHESSI*, *SOHO* MDI, MLSO, KSO, and *GOES* for providing valuable data. Y.S. acknowledges Kathy K. Reeves for helpful discussions. U.S. members of the XRT team are supported by NASA contract NNM07AB07C to the Smithsonian Astrophysical Observatory (SAO). The *TRACE* analysis are supported at SAO by a contract from Lockheed Martin. Y.S. is also supported by the NSFC projects with 10773032 and 10833007. The NLFFF modeling work was supported by NASA/LWS grant NNG05GK32G.

REFERENCES

Berger, M. A. 1984, Geophys. Astrophys. Fluid Dyn., 30, 79
Bleybel, A., Amari, T., van Driel-Gesztelyi, L., & Leka, K. D. 2002, A&A, 395, 685
Bobra, M. G., van Ballegooijen, A. A., & Deluca, E. E. 2008, ApJ, 672, 1209
Canfield, R. C., Hudson, H. S., & McKenzie, D. E. 1999, Geophys. Res. Lett., 26, 627
Fletcher, L., & Hudson, H. 2001, Sol. Phys., 204, 69
Golub, L., et al. 2007, Sol. Phys., 243, 63
Handy, B. N., et al. 1999, Sol. Phys., 187, 229
Heyvaerts, J., Priest, E. R., & Rust, D. M. 1977, ApJ, 216, 123
Ji, H., Wang, H., Liu, C., & Dennis, B. R. 2008, ApJ, 680, 734
Kosugi, T., et al. 2007, Sol. Phys., 243, 3
Lin, R. P., et al. 2002, Sol. Phys., 210, 3
Lites, B. W. 2005, ApJ, 622, 1275
Lites, B. W., Elmore, D. F., Seagraves, P., & Skumanich, A. 1993, ApJ, 418, 928
Lites, B. W., Low, B. C., Martínez Pillet, V., Seagraves, P., Skumanich, A., Frank, Z., Shine, R. A., & Tsuneta, S. 1995, ApJ, 446, 877
Lites, B. W., & Skumanich, A. 1990, ApJ, 348, 747
Martin, S. F., Livi, S. H. B., & Wang, J. 1985, Aust. J. Phys., 38, 929
McClymont, A. N., Jiao, L., & Mikic., Z. 1997, Sol. Phys., 174, 191
Metcalf, T. R., et al. 2008, Sol. Phys., 247, 269
Mikić, Z., & McClymont, A. N. 1994, in ASP Conf. Ser. 68, Solar Active Region Evolution: Comparing Models with Observations (San Francisco, CA: ASP), 225
Moore, R. L., Sterling, A. C., Hudson, H. S., & Lemen, J. R. 2001, ApJ, 552, 833
Okamoto, T. J., et al. 2008, ApJ, 673, L215
Priest, E. R., & Forbes, T. G. 2002, A&A Rev., 10, 313
Raadu, M. A., Schmieder, B., Mein, N., & Gesztelyi, L. 1988, A&A, 197, 289
Reeves, K. K., Seaton, D. B., & Forbes, T. G. 2008, ApJ, 675, 686
Régnier, S., Amari, T., & Kersalé, E. 2002, A&A, 392, 1119
Roumeliotis, G. 1996, ApJ, 473, 1095
Rust, D. M., & Kumar, A. 1996, ApJ, 464, L199
Rust, D. M., Sakurai, T., Gaizauskas, V., Hofmann, A., Martin, S. F., Priest, E. R., & Wang, J.-X. 1994, Sol. Phys., 153, 1
Schrijver, C. J., et al. 2006, Sol. Phys., 235, 161
Schrijver, C. J., et al. 2008, ApJ, 675, 1637
Simon, G., Mein, N., Mein, P., & Gesztelyi, L. 1984, Sol. Phys., 93, 325
Skumanich, A., & Lites, B. W. 1987, ApJ, 322, 473
Song, M. T., Fang, C., Tang, Y. H., Wu, S. T., & Zhang, Y. A. 2006, ApJ, 649, 1084
Su, Y. N., Golub, L., & van Ballegooijen, A. A. 2007a, ApJ, 655, 606
Su, Y. N., Golub, L., van Ballegooijen, A. A., & Gros, M. 2006, Sol. Phys., 236, 325
Su, Y. N., et al. 2007b, PASJ, 59, S785
Tsuneta, S., et al. 2008, Sol. Phys., 249, 167
van Ballegooijen, A. A. 2004, ApJ, 612, 519
van Ballegooijen, A. A., & Cranmer, S. R. 2008, ApJ, 682, 644
van Ballegooijen, A. A., & Mackay, D. H. 2007, ApJ, 659, 1713
Wang, J., & Shi, Z. 1993, Sol. Phys., 143, 119
Wheatland, M. S. 2006, Sol. Phys., 238, 29
Wheatland, M. S., Sturrock, P. A., & Roumeliotis, G. 2000, ApJ, 540, 1150
Wiegelmann, T. 2004, Sol. Phys., 219, 87
Wiegelmann, T. 2008, J. Geophys. Res., 113, A03S02
Wiegelmann, T., Inhester, B., & Sakurai, T. 2006, Sol. Phys., 233, 215
Yan, Y. H., & Sakurai, T. 2000, Sol. Phys., 195, 89